Synthesis of Nanomaterials for their Applications in Nuclear Research and Radioisotope Production

by

Mi Mu Mu Win

B.Sc., Simon Fraser University 2018

Thesis Submitted in Partial Fulfillment of the
Requirements for the Degree of
Master of Science

in the
Department of Chemistry
Faculty of Science

SIMON FRASER UNIVERSITY
Summer 2022

Declaration of Committee

Name:	**Mi Mu Mu Win**
Degree:	**Master of Science (Chemistry)**
Title:	**Synthesis of Nanomaterials for their Applications in Nuclear Research and Radioisotope Production**
Committee:	**Chair:** **Loren Kaake** Professor, Chemistry
	Byron D. Gates Supervisor Professor, Chemistry
	Erika Plettner Committee Member Professor, Chemistry
	Krzysztof Starosta Committee Member Professor, Chemistry
	Corina Andreoiu Examiner Professor, Chemistry

Abstract

Applications of radioactivity include nuclear medicine and nuclear power, with both industries seeing increased usage and demand every year. Yet, the dangerous nature of the radioactive decay makes it such that widely utilizing radioactivity in society requires proper planning and design for our health and safety. This is not limited to the usage of radioactivity, but also to the production and processing of radioactive materials. Research into the relationship between nanoscale events within a material and the resulting macroscopic properties strongly suggests that nanoscale materials and nanostructures can have a profound impact in developing radiation tolerant materials. This thesis demonstrates the benefits of nanomaterials in the production and processing of radioactive substances, and tolerance to irradiation events. The syntheses of both spherical nanoparticles of sulfur and $BaTiO_3$ nanoparticles were each pursued to utilize these nanomaterials for the purposes of these studies on the interactions of these materials with radiation. We demonstrate production and extraction of ^{32}P from the $^{32}S(n,p)^{32}P$ reaction through the use of a neutron generator. We also demonstrate an easier extraction of the ^{32}P from nanosized sulfur in comparison to its extraction from a commercial sulfur powder. The stability of synthesized $BaTiO_3$ nanoparticles, in terms of crystallinity and structure, was investigated under ~14 MeV neutron irradiation at fluences up to 1×10^{10} neutrons cm^{-2}. In addition, an alternative method is demonstrated to aid in visualizing the extent and the distribution of atomic displacements within the lattices of the irradiated nanostructures. This method is simpler and more cost-effective than the equipment typically required to view atomic displacements such as through the use of aberration corrected high resolution electron microscopes.

Keywords: Nanomaterials; P-32; Sulfur; Barium Titanate; Radiation tolerance; Radioisotope production

Dedication

This work is dedicated to Chris. And to my parents. Who couldn't be there at the end of my academic journey, but made sure I had an amazing start.

Acknowledgements

I would like to express my gratitude to the following people who contributed to the work presented in this thesis:

Dr. Byron Gates: For his guidance and mentorship since my undergraduate career and for the critical development of this thesis.

Dr. Erika Plettner & Dr. Krzysztof Starosta: For their invaluable review and guidance of my work. Their critical outlook on my work was greatly appreciated.

Sakshi Sakshi: Fellow graduate student who aided with imaging S samples.

Dr. Xin Zhang: Staff Scientist at 4D LABS who provided training in electron microscopy.

Dr. Lis Melo: Staff Scientist: Staff scientist as 4D LABS who provided invaluable training in electron spectroscopy, especially with crystallography techniques and elemental analysis.

Dr. Michael Wang: Staff Scientist at 4D LABS who provided training in X-ray diffraction studies.

Melissa Radford: Fellow graduate student who aided with sample loading on the TEM, as well as with imaging $BaTiO_3$ and S nanoparticles.

Annabelle Killham: Fellow graduate student who aided with imaging $BaTiO_3$ and S nanoparticles, particularly with electron diffraction techniques. She also was instrumental in facilitating the long-term neutron irradiation studies.

Heinz Asch & Frank Wu: Graduate students in Starosta Group who helped with the irradiation studies. An integral part of my thesis would not be possible without them.

The rest of Gates Group at SFU: For their immense support during my graduate studies.

Table of Contents

List of Tables

List of Figures

Symbols

Latin

e-	Electron
I_x	Intensity of neutron beam after travelling through distance, x, of a material.
N	The number of identical radioactive nuclei present in a population
N_A	Avagadro constant, the number of constituent particles in one mole of a substance
N_0	N0 is the number of radioactive nuclei at t = 0
N_s	The atomic density of a substance
S	The calculated theoretical activity after irradiation
t	Period of time
t_i	The time period over which irradiation takes place
$t_{1/2}$	The time it takes for exactly half the identical atoms in a sample to decay, on average

Greek

α	Alpha particle
β^+	Beta positive particle
β^-	Beta minus particle
Λ	Decay constant
σ_c	Cross section for neutron capture
σ_t	Cross section for neutron capture and scattering
φ	Neutron flux
ψ	The yield of neutrons emitted from the neutron generator
χ	Thickness of a sample

Glossary

Biological half-life	The length of time it takes for a substance to go from it's maximum concentration in a biological system to reach half the concentration.
Dislocation loop	A lattice structure defect. Can be the absence or addition of an extra plane of atoms.
EDS spectroscopy	An elemental analysis technique that determines presence of specific elements from characteristic X-rays generated when a focused electron beam interacts with the sample.
Electron hole	A hole in a lattice where an electron would normally be located.
Frankel defect	A defect in a lattice where an atom is occupying a normally vacant site other than its own.
HAADF imaging	A mode of STEM where images are formed through detection of electrons scattered at high angles.
Linear energy transfer	The amount of energy an ionizing particle transfers to the surrounding medium per unit of distance travelled.
Neutron capture cross-section	The measure of the probability of an incident neutron to be absorbed by an atomic nucleus.
SEM	Scanning Electron Microscopy. Microscopy that uses a beam of electrons to scan the surface of a sample to form an image.
STEM	Scanning Transmission Electron Microscopy. A transmission microscopy form where the electron beam is scanned over the sample.
TEM	Transmission Electron Microscopy. Microscopy that uses a beam of electrons transmitted through a sample to form an image.

Stacking Fault Tetrahedra	Pyramidal 3-dimensional defect found in FCC (face centred cubic) metals observed during damage such as those induced by radiation.
Redox reaction	A reduction-oxidation reaction. A type of chemical reaction in which the oxidation states of chemical species are changed.

Chapter 1.

Introduction

Materials science concerns the structure and composition of matter, for the purpose of understanding the properties, analyzing the performance, and interpreting any failures of a material in its application(s). In this thesis, materials science is used to demonstrate the benefits of nanotechnology in industries that utilize radioactive materials. This discipline incorporates elements of physics, engineering and chemistry; it is a distinct field that seeks to understand the significance in how a material's processing influences its structure and its resulting properties. This work details the efforts in developing materials for the purpose of improving radionuclide production, as well as for understanding the durability and performance of materials in environments with a high level of radiation exposure.

Nanomaterials are materials that typically range in size between 1-100 nm in width and/or length. Nanomaterials research takes on a materials science-based approach, with a focus on developing new materials with novel properties. While nanomaterials form the physical basis of nanotechnology, research into nanomaterials has often supported the development of microfabrication techniques and technologies, a field historically rooted in the fabrication of devices from semiconductors, such as the preparation of integrated circuits. It is important to promote the expansion of nanomaterials into other applications, as well as maintaining an interdisciplinary outlook in research.

The merger of nanoparticle synthesis and nuclear research in this work required an interdisciplinary understanding of nuclear interactions with materials on the nanoscale. Nanomaterials have a wide range of shapes and morphologies, with significantly different properties from bulk materials. The interactions of different types of nanomaterials with radiation can differ significantly depending not only on the properties of the incident radiation but also on the properties of the material being irradiated (e.g., particle size, internal structure, and composition). The interactions between nanomaterials and radiation can differ significantly from the interactions of radiation with macroscale materials and structures.

Nanomaterials can provide a different perspective to the production, processing, and utilization of radioactive materials. The probing of new materials for novel properties can result in formulated materials that have afforded beneficial properties in various aspects of radionuclide production and their applications. Increasing the number of grain boundaries within a polycrystalline nanoparticle provides more zones for radiation-induced defect annihilation.[1] The addition of layered nanocomposites, with sufficiently thin layers, can prevent the nucleation of helium bubbles formed during irradiation and can inhibit the characteristics of radiation burdened materials that deeply impact their durability.[2] The enhanced radiation tolerance observed in nanostructured materials, as well as the fast-growing field of using nanotechnology in nuclear dependant industries, make the work behind this thesis a valuable contribution to the field.

1.1. Introduction to Radioactive Materials

What distinguishes the elements from each other are their different chemical and physical properties. These properties are ultimately dictated by the atomic nucleus, particularly its composition of nucleons. Likewise, the differences in radioactivity between various radionuclides is due to the level of instability in the atomic nucleus. The excess nuclear energy that is shed during radioactive decay is what differentiates a radioisotope from a non-radioactive atom.

Radiation is the transmission of energy, either in the form of particles or waves.[3] The concept of radiation is not limited to radioactivity: forms of radiation include acoustic radiation, such as sound and seismic waves, as well as gravitational radiation that are formed by the ripples in the curvature of spacetime. Electromagnetic radiation is the propagation of synchronized oscillations of electric and magnetic fields through space, and includes radio waves, microwaves, and visible light. Some radioactive species are radioactive in that they decay by the emission of γ-rays, another form of electromagnetic radiation.[3]

Most radioactive materials shed their excess nuclear energy by emitting subatomic particles which can be a common source of ionizing radiation. Ionizing radiation are subatomic particles or electromagnetic waves that have energies, typically above 10 eV, that are capable of removing electrons from atoms and ionizing them. As such, the damage and degradation of materials exposed to ionizing radiation is common. Despite

that, radioactive materials have been extremely useful, and widely implemented in many industries.

1.1.1. Radionuclides

A nuclide is a species of atom with a specific number of protons and neutrons. The number of protons, a positively charged subatomic particle, dictate the overall property of an atom; each atom has their own atomic number. As neutrally charged subatomic particles, neutrons do not affect the charge of the atomic nucleus. Neutrons do, however, affect the atomic mass and have a mass slightly greater than that of a proton. There is an attractive nuclear force between the protons and neutrons, which is stronger than the repulsive electromagnetic forces between the individual proton charges.[3]

Radionuclides undergo radioactive decay; a process in which an unstable atomic nuclei loses energy through the release of radiation. Radionuclides are atoms with excess nuclear energy. Shedding of energy in the form of an emission gives radionuclides their radioactive properties. A nucleus behaves like a tightly packed ball of high energy nucleons (neutron and protons within the nucleus) that, despite moving rapidly, remain in tightly packed within the nucleus is the culmination of residual strong nuclear forces between quark-quark interactions. Quarks are elementary particles that form composite subatomic particles, such as protons and neutrons. It is the balance between the repulsion between the rapidly moving protons and neutrons, and the strong nuclear force, that maintains the cohesiveness of atoms and stabilizes the atomic nucleus. If there is a lower energy nuclear configuration that exists, the nuclei will transition to the lower mass/energy combination of protons and neutrons and emit radiation during this transition.

Regardless of how long an atom has existed, the stochastic nature of radioactive decay dictates that it is impossible to predict when a certain atom will undergo decay. Yet for a group of a significant number of identical atoms, a decay rate can be obtained. The rate of decay is dependant on the decay constant. The decay constant determines the half-life; the time it takes for exactly half of identical atoms in a sample to decay, on average.

1.1.2. Applications of Radioactive Species

Radionuclides have seen extensive use in medicine and research.[4,5] Over 40 million medical procedures involving nuclear medicine are performed worldwide every year, with the demand for such procedures increasing up to 5% each year.[4] In diagnostics, the nuclides are used to obtain information of the internal anatomy and the functioning of organs. In treatment, they are used to inhibit growth of hemopoietic forms of tumours and have been evaluated to treat peritoneal cancers.

As an example, radiotracers are chemical compounds that contain at least one radionuclide, wherein radioactive decay allows tracking of the compound through chemical reactions. ^{99m}Tc is the most commonly used radiotracer. Technetium based scans utilize detectors to identify the γ radiation emitted from the radiotracer. The measurement of γ-rays from radiotracers is employed in SPECT (single photon emission computed tomography) scans while PET (positron emission tomography) detects positrons emitted from radiotracers undergoing β^+ decay (to be discussed in Section 1.1.3.). For therapeutic purposes, applications can include their use either internally or externally to a patient. An emerging example is targeted alpha therapy (TAT), currently studied for possible use in immunotherapy, and to treat a variety of types of cancers.[5]

The TAT is a method currently in development largely for targeted radionuclide therapy of cancers that include peritoneal carcinomas, leukemia, as well as Phase I trials in melanomas. This form of therapy utilizes α decay either to treat diseased tissue near the radioactive species, or to enable imaging of specific areas in the tissue within the body. Although the penetration range of α particles in tissues is only 40 to 90 μm, α-emission can often be detected by either the accompanying gamma emission. The basis for TAT lies in the relatively high linear energy transfer of α particles in comparison to other forms of radioactive decay, such as β decay. The higher mass of α decay particles results in the stoppage of the particles over shorter distances through the tissue, and more energy deposited per distance travelled.

1.1.3. Interactions of Materials with Radioactive Species

.There are multiple decay modes, with radioactive species undergoing one or all of them. The three most common types of decay are α decay, β decay, and γ decay. The

forces that govern these decay modes are the nuclear force, the weak force, and the electromagnetic force, respectively. α decay involves the emission of an α particle, a helium nucleus. β decay can be categorized into two main forms: (i) β^+ decay; and (ii) β^- decay. In β^+ decay, a positron and a neutrino are emitted. A positron is the positively charged antiparticle counterpart of the electron. In β^- decay (see Figure 1.1.) an electron and neutrino are emitted from the nucleus. During β^- decay, a neutron is converted to a proton by transformation of one of its down quark into an up quark. This conversion is accompanied by emission of an carrier boson, which then decays into the emitted electron and the electron antineutrino. This decay of radioactive particles is mediated by the weak force which acts only over a much shorter distance when compared to the electromagnetic force and strong nuclear force. γ decay is the emission of high-energy photons due to an atomic nucleus being in an excited state. As a highly energetic form of radiation, γ decay consists of electromagnetic waves with very short wavelengths.

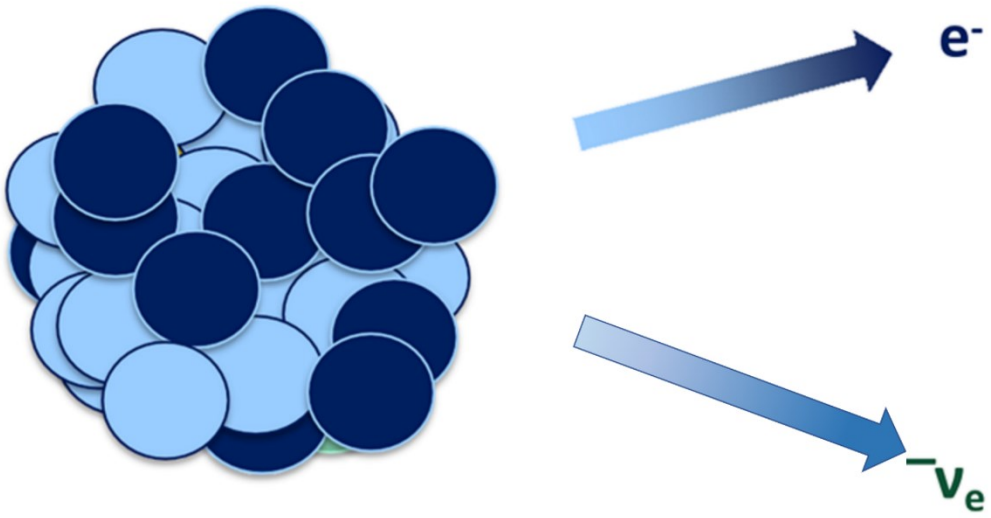

Figure 1.1. Depiction of a β^- decay of a nucleus, in which there is emission of a β^- particle (an electron), and an electron antineutrino

Radioactive decay often results in nuclear transmutation, where the element or isotope of an element undergoing decay is converted into another element. This decay process results in a change in the number of protons in the nucleus. There are, however, nuclear decays that do not result in nuclear transmutation. For example, instead of an emitted particle, an unstable nucleus may lose its energy through the emission of γ-rays. In the process of internal conversion, an electron is coupled to an excited state of the

nucleus. If the energy conferred to the electron is higher than its binding energy,[1] the electron is ejected from the atom. With the origin of the electron not from the nucleus, the emitted electron is not considered to be a β particle and internal conversion is considered a non-radioactive process.

Neutron interactions with materials can, on the atomic level, be grouped into scattering or absorption events. The interactions of free neutrons with matter can elucidate information about a material, and thus neutron diffraction techniques are being used for analyzing structures. Elastic scattering is used in neutron diffraction, where a beam of thermal neutrons hit a sample and the resulting diffraction pattern is used to determine the static structure of gases, liquids, or solids. Inelastic neutron scattering is used in vibrational spectroscopy by determining the change in energy of a neutron as it passes through the material.[6] The difference between elastic vs inelastic scattering of neutrons lies in the whether or not the kinetic energy of the incident neutron-nucleus system is unchanged after the interaction of an incident neutron and the target nucleus.

Neutron capture is the process in which an atomic nucleus absorbs a neutron. Neutron capture is one of the multiple possibilities of events that can occur when a material is irradiated with neutrons, and an atom interacts with a bombarding neutron. The probability of each interaction depends on factors that include, but are not limited to, the composition and size of the target nucleus and the energy of the bombarding neutron. There are various types of neutron capture events, largely categorized with what happens to the nucleus after the absorption of the neutron.

In fission based neutron capture events, the capture of a neutron causes the atom to split into fragments and create more neutrons. In electromagnetic neutron capture, a neutron is absorbed by a nucleus that then emits a γ-ray as a result. In neutral types of neutron capture, the emitted particles are neutrons (neutrally charged). For charged neutron capture, the absorption of a neutron produces a charged particle, such as the (n,p) reaction in which a proton is emitted. The work in this thesis will investigate the $^{32}S(n,p)^{32}P$ reaction as one of the two foci herein on the interactions of neutrons with nanoparticles.

[1] Energy required to remove a component from a system of parts

1.1.4. Conventional Methods for Radionuclide Synthesis

Radionuclide syntheses can happen through multiple modes. Naturally occurring radionuclides are categorized as primordial, secondary, and cosmogenic. Primordial radionuclides are produced through nuclear reactions in stars and in supernova explosions. Secondary radionuclides are derived from the decay of primordial radionuclides, arising in the decay chain of the radioisotopes ^{232}Th, ^{238}U and ^{235}U.[7] Cosmogenic radioisotopes are continuously formed in the atmosphere due to incident cosmic rays, generally through the interactions of cosmic rays with atoms within the solar system. They are formed from the high energy interactions between a cosmic ray and an atom, causing protons and neutrons to be expelled from the atom.[8]

Radionuclides can be created intentionally through a designed synthetic route that include radionuclides generators, particles accelerators, or nuclear reactors. In nuclear reactors, alongside the important nuclides extracted from nuclear waste, radioisotopes are deliberately produced by inserting certain elements with a relatively high neutron capture cross-section within the reactors. A neutron capture cross-section is related to the probability of a neutron capture event when there is an interaction between an incident neutron and an atomic nucleus. These elements are readily activated through neutron capture from the high flux of neutrons present within the reactors. In particle accelerators, charged particles are used to bombard targets that also produce radionuclides. An example are cyclotrons, in which an electric field is applied to accelerate charged particles. A static magnetic field is implemented to bend their trajectories into a spiral, allowing the particles to encounter the accelerating region created by the electric field multiple times, creating high energy charged particles.

The last major synthetic method for creating radionuclides utilize radionuclide generators. This method refers to parent radionuclides that produce daughter radionuclides through decay processes, with the parent often produced in nuclear reactors. A very common example is ^{99m}Tc, in which its parent nuclide ^{99}Mo is produced in a nuclear reactor.[8] ^{99}Mo has a half-life of 2.75 d before decaying to ^{99m}Tc. This relatively long decay time has enabled the shipment of ^{99}Mo to medical facilities where ^{99m}Tc could be extracted. Currently, ^{99}Mo for medical use is largely obtained from fission products formed when ^{235}U targets are irradiated with neutrons. These radionuclide generators are not applicable for radioisotopes that do not have a parent nucleus with an appropriate half

life; too long and there is not enough production of the radionuclide of interest, too short and the radionuclide will not last the transportation times. One notable example is ^{32}P.[8]

A large portion of medically pertinent radionuclides are produced in nuclear reactors through the neutron bombardment of bulk materials. Nuclear reactors operate on the basis of a fission chain reaction from interactions between fissile isotopes, such as ^{235}U, and neutrons. In a nuclear reactor, the atom undergoing fission releases neutrons. Any surrounding fissile atoms can absorb the emitted neutrons and cause more fissions and release of more neutrons. To prevent an uncontrollable reaction, and a possible nuclear meltdown, control rods containing neutron absorbers are placed within the reactor to strategically capture excess neutrons and control the nuclear chain reaction. These control rods serve to control the rate of fission of nuclear fuels. The composition of these rods includes elements that have a high neutron capture cross-section, such as cadmium, boron, and silver. Strategically, these rods can contain specific elements that, when capturing a neutron, are intentionally transformed into specific radionuclides.

Removal of target material and impurities for radionuclide extraction can be complex and time consuming. Any impurities present in the control rods (or other irradiated materials) may lead to not only a lower production of the intended radionuclides, but also neutron activation of impurities and unwanted production of other species. The extra precautions and knowledge in handling radioactive substances, and the cost of extracting these radionuclides can be very high. Starting with materials that can reduce the need for extensive processing can save time, and ultimately costs. For example, if the radioactive materials had a significantly higher surface area to volume ratio, removal of radioactive species produced within the material could be quicker and easier than with a bulk material.

Another aspect to consider for the production of radionuclides is the source of their production. Nuclear reactors cost billions of dollars and take many years to make.[9] This does not include the cost of maintaining and running such a large-scale operation. This is also true for cyclotrons and large linear accelerators. The high cost of building and maintaining nuclear reactors and large linear accelerators means there are less than 500 nuclear reactors in the world.[10] The result is that radionuclides produced in such facilities must be transported from afar to be used at their final destination. Since radioactive materials constantly undergo decay, there is a time limit for these materials before they are not sufficiently active for their intended purposes. These limitations are even more

significant for radionuclides used in medicine; they often have a relatively short half-life to ensure rapid decay after treatment, to protect the health of the patients.

Being able to produce some radioactive species in devices much smaller, and more portable, than nuclear reactors ultimately mean demonstrating the ability for the in-house production of these species. For example, a medical clinic could produce their own ^{32}P on demand for diagnostic imaging. It can, therefore, be hypothesized that one can produce applicable nuclides through neutron activation through more convenient means via the use of a neutron generator and a nanomaterial product that is more easily processed for extracting or otherwise using the radionuclide species. As such, there is motivation in this thesis for evaluating ^{32}P production through the use of nanoscale sulfur particles by neutron bombardment via a portable neutron generator.

1.2. Introduction of Nanomaterials in the Nuclear Industry

Nanomaterials designed for radiation tolerance have been studied for a variety of applications. These studies are fueled in part by an increasing consumption of energy worldwide. Aside from the ethical dilemmas associated with pollution from the removal and usage of fossil fuels and natural gas, the limited supply greatly supports the need for alternative energy sources, including nuclear power and renewable energy sources. In the United States, 20% of energy is sourced from nuclear power, while nuclear power serves 13 to 15% of the world's energy needs.[11]

There is the potential for improvement in many aspects of the nuclear industry. Improved nuclear fuels can increase fuel efficiency by avoiding losses. The fuels can also increase fission gas retention, radiation tolerance, and heat transfer capabilities. Increasing the efficiency of capturing toxic fissile products can improve the safety for employees at reactors and lessen the hazardous nature of nuclear waste. In addition to the required integrity of materials and structures prepared from materials in nuclear reactors for safety reasons, the durability of materials is also important in the handling and management of nuclear waste.[12]

The benefits of nanotechnology are not limited to the nuclear industry; nanostructured materials and nanomaterials prepared from alloys have been engineered to enhance the structural integrity of materials under extreme conditions, including at high

or low temperatures, under high mechanical stresses, and in high irradiation environments. Therefore, nanomaterials designed for radiation tolerance have been studied in applications that also include space exploration and solar cells.

1.2.1. Improving Nuclear Industry with Engineered Nanomaterials

Radiation heavy industries rely on facilities that can withstand radiation-induced damage. Part of the purpose of the thesis is to provide motivation for developing nanomaterials for radiation tolerance. The field of nuclear fuel development has seen the possibilities of an immense enrichment through applying nanotechnology. So far, the crux of nanoengineered fuels has been to increase enrichment of ^{235}U levels; natural abundance of uranium is only 0.7% as ^{235}U, which is the fissile isotope that undergoes fission reaction when absorbing thermal neutrons. The most common type of reactors, light water reactors, require up to 5% ^{235}U content in the fuel just to sustain the fission reactions.[13] Synthesized, high ^{235}U content UO_2 nanocrystals have numerous pores to efficiently adsorb highly reactive fission products such as iodine. The nanostructured morphology can improve fuel burnup by enhancing thermal and radiation stability. Other fission capturing nanotechnology products include porous metal organic frameworks as structures for capturing and temporarily storing toxic fission gasses.[14] In these compounds hazardous I_2 interacts with the tetrahedrally coordinated Zn atoms.

Another field of nanoengineered materials gaining momentum for radiation tolerance are ODS alloys. The ODS (oxide dispersion strengthened) alloys are potential candidates for increasing durability in reactor materials. These alloys consist of a metal matrix, such as iron-alumina or iron-chromium, wherein oxide particles below 100 nm in diameters are dispersed within this matrix. These alloys display enhanced corrosion resistance and mechanical properties at high temperatures, particularly over 600 ºC. These properties include enhanced radiation resistance, corrosion resistance, and tensile strength. As such, ODS alloys have become promising candidates for use in future nuclear reactors for high-temperature applications.[15]

The interactions between incident radiation and materials can be destructive-particularly if the radiation is ionizing. Significant material and biological damage are serious issues in the nuclear industry, as well as other applications in which radiation is prominently present. “Nanotechnology-enabled sensors” and *in situ* monitors can monitor

the properties of a material as it faces extreme conditions, while being able to differentiate between different forms of radiation. Radiation sensors can serve as a warning that too much irradiation is present for safety precautions but can also serve as tools to determine correlations between irradiation dose and properties of the irradiated materials.[12,16,17]

1.2.2. Degradation of Materials

The degradation of a material under radiation depends on the ability of the material to self-heal, the degree of particle interactions with the material and the properties of the bombarding radiation particle(s). The extent of damage can be mitigated by the presence of a nanostructured morphology, as explained in later chapters. Understanding the effects of radiation on a material are important for preventing failure and maximizing performance of the material in the intended applications. There are numerous industries that deal with exposure to a significant radiation flux, such as in the nuclear industry, in devices used in outer space or in the outer regions of the atmosphere, and in solar panels.[18] Materials that are sufficiently damaged can fail prematurely under the harsh conditions of some of these industries. For example, common structural failures in reactors include fractures and cracks.[19]

Damage, particularly during irradiation, is not static. The evolution and growth of damage have been observed and can be predicted through complex computer simulations.[20–22] Point defects that culminate in cavities can nucleate and evolve into voids (agglomeration of vacancies) and bubbles (agglomeration of point defects). One of the most devastating macroscopic effects of these defects include swelling, which can increase the embrittlement of a material and decrease the leeway in mechanical stress tolerated by a material before cracking occurs. The consequences of not understanding the impact of radiation on materials and devices in use in the field can be devastating. Materials failing unexpectedly can lead to a loss of operational time, income, and ultimately loss of life. Implementing engineered nanostructure into materials used in, for example, nuclear reactors, can prevent structural failure. Part of the work in this thesis evaluates the extent of damage in an irradiated material.

1.3. Sulfur Nanoparticles

Sulfur nanoparticles are widely used as the basis for antimicrobial and anticancer agents, in lithium-sulfur batteries, and in sulfur-based photocatalysts. For example, flexible lithium-sulfur batteries are promising candidates for a new generation of energy storage devices. These batteries have opened up the concept of incorporating sulfur into batteries, where current commercial lithium-ion batteries have a limited charge capacity and energy density. Sulfur cathodes have a high theoretical specific capacity of ~1670 mAh g^{-1} and Li/S batteries have an energy density up to 2600 W h kg^{-1}, which is much higher than with many other types of lithium-ion batteries.[23,24] These other types of lithium-ion batteries include lithium manganese cobalt oxide batteries and lithium cobalt batteries, which can achieve energy densities up to ~280 W h kg^{-1}.[25] Sulfur nanomaterials are being realized for their potential in batteries, providing motivation to further explore nanoscale sulfur morphologies.

Sulfur is a naturally abundant element and is extremely important in the production of sulphate and phosphate fertilizers, as well as for its use in other industries. Sulfur is also essential to life, normally found in the form of organosulfur (S_x) or metal sulfides. The relatively strong S-S bond (265 kJ/mol) results in the numerous sulfur allotropes, second only to carbon.[26] The ability of sulfur to catenate is largely due in part the to the difference in energy stability between two σ bonds versus a S-S π bond. The high energy S-S bond is weaker only to H_2 and C=C in terms of homonuclear single bonds. While double bonds are stronger than single bonds, S=S bonds are not significantly stronger than a S-S bond. This similarity in bond strengths between the double and single bonds is because of the poor π bonding overlap of 3p orbitals inhibiting bond strength more than the hinderance of lone pair repulsion that would weaken the σ bond in S-S. Therefore, sulfur tends to exist as a chain, such as the formation of S_8 over S_2. The longer, extended chain is the preferred thermodynamic state. Elemental sulfur contains mostly S_8 species, with smaller amounts of S_7 and S_6 present.

The most common allotrope of sulfur is cyclo-S_8, forming a crown conformation (Figure 1.2.) Octasulfur has three distinct polymorphs, of which only two are stable. At room temperature S_8 is in the form of α-octasulfur, which has an orthorhombic crystal structure. Above 95.2 ºC, α-octasulfur transforms into β-octasulfur, which has a monoclinic crystal form. This transition proceeds through a change in intermolecular interactions; the

S_8 crown conformation itself is unaffected. The difference in the polymorphs is how the rings are packed in the crystal.

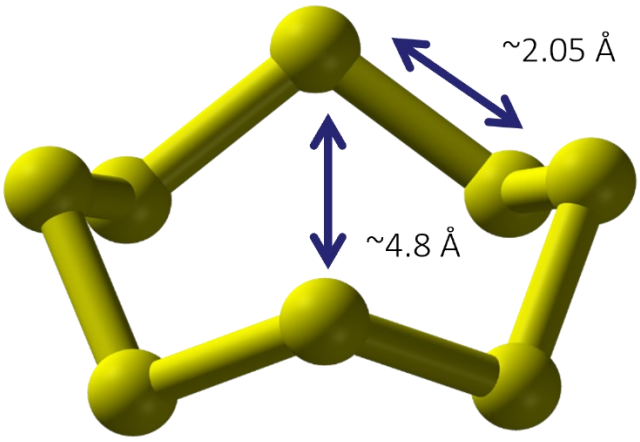

Figure 1.2. Schematic of sulfur showing the approximate interatomic dimensions in crown S_8.

There are many synthetic methods that have been published on the preparation of sulfur nanoparticles. Heating of sulfur can be not only hazardous, but also can be a challenging approach to preparing nanoscale sulfur materials—especially when size control is critical in the synthesis. Microemulsion methods for sulfur nanoparticle synthesis have been developed yet can be complicated methods, composed of surfactants, co-surfactants, and oil and aqueous phases.[27,28] A microemulsion system contains a lipophilic phase and a hydrophilic phase. A dispersion of these phases forms droplets of one phase suspended in the other phase, creating the microemulsion. The coalescence of droplets containing reactants allows the formation of microreactors that can be used for nanoparticle formation. Microemulsion methods can be difficult to scale up due to tedious processes required for the subsequent separation of the resulting particles from the multiple components of the microemulsion systems that may have similar chemical properties. Furthermore, published methods using a reverse microemulsion, created using a mixed gas-liquid system of H_2S (g) and a solution of iron chelate as a catalyst resulted in the formation of sulfur nanoparticles through an even more complex mechanism than that achieved with microemulsion methods.[29] Methods such as this also results in a potentially complex situation in which to extract and purify the sulfur nanoparticles.

Based on the current literature, it appears the currently favored approach to preparing sulfur nanoparticles with size control is through an acid catalyzed decomposition of sodium thiosulfate.[30] Any leftover salts and side products are washed away from the product using H_2O and an organic solvent. As with any precipitation reaction, the surfactants play an important role in the resulting particle size. Surfactants act as directing agents, their adsorption onto the surfaces of the particles affects the further adsorption of materials, resulting in surface passivation and shape control effects during the growth of the nanoparticles. The preferential adsorption of surfactants onto certain planes of a crystalline lattice may result in an anisotropic growth of the crystal and the formation of specific morphologies. What makes a surfactant adhere more strongly to a certain plane of a crystal includes the bulkiness of the surfactant's head group. For example, steric hindrance can favour the formation of elongated or cylindrical micelles, which can have a greater affinity to adsorb on a specific crystal plane, ultimately influencing the formation of the particle morphology. One notable example is the use of cetyltrimethylammonium bromide (CTAB) in Au nanorod synthesis.[31] While other factors are involved in shaping a particle, surfactants are one of the biggest influences in directing particle shape and guiding growth by preferentially adsorbing onto different crystal planes of the nuclei that serve as seeds to the formation of nanoparticles.[32] The methods pursued in this thesis will utilize an acid catalyzed decomposition of sodium thiosulfate in the presence of surfactants as one of the methods to prepare nanoscale sulfur particles for irradiation with neutrons.

1.3.1. Radionuclide Production using Sulfur

Its relatively short half-life of ~14 d means that ^{32}P would only exist naturally on earth in small amounts. Anthropogenic sources of ^{32}P include large nuclear reactors that utilize the bombardment of phosphorous through the (n, γ) reaction. Other reactions include the (n, α) reaction where ^{35}Cl is converted into ^{32}P, as the ^{35}Cl atom absorbs a neutron and emits an α particle. Another process is the $^{32}S(n, p)^{32}P$ reaction. The ^{32}S nuclei absorb one neutron and emit a proton. Lastly, the (n, γ) reactions are when a neutron is absorbed, followed by emission of a γ species. The majority of ^{32}P is produced in nuclear reactors. Light water reactors are the most common form of the ubiquitous thermal-neutron reactor. In light water reactors, regular water (as opposed to D_2O) is used

as the coolant and neutron moderator. The ^{32}P activity concentrations form these reactors are in the range of several kBq/L.[33]

^{32}P radionuclides have been produced by cyclotrons in the past, in a (d,2p)[2] reaction of ^{32}S using incident particle energies of 18 MeV. The energies required for this reaction are outside of the capability of current table-top cyclotrons. Furthermore, the footprint and mass of in-house cyclotrons are much larger than that of a portable neutron generator. Cyclotrons also produce protons, and not the neutrons needed for the other possible nuclear reactions resulting in the synthesis of ^{32}P. Considering the issues of cost and the practicality of implementation, portable neutron generators are currently the optimal solution for producing ^{32}P when nuclear reactors or cyclotrons are not ideal for the intended application and/or location of the intended use, such as when needing the on-site production of ^{32}P for medical or clinical applications.

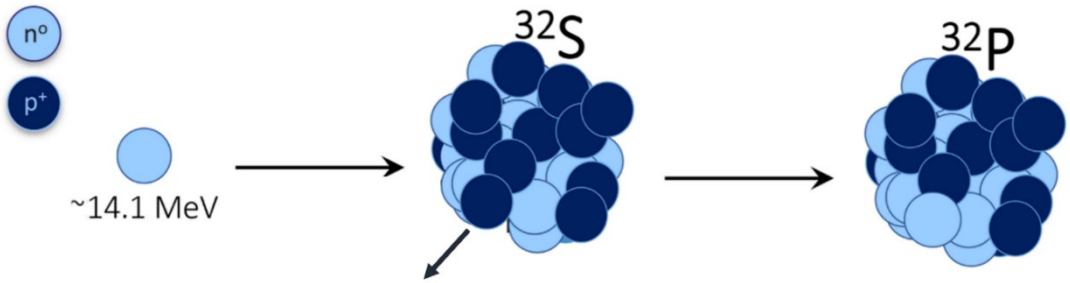

Figure 1.3. Schematic of ^{32}P formation from the neutron bombardment of ^{32}S with a neutron at an energy of 14.1 MeV.

The viability of demonstrating an easier and more economical method of ^{32}P production is largely due to the natural abundance of ^{32}S. Fast neutron irradiation of sulfur can lead to the production of ^{32}P through the $^{32}S(n,p)^{32}P$ reaction (Figure 1.3.). Sulfur exists naturally as 94.9% of the ^{32}S isotope. Possible side reactions that could significantly limit the ^{32}P production involve the next two most abundant sulfur isotopes: ^{33}S and ^{34}S at natural abundances of only 0.76% and 4.79%, respectively. Not only can the presence of other isotopes in sulfur lower the possible yield of ^{32}P formed, but those other isotopes can also introduce side reactions and products that can complicate the ^{32}P extraction process. For ^{33}S, the most significant side reaction is the $^{33}S(n,y)^{34}S$ reaction. Previous studies show that the neutron capture cross-section of ^{33}S is significant only at very low

[2] A nuclear reaction in which a deuteron is absorbed, and 2 protons are emitted.

neutron energies (<1 MeV).[34] The $^{34}S(n,y)^{35}S$ reaction has its highest cross-section values also at energy levels much lower than 14.1 MeV.[35] Therefore, the relatively small cross-sections of the two alternative isotopes and their low natural abundance relative to the ^{32}S isotope suggests that side reactions with these alternative isotopes are of little concern to the yield of $^{32}S(n,p)^{32}P$ via the fast neutron irradiation of a natural source of sulfur (i.e., without enrichment of ^{32}S). Sulfur enriched with ^{32}S is not necessary for our work. The highly penetrative nature of neutrons suggests that the ^{32}P radionuclides would be produced throughout the sulfur nanoparticles.

1.3.2. Applications of ^{32}P Radionuclides

Phosphorous is a monoisotopic element; only one of its 23 isotopes is stable. The isotope ^{32}P has a half-life of 14.26 d.[36] The nucleus contains 17 neutrons and 15 protons. Decay of ^{32}P involves the emission of a β particle with an average energy of 0.7 MeV. The relatively short half-life of ^{32}P means that it exists in only small quantities on Earth. Yet because phosphorous is found in so many organic compounds, ^{32}P is widely used in medical research—particularly in biochemistry and molecular biology. The radioisotope is used as a radiotracer to track phosphorylated molecules, such as in metabolic pathways, and to label DNA. The decay of ^{32}P is described by Equation 1, with decay particles having a maximum energy of 1.71 MeV:

$$^{32}_{15}P \rightarrow {}^{32}_{16}S^{1+} + e^{-} + \bar{\nu}_e \qquad \textit{Equation 1}$$

The release of the electron, e^-, is accompanied by an electron antineutrino. The electron antineutrino is the corresponding antiparticle to the electron neutrino, which is a fundamental particle. The decay energy of 1.71 MeV is enough for the radiation to penetrate the skin (up to 8 mm), allowing for an external detection of the radiation for use in locating and imaging tumours, as well as for the treatment of certain types of leukemia. β particles have already been demonstrated in a clinical setting to kill cancer cells.[37] The small linear energy of transfer of β-emitters compared to α-emitters for cancer treatment means that the radiation source does not need to be positioned directly at the cancerous cells; the β-particles can travel further through biological tissue, up to 8 mm in path length compared to ~40 μm for α particles.[37] This helps overcome α decay's limitations in which it is most useful for small tumours.

There has been a few approved drugs that implement ^{32}P. $Cr^{32}PO_4$ has been studied as a potential treatment for ovarian cancer due in part due to its long-term toxic effects by the accumulation of radioactive phosphorous species that is detrimental to cells, including those cancerous in nature.[38] Likewise, radioactive phosphorous has been used to treat blood disorders where the radiation absorbed by the bone marrow decreases the production of red blood cells and platelets. Yet the range of ^{32}P use in these disorders has been scaled back as the myelotoxicity of ^{32}P has stopped the recommended use of this isotope in palliative bone cancer therapy. Nowadays, ^{32}P is used to treat cystic craniopharyngiomas (benign tumours near the pituitary gland), as well as general polycythemia vera (a disorder resulting in significant increases in red blood cells). [39,40]

As well, though ^{32}P usage has largely been restricted to colloidal suspensions, recent research demonstrates the growth inhibitions of tumours in mice using low dose injections of intravenous solutions. In addition, unlike many clinically studied β emitters, ^{32}P possesses the ability to induce double strand breakage in DNA, offering powerful antitumour properties.[40] Due to its influence on double strand breakage,^{32}P has been shown to be more efficient than equivalent doses of high energy electrons emitted such as those from ^{90}Y, a β emitter more commonly used today.[41]

The valuable study of biological systems is complicated by the immensely convoluted and dynamic nature of their underlying mechanics. Living organisms deal with fluxes of metabolites and must maintain homeostasis for optimal functioning of the organisms in terms of fluid balance, body temperature, and many more variables.[42] The steady state nature of physical and chemical conditions means that there is a constant flux of metabolites that must be regulated, depending on the current needs of the body. Studying the metabolic pathways can be complex and involves monitoring the movements of metabolites and various compounds. Phosphate is abundant in biological systems. As such, phosphate labels are used extensively in the study of the metabolism of organisms, such as for the generation of different biomolecules.

1.4. $BaTiO_3$ (Barium Titanate) Nanomaterials

1.4.1. Introduction

For the purpose of investigating radiation-induced damage in this thesis, the aim is to synthesize sub-100 nm $BaTiO_3$ nanoparticles for determining their tolerance to fast neutron radiation. $BaTiO_3$ is a perovskite type material; these materials are commonly found in technologies and instruments that are subjected to elevated levels of radiation from sources that include cosmic rays and cosmic spallation.[43] The cost effective and facile manufacturing of perovskite type ultrathin films that absorb the complete visible spectrum make them a promising candidate for the next generation of solar cells.[44] Furthermore, perovskite titanates have been demonstrated for potential applications that include immobilizing fission products in nuclear waste.[45] Although radiation studies on $BaTiO_3$ and other ABO_3 materials have been beneficial to the nuclear industry and other radiation heavy environments, these studies are limited. Adding to the irradiation studies of $BaTiO_3$ is invaluable. In this thesis, $BaTiO_3$ materials with small dimensions (<100 nm) were sought for their nanocrystalline characteristics of these materials, and a plate-like morphology was sought to enable a relatively simple determination of structural failures within these particles using transmission electron microscopy techniques.

1.4.2. Properties and Applications of $BaTiO_3$ Nanomaterials

$BaTiO_3$ is a ceramic ferroelectric material with piezoelectric properties.[46] The cubic phase of $BaTiO_3$ is depicted in Figure 1.4. The spontaneous electrical polarization in ferroelectric materials can be reversed by an external magnetic field. The implications of this are that these materials can be used in capacitors to confer a high and adjustable capacitance. As such, $BaTiO_3$ is currently used in electronic devices such as capacitors and thermistors. The piezoelectric properties have resulted in a wide use of $BaTiO_3$ in electromechanical transducers, and more recently this material is being investigated as a lead-free perovskite alternative for piezoceramics.[47] Polarization and permittivity data from as early as 1949 illustrated the dielectric anisotropy in the ferroelectric phases of $BaTiO_3$.[48]

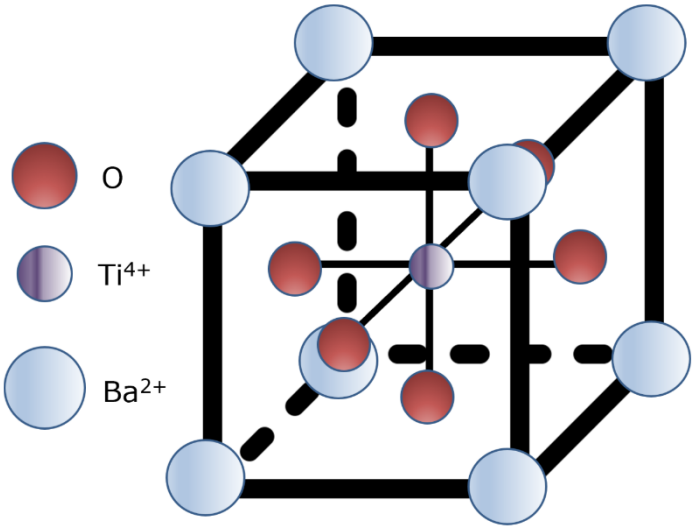

Figure 1.4. Schematic of $BaTiO_3$ in the cubic phase.

The ability to control $BaTiO_3$ nanoparticle size and morphology during its synthesis is vital to many applications that rely on these materials. For example, $BaTiO_3$ particles are currently probed as a base substance for ceramic materials with a high dielectric constant; high surface area contact between the different faces of the $BaTiO_3$ with a defined cubic morphology are ideal.[49] As such, literature shows motivation for developing syntheses of $BaTiO_3$ nanoparticles that control particle size as a means to maximize the surface area of the product, control shape to maximize the surface area in contact between particles, and regulate the particle surface chemistry to minimize the need for introducing surfactants or dispersants. Control of nanoscale particle growth is important in $BaTiO_3$ materials development.

Traditionally, $BaTiO_3$ powders have been prepared through solid-state methods at temperatures >1000 ºC but controlling the morphology of the final product that is on the nanoscale can be difficult.[50] Solid state reaction mechanisms are largely characterized by interfacial diffusion, as opposed to solvothermal and hydrothermal synthesis wherein the reactions between chemical species in the liquid phase often determine the reaction outcome Generally, controlling the size and shape of the final product has been best demonstrated using these wet chemical methods, via a bottom-up approach to preparing these materials. The benefit of the solvothermal or hydrothermal routes are the high pressures achieved during these methods that enables the crystallization of nanoscale materials while also using reagents that are normally not soluble in solution.

Using a steel pressurized vessel, solvothermal and hydrothermal syntheses involve the crystallization of substances at lower temperatures than would normally be possible through solid state syntheses.[51] This decreased temperature is enabled using high vapour pressures in a closed reaction vessel. These syntheses can produce single crystalline particles based on the solubility of minerals in water or other solvents at high temperatures and high pressures, utilizing temperature gradients within the reactor vessel. Solutes and reagents dissolve at the hotter portion of the reaction chamber, and at the cooler end these dissolved materials nucleate or deposit onto seed crystals, which eventually grow into crystalline products. While hydrothermal syntheses use aqueous solutions, solvothermal syntheses involve organic solvents. The wide range of solvents available make solvothermal syntheses more appropriate to investigate when developing methods to prepare $BaTiO_3$ with different morphologies.[52]

1.4.3. Radiation Stability of $BaTiO_3$ Nanomaterials

There are a limited number of studies of the effects of radiation on the stability of perovskites. Even fewer studies have been performed on the effects specifically for the neutron radiation of $BaTiO_3$, and only a few studies specific to these effects on nanoscale $BaTiO_3$. It was found that the irradiation of $BaTiO_3$ nanoparticles with γ-rays can increase its crystallinity and alter its particle size.[53] There was also an overall decrease in band gap energy with an increase in irradiation for doses up to 250 kGy. Researchers also looked at the stability of $BaTiO_3$ under γ radiation, in which the effects of radiation on the ferroelectric hysteresis loops of these perovskites were investigated.[54] Another study found that the crystallinity of $BaTiO_3$ against Ag^{7+} fared better when in the rhombohedral versus the tetragonal phase, up to a fluence of 1×10^{14} ions cm^{-2}.[54]

Another study looked at the effects of UV radiation on $BaTiO_3$ in terms of its optical properties, concluding that $BaTiO_3$ could be used as an efficient photodetector.[55] While another study investigated the effects of neutron irradiation on the ferroelectric properties of bulk $BaTiO_3$,[56] one work used X-ray diffraction to assess structural changes of macroscopic $BaTiO_3$ crystals, claiming to observe some atomic displacements within the lattice as a result of exposure to a fast neutron fluence of 1×10^{17} neutrons cm^{-2}. [57] There does not appear to have been previously published studies that utilize electron microscopy based analyses to assess the effects of neutron irradiation on the stability of nanocrystalline $BaTiO_3$.

1.5. Utility of a Neutron Generator for Radiation Experiments

1.5.1. Linear Neutron Generator

The source of neutrons in the transmutation experiments for the work of this thesis is a linear particle accelerator. These generators, in general, rely on a fusion reaction between a deuterium and tritium isotope, or two deuterium isotopes. One of these nuclei are accelerated towards a target that contains either deuterium or tritium, or a mixture of the two isotopes. Each fusion event between a deuterium and tritium produces an α particle, as well as a neutron with an energy, on average, of ~14 MeV, as depicted in Figure 1.5. This energy contrasts with a fusion event between two deuterium isotopes that forms a ^{3}He atom and neutrons with an average kinetic energy of 2.5 MeV. There is also a competing reaction in the deuterium-deuterium reaction in which a proton and tritium atom are produced. In either case, the emergent free neutrons can be captured by atoms and can participate in nuclear reactions, such as the ^{32}S(n,p)^{32}P reaction. The generator employed in this work produces neutrons at the energy of ~14 MeV.

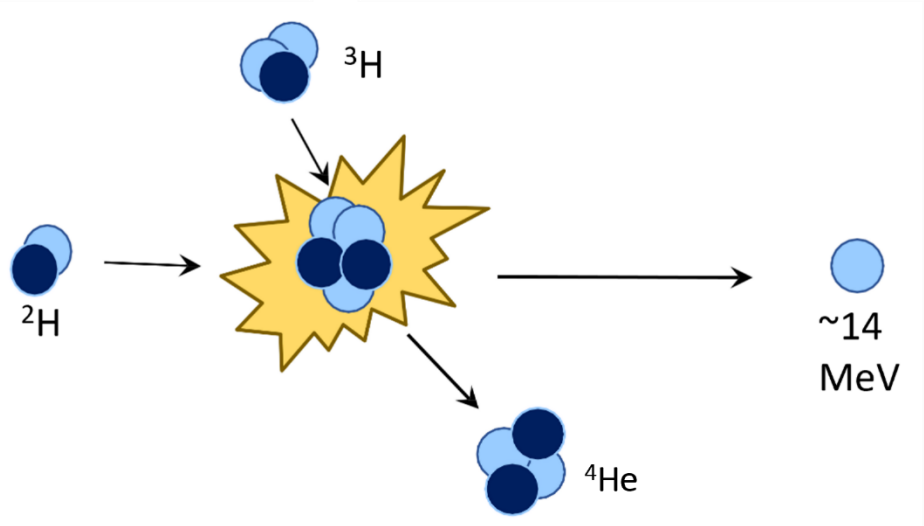

Figure 1.5. Schematic of a neutron generated from a deuterium-tritium fusion reaction.

1.5.2. Determining Theoretical Yield of Radioactivity

The fluence at a particular distance from the neutron source, assuming a point source, can be calculated using Equation 2. The yield produced by the generator during

irradiation is 2.1 x 10^8 neutrons s^{-1}, which has been verified by previous work that recently used the same generator while operating at the same output.[58] When this yield, ψ, is substituted into Equation 2 to determine the area density of the neutrons at a distance of 6 cm from the source, the calculated flux is ~4.6 x 10^5 neutrons s^{-1} cm^{-2}. This estimated flux, φ, is similar to values derived from previous work that recently utilized this generator under the same operating conditions.[58]

$$\varphi = \frac{\psi}{4\pi r^2} \qquad Equation\ 2$$

The yield of radionuclide production from the bombardment of neutrons with a target atom can be predicted. Equation 3 depicts the yield of radioactivity under ideal conditions. This equation demonstrates that the amount of radionuclide produced depends on the amount of target atoms and their neutron capture cross-section, the decay constant of the produced radionuclide, and the flux of incident neutrons.

$$S = \frac{N_A \varphi \sigma_c \left(1 - e^{-\lambda t_i}\right)}{A} \qquad Equation\ 3$$

Equation 3 solves for the activity of a sample after irradiation by neutrons, in Bq per gram of target material (*S)*. N_A is Avogadro's number. The term, *A*, is atomic weight. The term, φ, is the flux of neutrons per s^1 cm^2 was as obtained from Equation 2. The term σ_c is neutron capture cross-section of ^{32}S in the $^{32}S(n,p)^{32}P$ reaction and was estimated to be 0.25 barns (0.25 x 10^{-24} cm^2). The value used is determined from previous literature involving experimental data.[59] λ is the decay constant and is specific to the decay mode of each radioactive nuclide. The term t_i refers to the length of irradiation. The units of predicted yield are in Bq/g. One becquerel or Bq is a measure of one decay event per second.

By using Equation 3 to predict the amount of radioactivity produced from the exposure of a sample to neutron radiation, there is the assumption that there is no variation in the power of the neutron source (i.e., from the neutron generator). We also assumed that there was no destruction of the product nucleus. This equation was used to denote ideal conditions for the $^{32}S(n,p)^{32}P$ reaction, as we felt that any deviations during the experimental process, such as flux in power of the neutron generator, to be relatively

negligible. Radioactive decay follows a statistical process. The equation also assumes the decay constant specific to ^{32}P decay. The probability of decay is a property of the atomic nucleus. Mathematically, this law is expressed as,

$$dN = \lambda N dt \qquad Equation\ 4$$

Where *N* is the number of identical radioactive nuclei present in a population and λ is the probability of decay per nucleus per unit of time. The term, *dt*, refers to a period of time. As such, the activity of this sample, as measured by the change of the number of radioactive nuclei, can be calculated from Equation 5.

$$A = \frac{-dN}{dt} \qquad Equation\ 5$$

The half-life indicates the degree of instability of a radioactive nuclide, and is related to the decay constant by Equation 6. The term, $t_{1/2}$, refers to the half life of the radionuclide.

$$\lambda = \frac{ln2}{t_{1/2}} \qquad Equation\ 6$$

The equations laid out above can be used to derive an equation for the exponential decay of radioactive nuclei,

$$N = N_0 e^{-\lambda t} \qquad Equation\ 7$$

where N_0 is the number of radioactive nuclei at t = 0 (i.e., the initial reference point in time), λ is the decay constant, and t is the amount of time passed since the initial time point. From this derivation, *N* can be solved for the number of radioactive nuclei remaining after a period of time, *t*.

The equations laid out in this section were used to determine the theoretical yield of radioactive nuclei produced in various samples as discussed in the later chapters.

The transmission of neutrons through a material can be described by Equation 8. Here, χ is the depth or thickness of the sample, while σ_t is the neutron absorption and scattering cross section. The term, N_s , is the atomic density of the target material.

$$I_\chi = I_0 e^{-N_S \sigma_t \chi} \qquad Equation\ 8$$

For example, the intensity (I_x) can be calculated for a sulfur sample with a thickness, of 1 cm using the total cross section for the absorption and scattering of neutrons in sulfur (2 barns),[35] and the atomic density, N_s, of sulfur in its rhombic form (3.8865×10^{22} cm^{-3}). The intensity of a ~14 MeV neutron beam after passing through this sample of sulfur is calculated to be ~93%. I_0 is the incident beam intensity.

A way to describe the travel of neutrons through a material is by their mean-free path length. This value is the mean distance travelled by neutrons in between interactions with different particles within the sample. One can find the mean free path (L) for a beam of neutrons, assuming target particles are at rest, using Equation 9.

$$L = \sigma_t N_S^{-1} \qquad Equation\ 9$$

Incorporating the same values for N_s *and* σ_t as those used in Equation 8, the mean free path length of the ~14 MeV neutrons travelling through the sulfur sample is ~ 12.9 cm.

1.6. Extraction and Separation of Phosphates from Sulphates using Ion Exchange Chromatography

If formation of ^{32}P is successful, the next concern is purifying the species for use in many applications; whether through chelating the nuclide for targeting specific locations in biological systems, or through encapsulation for a timed-based release into the biological system. These applications require ^{32}P to be free from impurities. In solution, ^{32}P will likely be in the form of phosphates, due to the high tendency for phosphorous to be present in an oxidized form. Unfortunately, sulfur can also be present in its oxidized form and separating sulfates and phosphates can be difficult; chemical separation methods (e.g., chelation or precipitation) usually fail to fully distinguish between the two

species and removal of one often results in the removal of the other species. While phosphate specific removal methods have been developed, the may result in removed phosphates that are not suitable to facile processing.

Removal of phosphates from an aqueous solution is a concern normally for wastewater treatment processes. The two main types of removal methods are physio-chemical and biological; though many variations and combinations between the two types are commonly used in water treatment. Chemical treatments normally rely on precipitation; wherein the addition of salts form removable solids through clarification and precipitation. These treatments can also, although to a lesser extent, remove sulphates as well from the solution. The issue with these methods is if you plan to use the phosphates later, the separation of chemically bonded phosphates is difficult and presents another step that must be overcome.

Biological methods use microorganisms that take up relatively high amounts of phosphates, stored for future use in energy production. All living organisms use phosphate containing compounds, such as adenosine triphosphate, in energy transfer processes through the dephosphorylation of these compounds.[60] Phosphates collected and used by these organisms limits the practical use of these phosphates to many applications.

More recently, ion exchange technologies have been used in water treatment for phosphate removal. Initially, the resins were not effective at very low concentrations of phosphates (5 to 20 mg/L), particularly when there are higher concentrations of competing ions. Although not as well studied as previously discussed methods of phosphate removal, the highly selective nature of some resins has made this method more suitable for a number of applications, including the purposes outlined in this thesis. Pre-treatment of the exchange media with ferric oxides can increase the selectivity of a resin for phosphate ions.[61]

Hydrated iron(III) oxide nanoparticles have shown selective adsorption for phosphates over sulfates as indicated in Figure 1.6. Strong base resins and hydrated ferric oxides (HFOs) provide sorption sites for phosphates, although HFOs are more selective for phosphates.[62] The quaternary ammonium functional groups in strong base resins partake in coulombic interactions with orthophosphates, as well as with sulfates.

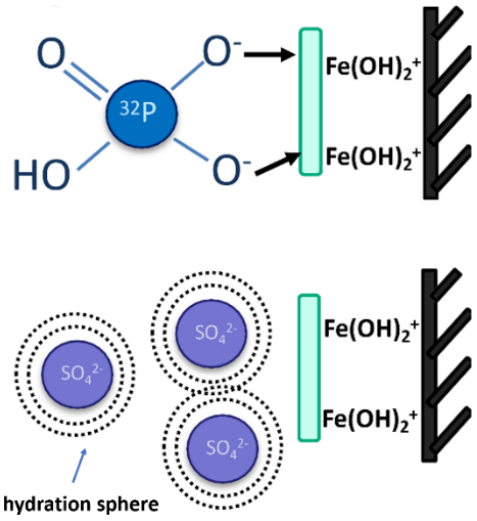

Figure 1.6. Schematic of the different complexes formed between ferric oxides and phosphates & ferric oxides and sulfates. Phosphates have ligand interactions with the adsorption sites, while the sulfates form outer sphere complexes with adsorption sites.

With HFOs, monovalent and divalent phosphates form inner sphere complexes with HFO surface sites and bind much stronger with the HFOs than the sulfates, which only form outer sphere complexes through coulombic interactions with the sorption sites (Figure 1.6.). The stronger binding with orthophosphates is due to the ligand interactions with the HFO adsorption sites. Polyvalent metals such as Fe(III), Ti (IV), and Zr (IV) demonstrate strong ligand absorption of HPO_4^{2-} and $H_2PO_4^-$ through inner sphere complexes.[63–65] Ferric oxides became the more promising candidate to impregnate ion exchange resins because, at some point, it became apparent that HFOs are relatively inexpensive and widely obtainable. As well, the literature on the synthesis of iron-based nanoparticles is relatively abundant.

Traditionally, HFO columns had low desorption and adsorption efficiencies. These columns utilized strong base resins and, as such, regeneration efficiencies were relatively low and could be considered inefficient (~20% to 40%). A resin containing a functional group that is a weak base, employing a tertiary amine versus a quaternary amine, does not bind as strongly to phosphate ions during the desorption process. During this process, a basic solution is run through the column to elute phosphates bound to the resins. The high pH promotes OH^- displacement of phosphate ions. A resin that is a weak base means that phosphates are released from their surfaces more easily. In addition, a study demonstrated a resin with a weaker base that had a higher adsorption capacity compared

to a resin that has functional groups that are a strong base, which is possibly due to less competition with interfering species such as sulfates.[66] While the work in this thesis does not include the purification of ^{32}P, this section provides a relatively efficient method for doing so and motivation for evaluating the method in future work.

1.7. Objectives of the Thesis

The objectives of the thesis are to explore the potential roles of nanomaterials in radiation studies. This work aims to develop sub 100 nm sulfur particles of a uniform size and shape, followed by their irradiation under neutrons to induce ^{32}P formation. Ideally, extraction of ^{32}P particles will not only be feasible, but we sought to demonstrate an easier extraction of ^{32}P from the nanosized S compared to commercially available, powdered forms of S. Such an outcome would confirm yet another advantage that nanomaterials have when employed in nuclear and radioisotope industries to produce radioisotopes.

In addition, studies have shown the self-healing properties of nanostructured materials against radiation-induced damage. In particular, perovskites have been studied for radiation tolerance, largely because of their applications in radiation heavy environments, such as in solar cells. Despite a wide range of irradiation studies in perovskite materials, including $BaTiO_3$, there are none evaluating the effects of fast neutron irradiation on nanocrystalline $BaTiO_3$ in terms of stability in the crystallinity and structure- particularly using electron microscopy techniques. We aim to study the stability of these materials against irradiation with ~14.1 MeV neutrons at fluences up to 4×10^{10} neutrons cm^{-2}

Chapter 2.

Techniques for Characterizing the Effects of Neutrons on Synthesized Nanomaterials

Characterizing the effects of irradiation on synthesized nanomaterials involves certain forms of analyses by electron microscopy and crystallography-based studies. These techniques are dependant on the manipulation of electrons, as their extremely small wavelength allow visualization and mapping of nanoscale morphologies and crystal structures. These techniques are vital to observe changes in both nanomaterial structure and morphology as a function of neutron irradiation.

2.1. Transmission Electron Microscopy

In comparison to optical microscopes, the high resolving power in electron microscopy relies on a focused beam of accelerated electrons and a series of electromagnetic lenses to create a projected image of a sample. The de Broglie wavelength of electrons accelerated with a voltage of 200 kV is up to 100,000 times shorter than the wavelength of visible light photons, which is a crucial aspect of electron microscopes for visualizing nanoscale structures and materials. In transmission electron microscopy (TEM) multiple imaging modes can be applied to characterize nanoscale objects and include, but are not limited to, crystallography techniques and elemental analysis techniques.

The images in TEM are generated when high energy electrons from an electron beam interact with a sample positioned perpendicular to the beam. The source of electrons in the beam in the instrument used in this work is a field emission gun containing a tungsten wire with a fine tip (<0.1 μm) coated in a ZrO_2 layer. These electrons are accelerated by an applied electric field and focused by electromagnetic and magnetic lenses within a vacuum column into a beam in which the electrons move in paths that are parallel to one another. The scattering of electrons by the sample creates the contrast in TEM imaging. The electrons that pass through the sample are focused onto an imaging device. The TEM instrument used in this work employed a charged-couple device (CCD) camera as the image capturing detector. Incoming electrons transmitted through the

sample excite a scintillator (normally a single crystal), that emits photons. These photons are transferred to the CCD. The CCD contains a circuit of capacitors, which are used to read out the electron charges converted from the incident photons to produce an image.

The main components of a TEM include the electron gun, the vacuum vessel, electromagnetic and magnetic lenses, apertures, and the sample stage. The gun provides a collimated high energy electron beam. A system with the ability to create a vacuum is needed to increase the mean free path of electron interactions with gases; this is required to create a greater voltage difference between the cathode and ground without generating an arc. Increasing the mean free path also reduces the collision frequency of electrons with gas atoms to negligible levels. The ability to re-evacuate the vacuum on a regular basis is required as the specimen holders are routinely inserted or removed from the system. The apertures are ring-shaped metallic plates and are employed to adjust the electron beam intensity, as well as to remove electrons that scatter at very high angles that can adversely affect the produced image.

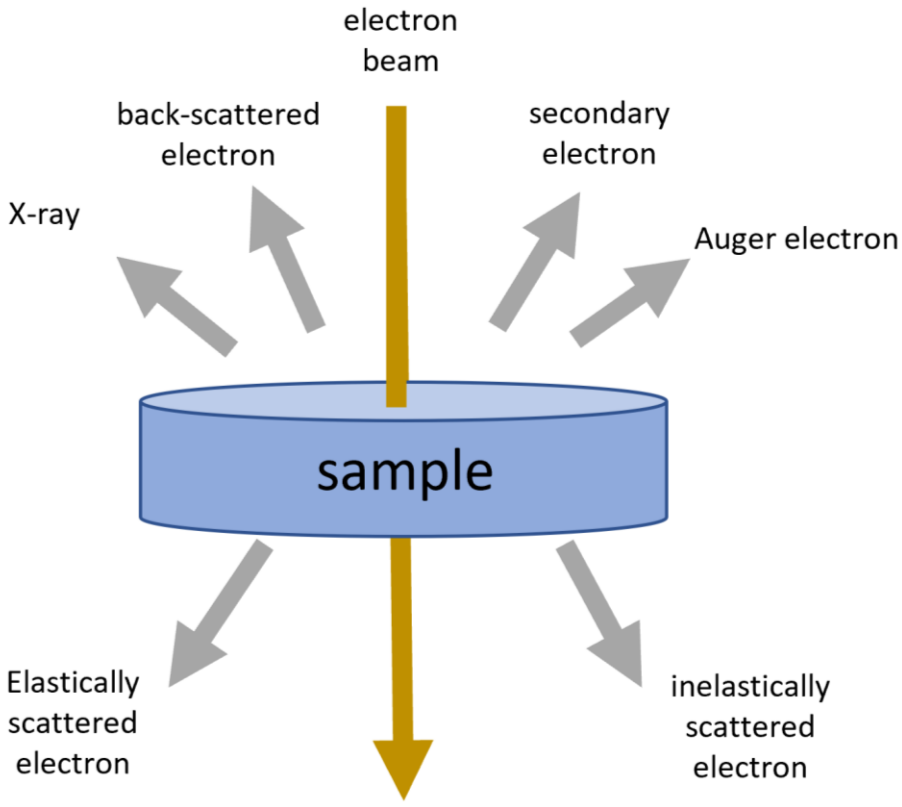

Figure 2.1. Schematic depicting the various signals that can result from the interaction of a high energy electron beam with a thin sample during electron microscopy.

Many electron microscopy systems, such as the one employed for the work in this thesis, are capable of scanning transmission electron microscopy (STEM) imaging as well. STEM is similar to TEM microscopy in that images are formed by electrons passing through a sample but differs in that STEM images are formed from the electron beam being focused to a relatively smaller spot size (as small as 0.05 nm) that is scanned over the sample. While the electron beam in the TEM imaging mode is focused perpendicular to the sample plane, STEM imaging mode has the beam focused at an angle to the sample plane before electrons converge to a focal point. There are multiple detectors for STEM imaging, such as the high-angle annular dark field (HAADF) detector, depending on the angle of the electron beam. Operating in the STEM imaging mode allows for analytical techniques such as energy-dispersive X-ray spectroscopy (EDS), which is often done in conjunction with the STEM imaging modes. These, along with HAADF imaging, will be covered in later sections.

As the electron beam is an ionizing source, interactions between the beam and sample can result in a range of signals that may be useful in determining sample structure and composition, as seen in Figure 2.1. Auger electrons are outer shell electrons that are ejected from the atom when energy is transferred to them. The energy stems from another electron transitioning to a lower energy orbital to fill a vacancy from an inner electron being knocked out by a primary, incident electron beam. Back scattered electrons result from elastic collisions between the incident electrons and atoms in the sample. Atoms with a higher charge scatter electrons more; the signal strength from backscattered electrons is proportional to the elements Z number. Compared to back scattered electrons, secondary electrons originate much closer to the surface of the sample, and result from inelastic collisions of the electron beam with the sample. They are largely from the surface as they have lower energy and can not travel as far through the material as back scattered electrons. Information extracted in electron microscopy is not limited to the electrons directly transmitted through the sample.

Sample preparation for electron microscopy involves pipetting ~2 μL of a dilute suspension of nanoparticles onto a TEM grid and vacuum drying this grid over night. The grids used in this work were copper, less than 5 mm in diameter and coated with formvar and a thin coating of carbon.

2.1.1. Crystallography Techniques

With a TEM microscope, there are numerous crystallography techniques that can be applied. Patterns obtained from the electron beam that are diffracted can provide information on the crystal structure of the sample. The wave-particle duality of electrons means that high energy electrons from the electron beam behave as waves, with wavelengths often in the picometers. As the spacing between atoms is about a hundred times larger, the electrons are diffracted by a crystal lattice that acts as a diffraction grating. These techniques each utilize a converging beam of electrons that are focused onto a portion of a sample to obtain a diffraction pattern. The crystallography technique used in this work was selected area electron diffraction (SAED). A diffraction pattern results from the interference of waves from the diffraction of electrons by the sample, with the distances between patterns (rings or spots) in the collected image of diffracted electrons correlated to the distances between the crystal planes of the sample.

The SAED technique obtains a diffraction pattern from a selected area; hence the term “selected area electron diffraction”. Different sized apertures can allow various portions of the beam to pass along the TEM column, allowing analysis of different portions of the sample. The resulting diffraction pattern can be a spot pattern corresponding to diffraction of a single crystal, or ring patterns that correspond to multiple, differently oriented, crystals within the field of view.

An SAED image, often depicted as a pattern of concentric rings, is the two-dimensional (2D) projection of the reciprocal crystal lattice and can be used to measure lattice constants, such as the distances between crystallographic planes. This distance is often distinct to a material and its crystal structure. SAED can, therefore, be powerful enough to determine the crystal structure and orientation of a sample. As such, SAED is commonly used for the determination of the phases and crystal structures in a sample. As SAED analysis can be performed in parallel with other electron microscopy techniques, no further sample preparation is needed than what is required for STEM imaging.

2.1.2. Elemental Analysis Techniques

Determining the elemental composition of synthesized materials or a particular portion of a structure are each important for confirming data that pertains to a sample.

There are various forms of spectroscopies in which quantitative and qualitative analyses of samples can determine the identities of elements present, as well as the mass of each element. In this work, the combination of STEM imaging using a HAADF detector along with EDS can provide elemental mapping of the species within nanoparticles.

In STEM imaging, the electron beam is scanned across the sample. A HAADF detector positioned below the sample detects any electrons that are scattered at angles >50 mrad.[67] This is in contrast with TEM imaging in which an objective aperture is used to detect only electrons that pass perpendicular to the sample plane. Because only electrons that are scattered at relatively high angles are detected in HAADF techniques, and since the angle of scattering is very dependant on the degree of electrostatic interactions between the nucleus of an atom and the electron beam, HAADF STEM imaging can provide a stronger sensitivity to heavier elements. There is a correlation between the contrast produced and the thickness of a sample, along with the atomic weight of the atoms that make up the sample. This means that HAADF may provide better contrast for imaging particular samples.[67]

An EDS analysis is often performed in parallel with HAADF imaging for elemental mapping. This technique is done in conjunction with scanning electron microscopy or STEM techniques, utilizing X-ray emission to identify the elemental composition of a sample. An atom has discrete energy levels pertaining to electron shells that governs the electron position surrounding a nucleus. An electron shell contains a fixed number of electrons. In EDS analysis, a beam of incident electrons knocks out electrons within an atom that are initially in their ground state, displacing these electrons from their original place within their shell in the atom. This sequence of events is depicted in Figure 2.2. Upon filling of this electron hole and release of energy from this relaxation process, a detector can capture the released X-ray and converts its energy into a voltage signal. A processor measures and integrates the signals created by these X-rays and an analyzer displays the signal for data analysis to allow a determination of the presence of an element. Despite some elemental overlap, these X-ray energies are generally characteristic to the elements present in a sample. For example, the Lα and Mα (for when electrons relax from their L and M shells) transitions for Ba are centered at 4.465 keV and 0.972 keV, respectively. The Kα and Lα transitions for Ti, respectively, are centered at 4.508 keV and 0.452 keV, respectively. And the X-ray emitted for the Kα transition of O is centered at 0.525 keV and for the Kα transition of S, it is centered at 2.307 keV.

The usefulness of an EDS analysis is so ubiquitous in research facilities across many fields such that electron microscopy equipment often comes equipped with these analyzers to detect and measure the X-rays generated from the resulting electron transitions to obtain elemental composition of samples. As such, the STEM instrument in 4D LABS at Simon Fraser University was the appropriate choice to evaluate the elemental composition of samples while also performing an imaging analysis of these samples. This system is relatively unique in that it has 4 EDS detectors, which makes it a more sensitive system than other systems with only a single EDS detector.

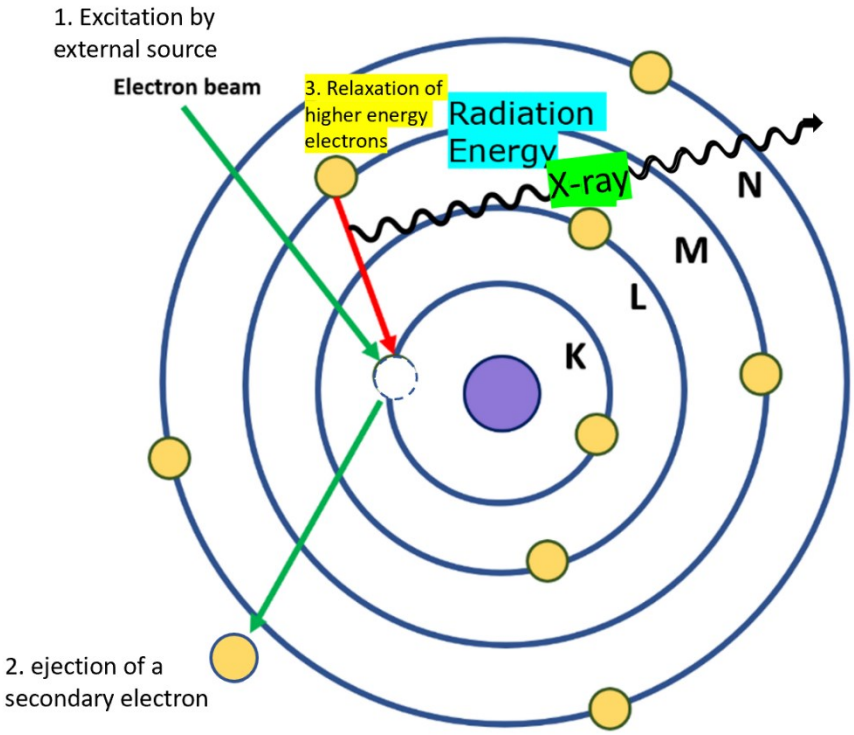

Figure 2.2. Schematic of characteristic X-ray generation when an outer shell electron relaxes to fill a hole a created by the ejection of a secondary electron as a result of an incident, external electron beam The letters refer to the electron shells.

2.2. Quantifying Radioactivity

Quantification of radioactivity relies on detecting and measuring the decay of radionuclides. A radioactive decay event results in the emission of energy, which can be detected and amplified by devices such as photomultiplier tubes. The signal from the photomultiplier tubes is converted by electronics within the instrument into a quantifiable measurement.

2.2.1. Liquid Scintillation Counting

The liquid scintillation counter (LSC) relies on radioactivity measurements as a result of mixing a radioactive sample with a liquid scintillation cocktail (which itself is described in Section 2.2.2). Except for γ decay, radioactive species undergoing a decay that releases energy in the form of particles that can be detected by the LSC. The cocktail used in LSC systems facilitates the transfer of energy from a decay particle to scintillators. The excited scintillators relax and emit photons, which can then be detected and quantified by photomultiplier tubes (Figure 2.3.).

The main parts of an LSC system are photomultiplier tubes (PMTs) and the electronics associated with the detection and quantification of the emitted signal, along with the sample holder. When measuring the radioactivity of samples, a decay event, such as the emission of a β particle, leads to the transfer of energy from the emitted particle to an organic scintillator within the cocktail. The excitation of the scintillators within the cocktail results in the subsequent release of measurable photons.

When the PMTs absorb the light emitted from the activated scintillators, the tubes transfer this energy into electrons ejected from the photocathode of the PMT through the photoelectric effect. These ejected electrons are kept under vacuum within these tubes. A focusing electrode directs the electrons under vacuum towards dynodes where electrons striking these electrodes cause a further emission of electrons. The multiplicative effect increases the signal enough such that the electronics and software within the instrument can convert the stronger signal into an electrical pulse that is analyzed and can yield quantitative data. Scintillation based detection methods can be considered to be a linear process when two main assumptions are made: (i) the light output of the scintillator is proportional to the energy of the incident radiation; and (ii) the electrical pulse produced by the PMT is proportional to the emitted scintillation light. The efficiency of counting differs between isotopes, depending on the energy of the decay particle. A high energy β decay from ^{32}P results in ^{32}P having near 100% counting efficiency in LSCs; almost all decay events are detected.[68]

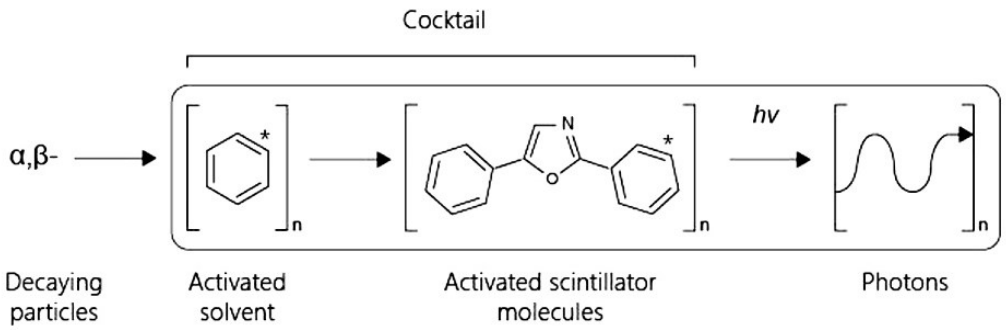

Figure 2.3. General schematic of the transfer of energy from a decay particle to the emission of a photon during scintillation counting used to quantify radioactivity of a sample.

2.2.2. The Role of the Liquid Scintillation Cocktail

The scintillation cocktail is a vital element to scintillation counting as the cocktail provides a means for the transfer and transformation of energy from the decay particle of the radionuclide to the PMTs within the LSC. The chemical composition of the cocktail is dependant on the four main components needed for scintillation counting: (i) the solvent; (ii) the surfactant; (iii) the primary scintillator; and (iv) the secondary scintillator.

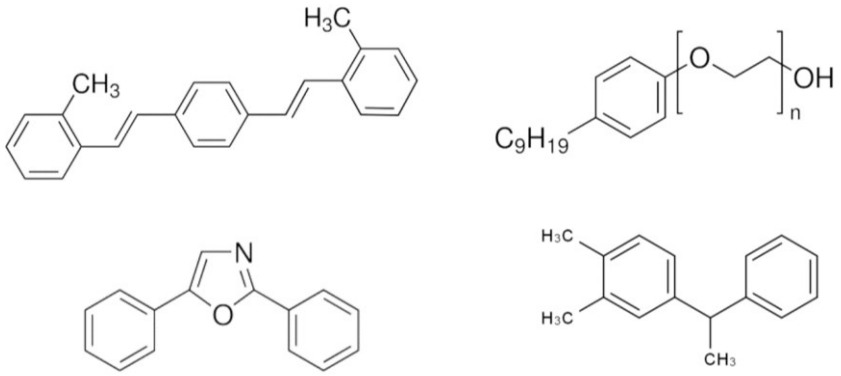

Figure 2.4. Structures of (top left) 1,4-Bis(2-methylstyryl)benzene (scintillator), (top right) 4-nonylphenyl-polyethylene glycol(surfactant), (bottom left) 2,5-Diphenyloxazole (scintillator), and (bottom right) phenylxylylethane (solvent) that can be used in the creation of scintillation cocktails.

An optimal solvent in scintillation cocktails would maximize the acceptance of energy from a radioactive decay event. The dense electron clouds in solvents such as toluene, xylenes, and benzene made them ideal solvents in scintillation counters. Unfortunately, the efficacy of these solvents was countered by their toxic and hazardous

nature. The relatively low boiling points and flash points, along with the numerous health hazards eventually led to their substitution with safer solvents. The most common solvents used in scintillation cocktails today are phenylxylylethane (Figure 2.4.), diisopropyl naphthalene (DIPN), and linear alkyl benzenes (LABs). These solvents have aromatic rings that provide the needed electron density to accept the transferred energy, but do not have the same hazardous properties of the classical solvents. The LABs were developed initially as a raw material for dodecylbenzene sulphonate, DIPN was developed as a base solvent for dye used in carbonless copy paper manufacturing, and PXE was a solvent initially developed as an alternative to the extremely toxic polychlorinated biphenyls used in transformer fluids.[69] The exact mechanism for how energy is transferred to the scintillators is not known but it is likely there is a dipole moment induced in the solvation shell, allowing direct transfer of energy between the excited solvent molecules and the scintillator.[70,71] However, this transfer requires close physical contact between the solvent, the decay particles (and, therefore, the radioactive sample), and the scintillators.

The surfactant within the scintillating cocktail is essential for facilitating this close contact between the decay particles of the sample and the solvent, for efficient energy transfer, before the energy is then transferred to the scintillator molecules. An appropriate surfactant can overcome differences in miscibility between organic and inorganic compounds in the sample and cocktail, allowing for the formation of a microemulsion that is: (i) clear for photon detection; and (ii) provides stable conditions that are necessary for counting decay over a sufficient period of time. A surfactant used in the experiments outlined in this thesis is 4-nonylphenyl-polyethylene glycol (Figure 2.4.). Most radioactive species of interest to this thesis are contained in aqueous solutions. As the solvents used in the scintillation cocktail are organic based species that are not miscible with aqueous solutions, a surfactant is needed to facilitate intimate contact between the solvents, the sample, and scintillators. When water is added to a cocktail, micelles are formed; water molecules are held within the middle of the spherical micelles, and the non-polar head of the surfactant is directed outwards into the organic solvent. When an aqueous radioactive sample is added to the scintillation cocktail, the aqueous solution can thus be dispersed within the organic solvent by the assistance of these micelles, and as a result the radioactive species are positioned in close proximity to the organic solvent that contains the scintillating molecules. The resulting microemulsion is required for an efficient energy

transfer from the decay particles to the scintillating molecules for conversion into photons that can be detected by the PMT.

The role of the scintillator molecules is to emit the absorbed energy from the decay particles in the form of light at a wavelength that can be detected by the PMT of a liquid scintillation counter. Because of this requirement, good scintillators should have a fast decay and a high fluorescence quantum yield; the ratio of the number of photons emitted versus the energy absorbed during excitation of the scintillating molecules.

In scintillation counting, two classes of scintillators are used: (i) the primary scintillator, which is the initial point of contact in the energy transfer between the solvent and scintillators; and (ii) the secondary scintillator, which can absorb the photons emitted by a primary scintillator and subsequently emit photons at a longer wavelength that can be detected by the counting instrument. The scintillation involved in these experiments are due to the delocalized π electrons in the interacting π bonds of the organic scintillators. Radiation can excite the delocalized electrons and their de-excitation leads to luminescence. The electrons within the PMT detector material absorbs the energy of these photons as a result of the incident photons and, through the photoelectric effect, an electron is ejected from the photocathode and further electrons emitted from the dynodes of the PMT during the initiated cascade effect to form a detectable signal that is used to quantify the decay events. The primary and secondary scintillators used in these experiments are 2,5-Diphenyloxazole and 1,4-Bis(2-methylstyryl)benzene (Figure 2.4.), respectively.

Chapter 3.

Synthesis of ^{32}P from Neutron Irradiation of Sulfur Nanoparticles

3.1. Introduction

Figure 3.1. shows the desired outcomes using nanoscale sulfur for the creation of ^{32}P radionuclides in this thesis. Traditional synthesis of radionuclides, particularly for medical use, involves the processing of bulk materials that requires specialized handling, resulting in higher costs and longer processing times. Possibly, medical institutions can employ neutron generators in-house and generate their own medical radionuclides on demand, instead of being entirely dependant on the transportation of these species.

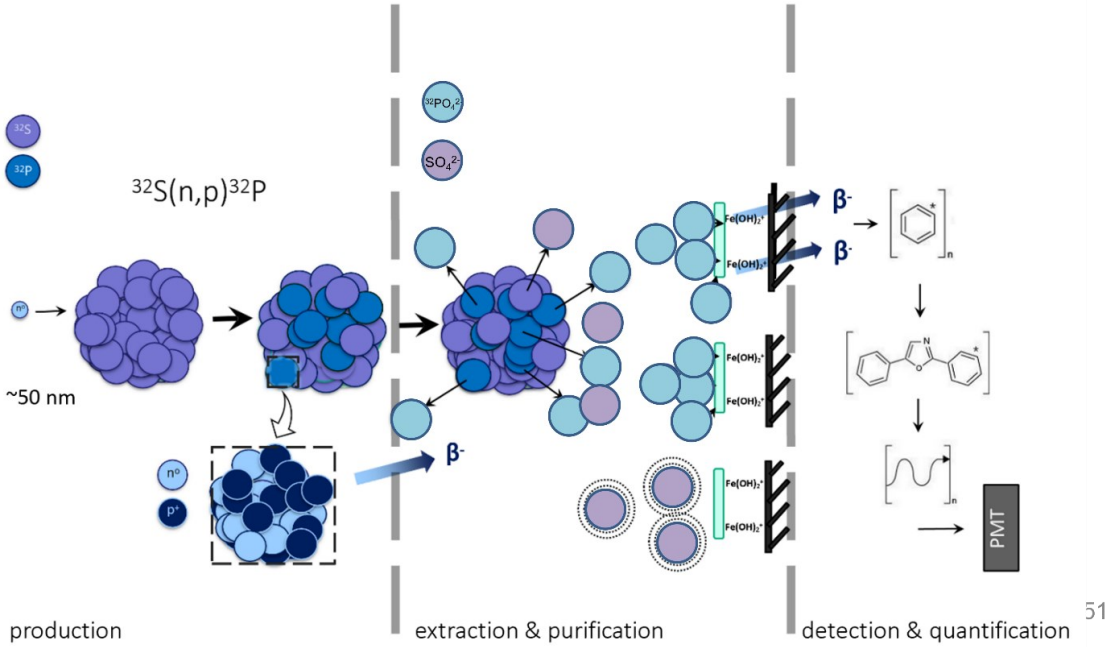

Figure 3.1. Schematic of for the use of nanosulfur for ^{32}P production, and its extraction using hydrated ferric oxides for selective phosphate removal before measurement of activity via liquid scintillation counting.

The acidic catalyzed decomposition of $Na_2S_2O_3$ (sodium thiosulfate) by HCl is seemingly straightforward, performed in many undergraduate courses as a demonstration of the concept of the rate of a reaction with an emphasis on the effects of [$Na_2S_2O_3$] on

the reaction rate. When the concentration of HCl is 0.2 M and the concentration of $Na_2S_2O_3$ is in the range of 0.01 M, it is observed that the rate of reaction is strongly dependant on the concentration of $Na_2S_2O_3$. However, the exact mechanism of forming colloidal sulfur across a wider range of reactant concentrations is not entirely known, nor are the kinetics fully elucidated.

This reaction is a redox (or reduction-oxidation) reaction catalyzed by protons. The ionic equation in acidic solution is:

$$2H^+ + S_2O_3^{2-} \rightarrow SO_2 + S + H_2O \quad Equation\ 10$$

For the thiosulfate ion each sulfur, on average, is in the +2 state. As a result of a disproportionation reaction, the products include sulfur in the +4 oxidation state as SO_2 (aq) and in a neutral state as S (s), which is associated with the S_8 molecule. The rate of the reaction is equal to $k[S_2O_3^{2-}]^t[H^+]^h$. The order t and h are not definitively known. From previous studies it is suggested that t is likely equal to 1. From published works, h = 0→1, depending on the ratio of $[S_2O_3]^{2-}$ and $[H^+]$. A study on the kinetics of this process using radioactive sulfur was performed in 1958, where concentrations of reagents were varied from 0.001 to 0.01 M.[72] This study proposed the rate expression to be:

$$rate = k[S_2O_3^{2-}]^{\frac{3}{2}}[H^+]^{\frac{1}{2}} \quad Equation\ 11$$

The dependence upon the acid concentration is explained in terms of a biomolecular reaction between bithiosulfate and thiosulfate. The thiosulfate can be visualized as undergoing a nucleophilic reaction displacing a sulfite ion, which then forms sulfur dioxide upon protonation. This reaction is a complex multi-step reaction. In the 1958 study, it was hypothesized that the reaction involves ions like $[HS_nO_3]^-$, where n = 1 → 9 after the reversible formation of a hydrogen sulfite ion, as seen in Equation 9. The $[HS_9O_3]^-$ then breaks down to a molecule of S_8 with release of hydrogen sulfite.

$$[HS_9O_3]^- \rightarrow S_8 + HSO_3^- \quad Equation\ 12$$

There is a chain lengthening process that favours the crown conformation due to the geometry of the sp^3 hybridization between the sulfur atoms. The chain of 8 atoms is the most energetically stable as it is more energetically preferred length for chains of S-S and most chains longer than this will fragment. There is a tendency for the chain to fold back onto itself, forming a crown conformation. After the S_8 species are formed, there are classical nucleation processes, aggregation, and/or Ostwald ripening that take place in the suspension, which result in the formation of sulfur particles.

The exact mechanism for the growth of sulfur nanoparticles during the acidic catalysis of sodium thiosulphate is not fully understood. Nanoparticle formation in solution involves a variety of processes that depend on the conditions of particle growth and the composition of the particle itself. Historically, the traditional model of growth of particles has involved nucleation models that are highly dependant on thermodynamic stability of the products.

Although the exact process is influenced by the reaction conditions, the general growth of nanoparticles has historically been described through the LaMer burst nucleation, followed by Ostwald ripening.[73] According to nucleation theory, there is an “instantaneous” nucleation within solution followed by a uniform growth of these nuclei in solution, which explains the formation of monodispersed particles. Two atomic nuclei coming together start the process of cluster formation. While most clusters can break apart, some will grow to a critical size in which they will continue to grow and not shrink. In Ostwald ripening, there is dissolution of smaller particles and deposition of material onto the larger particles in solution. The larger particles are thermodynamically more stable than the smaller particles.[74]

A more recent review of the nucleation mechanisms suggest LaMer’s theory was for appropriate weakly interacting systems, and that the theory is not as applicable to strong bonding systems that make up most of nanoparticle-based syntheses.[75] Furthermore, other theories, including those that are a modification of LaMer’s theory, have been proposed.[76]

Restricting further growth by limiting the reaction time and the use of surfactants to decrease the surface energy and growth of particles can result in smaller, nanosized sulfur particles. Sulfur nanoparticles have been described throughout literature. Yet, many

examples described in the literature show heavily aggregated particles with non-uniform morphology and size. Repeating the syntheses laid out in the literature did not result in the desired morphology, which for this thesis the target product was uniformly sized and spherical particles with an average diameter below 100 nm. It was, therefore, necessary to develop our own method for preparing the desired sulfur particles.

The role of surfactants in nanoparticle synthesis is to guide the growth of the particles, such as required for directing the growth of the desired shape and for generally controlling the rates of growth. The type of surfactant selected is a major factor in their mechanism of action. This selection of surfactant along with the concentration of the surfactant, the pH of the solution, and the ionic strength of the solution each impact the processes of particle nucleation and growth.[77] The relatively high surface area of nanoparticles results in their tendency to agglomerate. Surfactants cover and coat the surfaces of the particles and prevent agglomeration and aggregation. The mechanism of dispersion of nanoparticles by surfactants follow two main avenues: (i) electrostatic repulsion of ionic surfactants; and (ii) steric hindrance imposed by polymeric surfactants. These factors are balanced out by van der Waals forces in the local environment.[78,79] The later forces are the result of spontaneously induced dipoles of fluctuating electron clouds, interactions between permanent dipoles and induced dipoles, and the interactions between molecules with permanent dipoles. The effects of specific surfactants on the formation of nanosized sulfur particles will be studied herein.

Surfactants also play a role in directing growth of certain crystalline facets during nanoparticle formation. This is critical in the outcome of the final morphology of the particles. Surfactants may adhere preferentially to specific crystal surfaces, lowering the surface free energy of those surfaces and can even promote anisotropic growth or growth of a particular morphology.[80] For example, strongly adhered hydrophobic tails of surfactants can interact and take part in minimizing or promoting particle to particle interactions. If adsorbed preferentially on the surfaces of certain crystal facets, there can be an increase in the free energy of the surfaces that provides a driving force for the formation of a bilayer of surfactants that overall will decrease the free energy of these surfaces. This bilayer assists with minimizing interparticle aggregation through passivating specific facets, but other facets may not be efficiently passivated by the surfactants. This selective passivation of specific surfaces of the nanoparticles can result in a directed

aggregation or an oriented attachment of nanomaterials during their growth that lowers the free energy of the overall system.[81]

In addition to forming spherical particles of sulfur, a rod-like morphology was also desired such as that achieved through a facile process that is, ideally, quicker than what has been reported in literature. One study has reported truly rod-like structures, with a month-long synthesis.[82] Another study reporting nanorod syntheses shows structures that are more cuboidal in shape.[83] These two reported syntheses also involve heating solvents past 100 °C or use of an ozone treatment. Sulfur rods with a high length to width ratio could allow formation of the sulfur nanomaterials into a mesh-like (or membrane-like) conformation, wherein the high surface area of the nanorods combined with the porosity of the mesh-like form would enable an easier extraction of ^{32}P if water was to flow through the mesh-like assembly of nanorods. The ^{32}P could be collected as the radionuclides leach into the water, which would simplify the purification process. in addition to producing more uniform, spherical nanoparticles of sulfur, we also aimed to simplify the synthesis of the sulfur nanorods by producing these on a much shorter timescale than achieved in the prior art. Our goal was to have multiple materials to work with for demonstrating a tuneable approach to ^{32}P production using nanoscale sulfur.

3.2. Experimental

Synthesis of sulfur nanoparticles with diameters less than 100 nm was desired for ^{32}P production and its facile extraction. We also aimed to develop our own synthetic method for preparing sulfur rods. Sulfur rods could be useful as a good candidate for ^{32}P extraction; especially if they form a mesh-like assembly. Compared to spherical shapes, rod-like structures might not pack as tightly and, therefore, could provide more solvent access to their surfaces to allow for a more efficient extraction of ^{32}P.

3.2.1. Acidic Decomposition of Sodium Thiosulfate with Hydrochloric Acid

Uniform and dispersed sulfur nanoparticles were synthesized by adding 20 mg of 40 kDa polyvinylpyrrolidone (PVP) (Sigma Aldrich, Lot#: SLBK1476V) and 10 µL of Brij® L4 (Sigma Aldrich, Average Mn ~362, Lot#: MKCD2308) to 100 mL of an aqueous solution of 0.04 M $Na_2S_2O_3$ (Sigma Aldrich, 99%, batch#: 06830KC). To this solution, 0.8 mL of

~37% HCl (Sigma Aldrich, 36.5-38%) was added dropwise at a rate of ~1 drop per second. The solution was left to stir at room temperature for 2 h. The isolated particles were then washed a minimum four times by re-suspending with diH_2O (deionized water) and repeating the process of centrifugation and decanting of the solution. Subsequently, this wash procedure was repeated two more times with ethanol. The rinsed particles were stored in an aqueous solution of 0.01% Brij® L4.

For imaging, 2 µL of the particle solution diluted ~20x in isopropyl alcohol was drop casted onto a carbon TEM grid. The particles were analyzed by TEM and this method is the same for the S/TEM analysis of other samples.

3.2.2. Novel and Facile Synthesis of Sulfur Nanorods

In 50.0 mL of diH_2O, 0.791 g of $Na_2S_2O_3$ was dissolved. Then, 0.250 mL of Brij® L4 was added 0.43 mL of 12 M HCl was added dropwise, at a rate of ~1 drop per second. The mixture was stirred at room temperature for 2 h. The particles obtained from this synthesis were washed by the methods outlined in the previous section. Then, 50 µL of the synthesized particles were spun down by centrifugation and the supernatant was removed by decantation. To these particles, 300 µL of PC was added as a solvent. This sample was exposed to ultrasonication for 2 h while the sample was held in a plastic centrifuge tube. The average temperature of the water bath in the sonication system was ~27 °C throughout this process. After the exposure to ultrasonication, the particles dispersed in PC were held at room temperature for 1 week.

To a silicon wafer, 10 µL of the particle solution were left to dry at room temperature for 2 d. The particles were then analyzed via optical microscopy.

3.2.3. Neutron Irradiation of Sulfur Nanoparticles

The neutron generator used for the neutron irradiation studies was a Thermo Fisher P 385 deuteron-tritium generator with an average yield of 2.1 x 10^8 neutrons s^{-1}. The final operating voltage was 130 kV, with a beam current of 69.9 µA. The sulfur particles were irradiated for 24 h for a total neutron fluence of 4.0 x 10^{10} neutron cm^{-2} at a neutron flux of 4.6 x 10^5 neutrons s^{-1} cm^{-2}.

3.2.4. Determination of ^{32}P and Extraction from Irradiated Sulfur

After neutron irradiation, the irradiated nanosized sulfur (1.0 g) was fully dissolved in 15.0 mL 100 °C toluene and 1.5 mL of ddH_2O, while undergoing continuous stirring. The solution was left to equilibrate to room temperature, with the sulfur forming macroscopic crystals. The supernatant was then transferred to 12 mL of "Ecolite^{TM}(+) Liquid Scintillation Cocktail", containing phenylxylylethane as the solvent, 2,5-diphenyloxazole as the primary scintillator with an emission wavelength of 357 nm, and 1,4bis(2-methylstyryl)benzene as the secondary scintillator with an emission wavelength of 477 nm. The mixture was analyzed using a Beckman Coulter LS 6500 liquid scintillation counter.

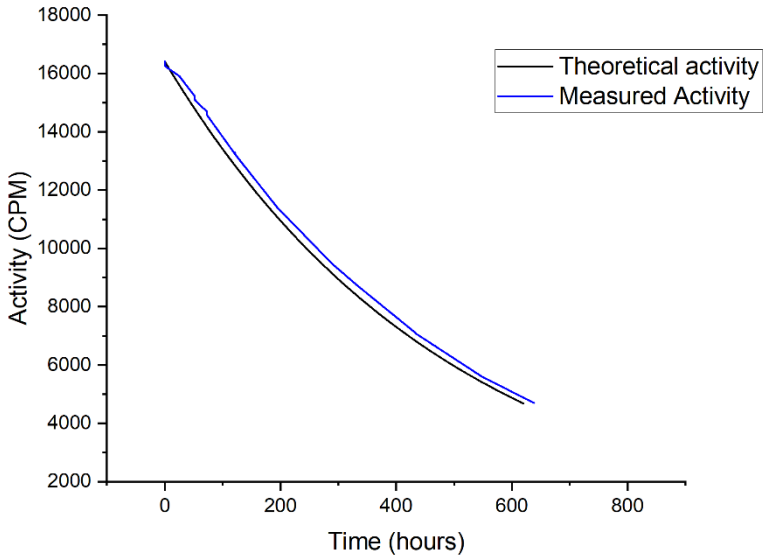

Figure 3.2. Decay curve constructed from measurements of a ^{32}P standard using the Beckman Coulter LS 6500 liquid scintillation counter (blue) with a comparison to the calculated theoretical decay curve of ^{32}P (black).

Preliminary experiments demonstrated that ~0.3 g of nanosulfur dissolves in 5 mL of toluene and 0.5 mL of ddH_2O at a temperature of 100 °C. Partial dissolution of the sulfur was utilized as a quick and facile method of assessing ^{32}P extractability from nanosulfur versus a commercially available sulfur powder. For this comparison, 1.0 g of irradiated nanosulfur and 1.0 g of the commercial sulfur were each separated into 3 solutions of 5 mL of toluene. These solutions were each heated at the same rate to 100 °C, held at that temperature for 5 min, vortexed for 30 s, and left to cool to room temperature. The supernatants were transferred to the aforementioned scintillation cocktail and analyzed

using a Beckman Coulter LS 6500 Liquid Scintillation Counter. As emission energies of ^{33}P overlap slightly with ^{32}P, there was a concern for the potential for inaccurate measurements of ^{32}P levels using this system. In particular, there was a concern that the measured activity could have contributions from ^{33}P radionuclides. The ability to accurately measure ^{32}P using the scintillation counter was confirmed by constructing the decay curve of a ^{32}P standard, as seen in Figure 3.2. The measured decay of the ^{32}P standard, in blue, followed closely with the calculated theoretical decay curve of ^{32}P, in black. Any presence of ^{33}P or the influence of its decay on the measured activity is negligible as ^{33}P and ^{32}P are in separate energy ranges (see Figures A4. and A5.) It is not known why the measured activity was consistently higher than the theoretical yield, however the decay curve for ^{32}P was still followed and it is possible the higher values were due to repeatability errors within the instrumentation itself.

3.3. Results and Discussion

3.3.1. Sulfur Nanoparticle Synthesis

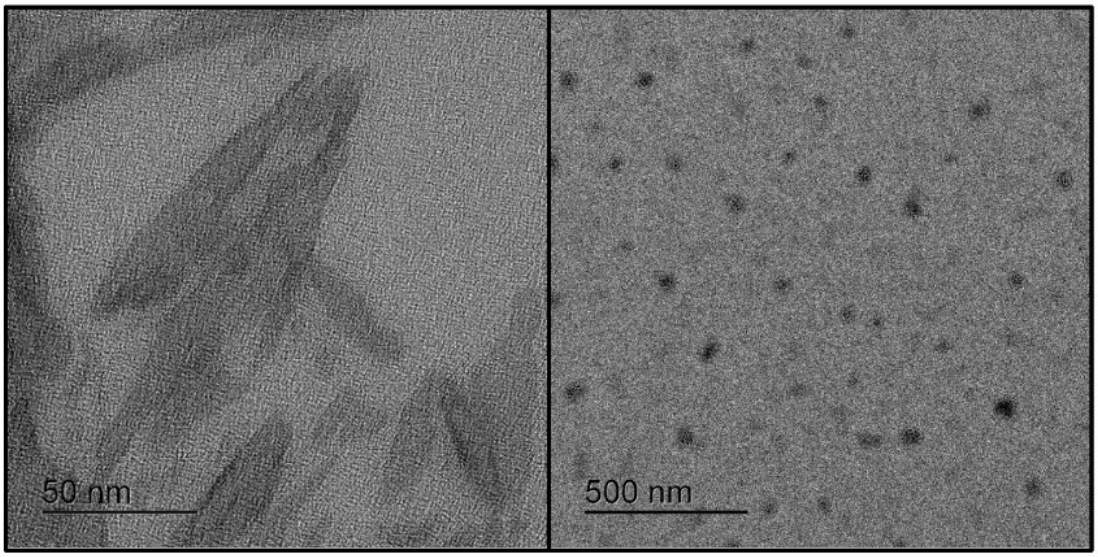

Figure 3.3. TEM images of sulfur nanoparticles synthesized without surfactants (left) and with (right) the presence of both PVP and Brij L4.

Previous literature on the morphology of uniform, nanoscale and dispersed particles synthesized by the simple acid catalyzed decomposition of $Na_2S_2O_3$ is sparse. From Figure 3.3., when comparing the left-hand and right-hand images, it is clear that some surfactant is needed to control the size and shape of the products. Our own attempts

at controlling size and morphology using various reaction times and various surfactants such as SDS (sodium dodecyl sulfate) and CTAB (cetyltrimethylammonium bromide) were not successful (images not shown); a wide range of particle sizes with no distinct morphology were obtained when using either of these surfactants. One method used PVP to obtain uniform and monodisperse particles.[84] Attempts to reproduce their results using the reported method were not successful and resulted in the formation of aggregated particles with sizes up to 500 nm in diameter. The addition of just 10 µL of Brij L4, a nonionic polyether, to 100 mL of the reaction mixture along with 0.02 wt% 40 kDa PVP resulted in the formation of small, spherical particles seen in Figure 3.3. (right-hand image).

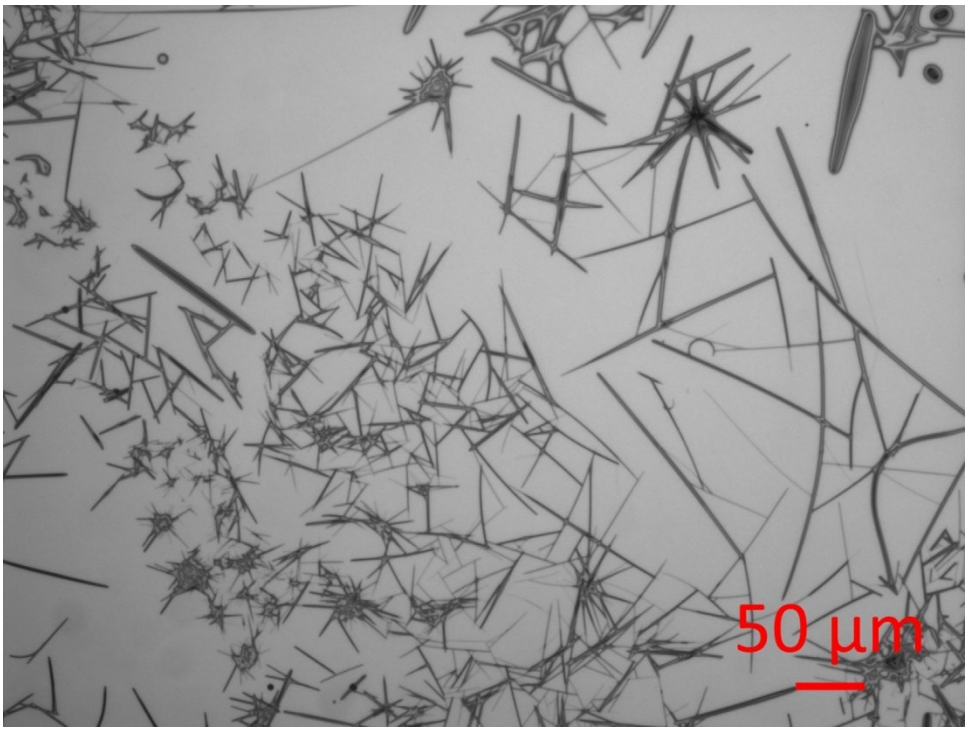

Figure 3.4. Image of sulfur rods as visualized using optical microscopy techniques.

Sulfur rods were also obtained (Figure 3.4.) through a facile process that is significantly quicker than what is reported in literature.[82] Other reports focused on structures that are more cuboidal in nature, although these were claimed to also be nanorods.[83] We aimed to develop a synthesis that was easier than the high temperatures and ozone treatment reported previously for the syntheses of sulfur rods.[82,83] The synthesis pursued in this chapter only requires nanosulfur, produced as outlined in Section 3.2.2., as a precursor material to be exposed to ultrasonication while these particles are

dispersed in propylene carbonate (PC). The solution was set aside and held at room temperature for 1 week. During that time, there is likely a self-seeding process that initiates crystallization. There would likely be an anisotropic growth within this system that results in the achieved rod-like morphologies, which has been seen in other chalcogenide systems.[85] These products could be easily imaged by microscopy techniques (Figure 3.4.). Since other solvents, such as ethanol and diethylene glycol, did not result in rod-like morphologies, it is hypothesized that PC had a role in controlling the growth of the particles by directing the deposition of sulfur onto the seeds. These preliminary results are interesting as most syntheses of particles that reported the use of PC as a solvent have resulted in the formation of products with only spherical morphologies. Future work will need to be done to develop and confirm a reproducible methodology, as determining the appropriate conditions for sulfur nanorod synthesis can be difficult. Considering that PC is one of the greenest solvents available, these preliminary results demonstrating the desired rod-like particle morphology using PC as a solvent is exciting.

3.3.2. Evaluation of ^{32}P Extraction

The theoretical ^{32}P activity from fast neutron irradiation of 1 g of sulfur is 6180 counts per minute (cpm), calculated using Equation 3. After 27 h, the activity of ^{32}P that was extracted from the irradiated sample of spherical, nanoscale sulfur was determined, by LSC, to be 2730 ± 30 cpm. Using Equation 7, the theoretical activity obtained 27 h after the irradiation should be ~5710 cpm. This equates to a yield of ~49%. For the neutron activation of a commercial sulfur powder, the ^{32}P activity measured was 1370 ± 30 cpm, which corresponded to a yield of ~31%. To confirm that the measured activity is due to ^{32}P decay, the measurements were taken again 143 h after irradiation. Using the activities measured at 27 h, the predicted activities for the ^{32}P extracted from the nanosulfur and commercial sulfur powder at 143 h were 2160 and 1390 cpm, respectively. These values fall within the error ranges of the activities measured for these samples at this time point (Table 3.1). The errors were instrumental error and propagated errors for the accumulation of activity of the three 5 mL aliquots for each sample, as well as errors between the three separate readings obtained for each sample. As the decay energies also match the rate of decay determined for the standard ^{32}P sample (Figure 3.2.), the measured activity is likely from ^{32}P decay.

Table 3.1. Measured activities of ^{32}P extracted from neutron irradiated nanoscale sulfur and a commercial sulfur powder. Samples were irradiated with 14.1 MeV neutrons for 24 h.

Sulfur type	mean diameter (nm)†	Activity (cpm)		approximate yield of activity (%)
		27 h‡	143 h‡	
Nanosulfur*	42 ± 14	2730 ± 50	2140 ± 30	49
powder	460 ± 90	1760 ± 20	1370 ± 30	31

*Synthesized sulfur (See Section 3.2.1.)
† Dimensions of the sulfur determined by TEM analysis
‡ Time = 0 at end of irradiation

As seen from Table 3.1, ~60 % more ^{32}P activity was extracted from nanosized sulfur compared to the commercial sulfur powder. The greater extent of extraction of ^{32}P from the smaller, nanosized particles suggests a more efficient removal of ^{32}P from the nanoparticles into solution. This difference in efficiency is likely due to the smaller particles having more of the ^{32}P exposed to the extraction solution on the surfaces of the nanoparticles due to their higher relative surface area, and/or the ease of dissolution of the nanosulfur relative to the larger particles in the commercial sample. The surface area for the average nanosized particle is ~5.5 x 10^3 nm^2 compared to ~6.6 x 10^6 nm^2 for a commercial sulfur particle. The relative surface area to volume ratios for these samples are roughly 0.14 nm^{-1} and 0.013 nm^{-1}, respectively. Sulfur is known to only be readily dissolved in carbon disulfide, a very toxic compound, at room temperature. It was, however, found that ~0.3 g of sulfur dissolves in 5 mL of toluene at 100 °C as an alternative solvent. Each sample of sulfur type was separated into 3 x 0.33 g portions. These portions for both types of sulfur samples were heated at the same rate to 100 °C, before being vortexed for the same amount of time. The solution containing the nanosulfur became transparent after heating and vortexing while the solution with commercial particles of sulfur still contained an obvious suspension of particles after the same procedure. These results were consistent across the treatment of 3 separate aliquots for both types of sulfur. About 30 s after the solutions are removed from the heat, crystals were observed forming in solution (Figure A2). The samples were allowed to cool to room temperature before the supernatants were extracted for the measurement of their ^{32}P levels. While there are variations outside the experimental controls, such as precise amount of force conferred onto the samples during vortexing, the large discrepancy in measured ^{32}P activity

extracted between the nanosulfur and the commercial sulfur strongly suggests that the extraction of ^{32}P from the nanosulfur particles is relatively easier to achieve.

Achieving a maximum extraction efficiency of 49% of the theoretical yield suggests the equation used to predict yield might not be an accurate portrayal of this system of study, or that there was a significant amount of ^{32}P remaining in the samples that was not extracted. While assumptions were made when calculating the predicted yield, such as changes in the flux from the neutron generator being negligible, the much lower yield than anticipated is likely more indicative that not all the ^{32}P was efficiently extracted in this process. One possible reason is that there was not enough aqueous solution in the extraction solvent for the ^{32}P to leach into. Future studies would involve fully dissolving the irradiated sulfur in adequate volumes of toluene to maximize extraction and obtain a true yield. While the solution of nanosulfur looked clear after heating to elevated temperatures, there may have still been particles present that were not visible to the eye that contained trapped ^{32}P. Also, while the solutions cooled to room temperature, the ^{32}P in the toluene solution may have adsorbed onto the surfaces of the sulfur crystals that formed in solution as a result of this temperature change. The use of methods for extraction of ^{32}P, such as that introduced earlier in this chapter, could also improve the yield.

3.4. Conclusions and Outlook

The work in this chapter builds upon the current state of knowledge in nanosulfur synthesis and their applications. In addition, the conventional means of ^{32}P production and processing is challenged with a possibly more efficient and cost-effective alternative, providing easier and quicker access to a medically and clinically valuable radioisotope. The available studies on developing nanoscale sulfur morphologies are fairly limited compared to the more popular metal-based materials, such as Au or Fe based materials.[86–88] It can be argued that this is due to the historically limited applications of sulfur-based nanomaterials. However, changes in attitude towards nanoscale sulfur applications such as an increasing interest in sulfur-based lithium ion batteries, and the concept of increasing the surface area to volume ratio of the sulfur for the ease of producing ^{32}P by extraction from neutron irradiated sulfur, provide motivation to develop syntheses for different nanosulfur morphologies.

This work produced dispersed, uniformly shaped nanosulfur that is not as commonly depicted in literature as other morphologies. The synthesis method involved a simple acid catalyzed decomposition of $Na_2S_2O_3$, while some other published methods used more complex steps involving techniques such as microemulsion techniques. Those that did publish monodispersed sulfur by decomposition of $Na_2S_2O_3$ had published morphologies that could not be reproduced in our own studies. Furthermore, nanorods were synthesized using a method that is quicker and that appears to be simpler than what is reported in literature. Rods up to 200 μm in length and 10 μm in diameter were synthesized in one week, using one of the most widely available green solvents, propylene carbonate. Sulfur rods will be pursued in the future for irradiation experiments, as they could be more efficient than spherical morphologies due to their difference in dispersion and packing in a solid form (e.g., upon settling from solution).

Finally, the work in this chapter demonstrated an easier extraction of ^{32}P from nanosulfur compared to larger sulfur particles obtained as a commercial powder. Irradiating nanomaterials for radioisotope production instead of bulk materials can be beneficial in terms of the labor and time required for processing the samples. The maximum extraction efficiency achieved in this demonstration of just ~49% still raises the issue of the location of the remaining amount of ^{32}P predicted following the irradiation step; likely ^{32}P remains within the sample. It is likely The efficiency of measuring ^{32}P using liquid scintillation counting is close to 100%, suggesting that nearly all decay events in the measured supernatants were accounted for.[68] It is possible that some ^{32}P had adsorbed onto the sulfur crystals formed while the solutions cooled to room temperature following the extraction process; if so, further work should investigate how the radionuclides can be better removed from the solution and from these crystals. In addition, multiple samples of sulfur should be irradiated to obtain replicate data for more statistical significance.

Chapter 4.

Radiation Tolerance in Nanomaterials

4.1. Introduction

Understanding the possible damage of the irradiated $BaTiO_3$ particles in this work requires a basic understanding of how radiation induced defects culminate in irradiated materials. Furthermore, as a general goal of the thesis to promote the value of implementing nanomaterials and nanostructures in the development of radiation tolerant materials, it serves a purpose to review the various self-healing properties of nanostructures and nanomaterials against radiation induced damage. A review of such works demonstrates the significant role of interfacial chemistry in such self-healing.

Development of materials, particularly for industrial uses, often requires a careful consideration of extreme environments that these materials might be exposed to. This is particularly true for applications in the nuclear and space industry where radiation can impact instrument durability and longevity. With the finite supply of natural oil and gas leading to an increasing interest in nuclear power as an alternative energy source,[89] design and development of durable materials in nuclear power production and waste has been an increasingly popular field. The growing number of technologies in space, as well as solar cells, means there is an increased demand for the development of materials that are tolerant to multiple forms of radiation from space, such as neutrons (thrown into space from collisions between cosmic rays and the surface of celestial objects that have no atmosphere, such as the moon), protons and different ions.[90,91] Technologies and devices in space, such as the International Space Station are constantly monitored for levels of cosmic radiation they are subjected to. The need for increasing safety and material longevity have led to the study of the role of nanostructures in radiation tolerant materials. Due to the extreme environments within nuclear reactors and in space, materials used therein must be scrutinized for their durability. We highlight the discoveries made in the field of interfaces in different materials, and their influence on radiation tolerance by the manipulation of defect production and distribution within the matrix of a material.

4.1.1. Radiation Induced Defects

Irradiated materials can undergo microstructural transformations that result from the impacts from bombardment with energetic particles such as neutrons, electrons, and/or ions. Studies investigating the radiation tolerance of materials most often have utilized energetic particles with energies in the range of keV to MeV.[92–95] At the atomic level, the chaotic events of a collision cascade during irradiation of a material can cause the formation of unrelated interstitials, dislocated atoms, and atomic vacancies. A specific type of dislocation is an interstitial, which occurs when the dislocated atom occupies a space that was previously devoid of an atom. A vacancy results from an atom being dislodged from its original place within a crystalline lattice, leaving behind an empty spot in the crystal lattice where the atom used to be located. This resulting pair of defects is often called a Frenkel defect, a defect where the two components are created (Figure 4.1.). As radiation-induced defects, interstitials are often referred to as self interstitial atoms, where the interstitial has the same atomic composition of those already present in the lattice. Both interstitials and atomic vacancies are point defects. These defects can agglomerate and most commonly form clusters. These clusters can include vacancy clusters, stacking fault tetrahedra, interstitial loops, dislocation networks, bubbles, and voids.

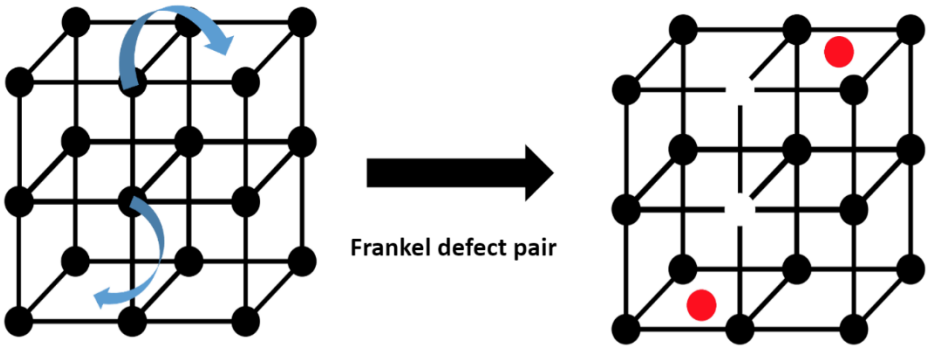

Figure 4.1. Schematic of Frenkel pair defects within a crystal lattice. When an atomic part of a lattice structure is displaced from its position in the lattice, the result is defects identified as interstitials and vacancies left behind, which are known as a Frankel pair.

Interstitial loops are largely a disk-shaped layer of atoms formed from the congregation of several free interstitial atoms in the bulk solid.[96] During the spontaneous recombination of interstitial defects and vacancies that form during radiation-induced exposure, the clustering of interstitials largely depends on how the atomic composition of

grain boundaries, on an atomic level, modify the spatial distribution of defects within the crystal structure, including at the grain boundary interface.[97,98] Dislocation loops and stacking fault tetrahedra are defects associated with the collapse of multiple point defects into lower energy defect structures.[99] Dislocation loops can result from the addition or absence of an extra plane of atoms within a crystalline structure, as shown in Figure 4.2. These loops can agglomerate and form dislocation networks. Stacking fault tetrahedra are pyramidal structures, comprised of a type of dislocation at the (110) edge of tetrahedron structures.[100] There is no material that is completely immune to radiation induced damage. In addition, the variety of radiation-induced defects and the subtypes of these are numerous.

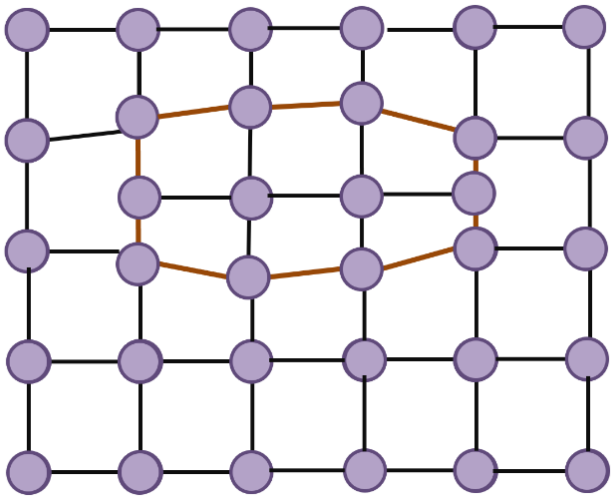

Figure 4.2. Schematic of an interstitial loop within an atomic lattice.

An important source of radiation damage stems from the initial atomic displacements upon bombardment of a material with irradiating particles. Irradiation events, on an atomic level, can seem erratic. There is usually a cascade of events that results from the initial collision by high energy particles, which in turn can form numerous atomic displacements and atomic vacancies. This cascade event is followed by a spontaneous recombination of interstitials and vacancies, often called self-healing. The degree of displacements from irradiation is dependent on the energy of incident particles and the displacement energies of atoms within the atomic lattices. The threshold displacement energy for sulfur is ~10 eV.[101] This energy is the energy required to move the atom from the lattice it is situated in. In $BaTiO_3$, the threshold displacement energies

for Ba, Ti and O are ~ 60, 10 and 40 eV, respectively.[102] These energies have implications on the effects of fast neutron radiation on $BaTiO_3$ materials seen in Chapter 5. The recoil energy of a typical atom from impact with a neutron at an energy of ~14 MeV can be in the range of MeV.[103] Furthermore, the recoil energy of any defects that remain following this process will constitute the radiation damage in the irradiated material. These defects can form higher tiered structures such as clusters and stacking fault tetrahedra. It was once assumed that once defect clusters are formed, the structures remained constant, while continuing to grow spatially.[99]

It is now known that cluster formation during irradiation is dynamic, with one type of structure often transforming into another.[104] It is considered to be more thermodynamically stable to go through the process of multiple vacancies before turning into stacking fault tetrahedra.[100] These transformations include the formation of stacking fault tetrahedra from vacancy voids, which is the most dominant form of vacancy cluster in many materials. Some studies postulate that the vacancy voids collapse into a loop structure (i.e., a disc of vacancies lying within a single crystalline plane), often at temperatures above 800 K.[105] At this temperature, the thermal energy is ~ 70 meV (compared to ~30 meV at room temperature). It is important to note that the binding energy in crystal lattices are on the scale of ~10 eV.[106] Other studies hypothesize that this collapse results into a direct transformation into a stacking fault tetrahedra, without going through the formation of a loop structure.[99]

The clustering of defects culminates in damage within a material that can include void swelling, where vacancies cluster to create a growing void within the material.[107] The formation of these defects can result in hardening of the material, where the defects prevent atomic movement within the crystal lattice. Too much hardening can result in an embrittlement of the material, due to the lack of mobility of atoms within the lattice. For nanostructured materials, radiation-enhanced hardening can be suppressed at length scales, ranging from a few atoms to nanoscale dimensions.

Hardening of materials results in an increase in the stress required to induce a plastic deformation of these materials, such as the permanent distortion of the materials from tensile, bending, or torsion stresses. An increase in material embrittlement can accelerate material failure in nuclear reactors, which decreases the lifetime of these materials and the systems they support, such as a nuclear power plant. Radiation

hardening largely occurs when defects form clusters and precipitates within a material, which can result in locking dislocation lines that resist the further movement of dislocations. As a result of radiation damage, hardening of a material is often interpreted in terms of either the dispersed barrier hardening model or the Friedel–Kroupa–Hirsch model. The selection of the appropriate model depends on the strength of the dislocation within the materials, such as its strength as an obstacle to further inhibit atomic movement within the matrix.[108]

The dispersed barrier model describes obstacles that intersect at a glide plane and prevent large-scale atomistic movements. The Friedel-Kroupa-Hirsch model is more appropriate for describing radiation defects that include a number of small defect clusters, such as the formation of dislocation loops, that form relatively weak obstacles to dislocation movements.[109] Often a combination of both models is used to determine the changes in hardening of a material following its exposure to radiation. The Friedel-Kroupa-Hirsch model is used to determine the component of hardening that results from dislocation loops, whereas the dispersed barrier model is more useful in determining the hardening contributions from all other types of defects.[110]

Another physical transformation that can result during radiation exposure is radiation creep within a material. Creep is a gradual but often permanent deformation of a material. This deformation often occurs in response to radiation induced damage. Creep results when a radiation damaged crystalline structure is subjected to additional damage and physical stresses. Usually, radiation-induced creep is accompanied by thermal creep.[108,111]

The culmination of defects and their clustering within a material can result in the formation of large-scale displays of radiation damage, such as the formation of bubbles and swelling. In addition, there are numerous studies that have confirmed the role of grain and interphase boundaries as sinks for radiation-induced point defects, which results in the suppression of void growth and swelling. Void growth and bubble nucleation is often the result of He implantation, which is a common phenomenon during the irradiation of materials.[112–114] Helium implantation is further discussed in 4.2.2

4.2. Interfacial Chemistry

The role of nanostructures in radiation tolerance is well known, but there is a growing interest by the scientific communities and various industries in the structural stability of radiation tolerant materials in different fields. As defect accumulation and annihilation is predominantly at some form of an interface, understanding interfacial chemistry is integral to enhancing radiation tolerance. In this context, interfaces include the grain boundaries between nanocrystals, additional interfaces within polycrystalline materials, and the interface between composite materials and the surrounding environment (e.g., liquid, gas, or vacuum). The benefits of nanomaterials in terms of improving radiation stability of a material on an atomic level largely stems from these interfaces. A significant component of this radiation tolerance is due to the ability of these materials to efficiently remove radiation-induced defects. This chapter discusses the fundamentals of the structural formation of radiation induced defects at different grain boundaries and provides examples of materials that have been demonstrated to exhibit radiation tolerance. For example, some metal alloys have been shown to have radiation tolerance, which often depends on their grain size, crystal structure, and grain surface energy. These alloys inherently have interfaces that play a role in how radiation defects interact with the material.

4.2.1. Grain size, Grain Boundaries, and Associated Surface Energies

Grain size and surface energies at grain boundaries are important factors in the ability of a material to tolerate radiation damage. These factors influence a material's ability to collect and remove defects through recombination events. In essence, defect density within a material decreases as its surface area to volume ratio increases.[115–119] A higher surface area to volume ratio in smaller grains facilitates a more efficient absorption of defects, which results in an interstitial-vacancy annihilation by recombination and ultimately damage recovery. Smaller grains also exhibit a lower stress at the grain boundaries within a polycrystalline matrix. Dislocations tend to pile up at these boundaries, and these dislocations can repel each other. The more dislocations that accumulate at a grain boundary, the higher the stress within the material. In materials with smaller grain boundaries, a higher stress can be tolerated before it results in material damage as a

larger number of dislocations can accumulate across more grain boundaries than in materials with larger grains.

The distribution of defects within a region exposed to cascade induced damage is determined by, but not limited to, grain boundary properties and crystallographic orientation of the neighboring grains. The grain boundary energy increases after irradiation, where the increase in energy is proportional to the number of defects within the grain.[120] The barrier to vacancy migration can decrease to as low as 0 eV at the center of a grain boundary, implying that vacancies can move along the grain boundary planes via barrier free processes. There is also a decrease in the energy of formation of interstitials and vacancies at these interfaces, which is another example of the influences of grain boundaries.[121] Additional observations have indicated that there is a further reduction in energy of formation for vacancies at damaged grain boundaries in comparison to the barrier to their formation at non-damaged boundaries.[122] These results suggest that an excess of interstitials at the grain boundaries can facilitate additional defect formation at these damaged grain boundaries. This influence of a damaged grain boundary to facilitate the formation and migration of additional vacancies towards these boundaries has been seen in previous studies with cubic metals, such as Cu.[123] Grain boundaries act not only as a barrier to defect migration and movement within the bulk material (*e.g.*, across grain boundaries), but the grain boundaries also serve as a region in which the defects can be mobilized—although only along these boundaries (*i.e.*, pinned to the grain boundaries), which prevents their free movement and coalescence into larger defect structures. The ability for a grain boundary to serve as a sink for defects depends on the rate of recombination events between vacancies and interstitials at the boundary, which is largely controlled by the diffusion of defects within the interface.

4.2.2. Multilayered Composites

Composites with nanoscale layered structures could serve as novel materials for potential use in structural materials and coatings associated with the materials needs of nuclear reactors. Metal composites with nanoscale layered structures can have very high mechanical strength and durability,[124–126] as well as increased resistance to radiation over pure materials.[127,128] Coarse grained polycrystalline materials with microscale grains can be thermally stable, but these materials are generally mechanically weak and are susceptible to radiation induced swelling and hardening.[111,129,130] Nanocrystalline materials

generally have a higher mechanical strength and an improved resistance to radiation damage due to their higher density of grain boundaries. Yet, nanocrystalline materials are not as thermally stable as polycrystalline materials with microscale or larger grains, and nanocrystalline samples can coarsen rapidly even at relatively moderate temperatures (*e.g.*, 300 °C for nanocrystalline Ni).[131,132] Materials prepared from nanoscale layered composites could overcome many of the limitations of both the nanocrystalline and microcrystalline materials. The preparation of composites with nanoscale layered structures could be scalable to suit the needs of the various industries and could even eliminate some current trade-offs in the selection of materials traditionally used or investigated by these industries. Just like the grain boundaries in nanocrystalline materials, interfaces play a major role in determining the radiation tolerance of composites prepared from nanoscale layered structures.

Theories postulating the mechanisms for the radiation tolerance of materials stem from the properties of interfaces, which are often described on the atomic scale. The properties of layered composites for nanoscale, thin layers arise from a series of interfaces. It is, therefore, important to understand in further details the properties that make certain composites more durable and capable of removing radiation induced defects than other types of materials as this understanding could lead to the preparation of new materials with enhanced properties. Established sinks for defects, such as the boundaries of interfaces, have been shown to alter the distribution of radiation-induced defects within a material and can often result in less radiation damage.[118,133] It is not surprising then that researchers have prepared materials from alternating the composition of layered structures with nanoscale dimensions to create model systems with a high density of interfaces to explore the effects of interfacial structures on the evolution of radiation induced damage. The interfaces between these layers could, potentially, serve in the same manner as grain boundaries for improving the radiation tolerance of a material.

In one example, a series of multilayered films were prepared from alternating layers of titanium nitride (TiN) and aluminum nitride (AlN) with thicknesses varying from 5 nm to 50 nm.[134] It was found that these multilayered composites had a better tolerance to ion-irradiation damage than that observed for layers of only AlN, exhibiting suppressed amorphization in contrast to the pure AlN materials. The interfaces within the multilayered materials served as defect sinks for defects arising from radiation induced damage, which prevented the accumulation of damage and an amorphization in the AlN. Interestingly, it

was determined that a critical thickness of the nanoscale films was between 10 to 20 nm for achieving an optimal improvement in the radiation tolerance of the composite. It was also determined there is a minimum thickness that was required to prevent severe interlayer mixing (*i.e.*, diffusion or mixing of atoms between the layers). This thickness did, however, vary as a function of the properties in each layer.

A separate study prepared structures with nanoscale layers from a composite of vanadium and graphene, which were then studied by experimentation and molecular dynamics simulations for probing their tolerance to irradiation with helium ions (He^+) at a fluence of 1×10^{18} He^+ cm^{-2}. This study confirmed that the graphene interfaces can spontaneously absorb defects produced during a collision cascade, where a single atom (V or C) knocked out of the crystalline lattice can displace other atoms leading to a cascade of events that form secondary defects in the material. The inclusion of graphene layers significantly reduced the radiation induced hardening of the vanadium.[2] In another study, it was determined that layered composites of vanadium and silver (alternating layers of V and Ag) were found to suppress radiation hardening that can result from irradiation with He^+.[135] The thickness of the layers evaluated in this study ranged from 4 to 7 nm. Hardness measurements were obtained for a series of V/Ag multilayered samples, as well as for bulk vanadium and silver. There was no change in hardness after room temperature He^+ implantation with layers <10 nm in thickness—the average diameter of the induced He bubbles. Previous work has determined that the hardness of a material can increase as a result of He^+ implantation, but that the effect decreases with a decreasing layer thickness of a film. Materials studied included Cu/V and Fe/W as layered materials with nanoscale thickness to each layer.[127,128,136] There was no change in the hardness of these materials as a result of He^+ implantation for a thickness <10 nm. In contrast, for layers over >10 nm in thickness, defects induced by He^+ implantation increased with increasing thickness of the layer. Composites of metal “nanolayers”, particularly at thicknesses that impede He bubble formation and movement, can have enhanced structural integrity against radiation-induced defects.

Investigations into the radiation tolerance of layered composites has largely focused on studies using irradiation with He ions and establishing how these composites alter a material’s resistances to typical damage that occurs from this irradiation, such as the formation of He bubbles and material vacancies. Of the materials evaluated in the studies with He^+ irradiation, a multilayered composite of copper and niobium (Cu/Nb)

composites are one of the most commonly studied materials. The Cu/Nb composites have been a focus of investigation for their potential use in fuel claddings. The use of these composites has been shown to increase the corrosion resistance of zirconium alloys[137] that are currently used for fuel claddings.[138] In Cu/Nb composites prepared at a larger scale, the majority of all the irradiation induced defects were mitigated by the interfaces between the layers.[139]

An investigation of the dispersion of He bubbles resulting from He^+ irradiation of copper films in comparison to a series of Cu/Nb multilayer composites found a significant decrease in the hardening of the layers with when prepared with a thickness <5 nm in comparison to those >70 nm thick.[140] This result was attributed to the dominant interactions between the bubbles and the interfaces formed by the layers. When the spacing between the He bubbles was much smaller than the thickness of the layers, there was a corresponding increase in the hardness and an embrittlement of the materials. In comparison, when the spacing between bubbles was similar to the thickness of the layers, there would be resulting structural deformation of the layers. These deformations were primarily the result of single dislocations crossing through the interfaces within the layered composites. These deformations are easier to annihilate than the deformations that result in bulk samples and, therefore, form structures that are less brittle. For pure Cu metal and for Cu layers with a thickness >70 nm, material hardening which results from the formation of He bubbles is significant. This effect increases with an increasing He content of the material through the Orowan hardening mechanism, which involves inhibiting the motion of dislocations.[141] When the thickness of the layers in the multilayered composite are small, the hardening of these materials is significantly mitigated regardless of the He concentration. Other investigations also observed a delayed nucleation of He bubbles and an overall retardation of bubble growth in sputter-deposited composites of Cu/Nb multilayered samples.[142] Multilayered composites of Cu/Nb have been demonstrated in a number of studies to exhibit an improved radiation tolerance and suppressing material failure (*e.g.*, embrittlement), as well as resisting large-scale structural deformations. The interfaces within the Cu/Nb composites remained morphologically stable after He ion irradiation, and no voids were observed to form following He^+ bombardment. This result was distinct from the defects observed to form at grain boundaries within either a material of only copper or niobium.

Material resistance to hardening and embrittlement from He^+ irradiation has also been studied for other multilayer composites. For example, a study of damage induced by He ion irradiation in multilayered composites of iron and tungsten (Fe/W) revealed the formation of 1 to 2 nm diameter He bubbles along the interfaces of these layers.[136] Radiation induced hardening of these composites was also found when the layer thickness was >5 nm, which possibly originated from the formation of dislocation loops and from the formation of He bubbles. In a separate study, He bubble growth, resulting from the implantation of He ions, was evaluated for composites of vanadium and silver (V/Ag) as a multilayered structure.[135] This study correlated a decrease in bubble size with a decrease in the thickness of the layers, suggesting an influence of the layered interfaces on bubble nucleation and growth. In terms of radiation induced hardness, no change in the hardness of these materials was observed in the multilayers with a layer thickness of <10 nm. The interface of the layers within these multilayered composites can act similarly to grain boundaries and serve as a location where bubbles can accumulate within the material. As a result, the increasing size of the bubbles can sometimes result in the bubbles being sufficiently large to facilitate boundary sliding and dislocation emission.

While interfaces can mitigate the damage induced by radiation, radiation can affect the interfacial properties and change their morphology. The impact of radiation on the properties of the interface should be considered when designing composites of nanoscale layers for creating radiation tolerant properties. For example, the effects of radiation on the interfaces can be assessed from changes to the properties of the layers. For example, there was a change in properties of a multilayered system of titanium nitride layers with amorphous boron carbon nitride layers upon irradiation.[143] In one study, it was observed that the thickness of the bilayer increased at low radiation fluences as a result of a global displacement of atoms in a direction perpendicular to the interfaces between these layers. In addition to potential structural and compositional changes, the interfaces of multilayered composites could exhibit additional changes to their properties. The ability of interfaces to act as sinks for defects to prevent the deleterious effects of the radiation on the material's overall integrity has led to the development of several composites from nanoscale layered structures with engineered features at these interfaces.

The degree of radiation-induced damage generated in a material is strongly correlated with the degree of self-healing within the material's structure. The ability to absorb defects and prevent formation of larger defect structures in the moments after

irradiation denotes the degree of radiation tolerance of a material. It has been discovered that perovskites have tolerance towards different forms of radiation, possibly more so than other similar materials. As such, different perovskite morphologies and crystallinities have been studied for their structural changes as a result of irradiation. These studies are, however, not complete. Perovskites, such as $BaTiO_3$, should be investigated further for their radiation tolerance to gain a better understanding of how to develop radiation tolerant materials that can be useful in applications that require exposure to relatively high levels of radiation. The work in this thesis, along with this review detailing the role of interfacial chemistry in radiation tolerant materials, seeks to provide the foundations for exploring the stability of various $BaTiO_3$ nanomaterials in future work.

Chapter 5.

Solvothermal Synthesis and Neutron Irradiation of Cuboidal $BaTiO_3$ Nanomaterials

5.1. Introduction

Studies of radiation tolerance in nanocrystalline compounds suggests a degree of structural stability against neutron radiation. In addition to nanocrystalline materials, titanium-based perovskites, such as $BaTiO_3$ have also been demonstrated to have enhanced radiation tolerance under forms of radiation including gamma, proton, and neutron radiation.[144–146] It follows that the perovskites of barium titanate ($BaTiO_3$) may have some forms of radiation tolerance that is worth investigating. To observe the effects of neutron irradiation on the structural stability of barium titanate, cuboidal nanoparticles of $BaTiO_3$ with a relatively thin morphology were synthesized before being bombarded with fast neutrons for up to 24 h. These particles were subsequently treated by ultrasonication to potentially enhance any radiation-induced damage to the surfaces of these materials. Electron microscopy and electron diffraction techniques were used to determine any significant changes to the structure and crystallinity of the particles.

5.2. Synthetic Techniques to Prepare $BaTiO_3$ Nanomaterials

Up until the past decade or so, the more common route of $BaTiO_3$ synthesis has been through the use of solid-state reactions. These syntheses were often accomplished by heating together barium carbonate and titanium dioxide, followed by a liquid phase sintering to form a densely packed solid mass.[147] Another method was through a high temperature calcination (heating to ~1,200 °C) using chemically derived intermediates.[148,149] Ball-milling has been another popular form of preparing $BaTiO_3$ powders in which bulk materials are ground down into smaller particles. However, along with lacking particle size control, these traditional methods have had issues in producing smaller particles sizes, such as on the nanoscale. $BaTiO_3$ nanomaterials, for many of their applications, often require better control over particle shape to obtain both a uniform size and morphology than that provided by processes such as ball-milling and solid-state reactions. Furthermore, the powder produced in these techniques can inherently have

relatively high amounts of impurities, which is typical of heterogenous solid-phase reactions. The impurities can enhance internal strain and decrease the crystallinity of the particles by stabilizing other phases of the structure.[150]

The motivation to better control the size and morphology of $BaTiO_3$ nanomaterials during their synthesis has been largely driven by the recent advances in the electronics industries.[151] The miniaturization of multilayered ceramic chip capacitors, alongside an increase in performance requirements, required chips to have a higher mechanical strength, a higher reliability, and a lower cost. To meet these demands, manufacturers needed to create these multilayered capacitors with uniform, ultrathin ceramic layers with well-defined microstructures. As such, wet-chemical methods, such as sol-gel processing, co-precipitation and micro-emulsion processes became more favoured in $BaTiO_3$ syntheses in recent decades.[151,152] The ability of these syntheses to better control the processes underlying particle formation have resulted in the formation of materials with a more uniform size and shape, and with a significantly higher purity.

5.3. The Role of Solvents and Surfactants in Hydrothermal and Solvothermal Syntheses of $BaTiO_3$

As with other materials, $BaTiO_3$ particles grown in solution can be guided and controlled using the addition of certain surfactants and solvents. The degree and manner of shape control provided during nucleation and growth depends on interactions of both the solvent and surfactants with the seed that eventually grows into a particle. Multiple studies have demonstrated the influence of surfactants and solvents in both hydrothermal and solvothermal syntheses of nanoparticles, particularly for metal oxides.[153–155] This work investigates the influence benzyl alcohol in comparison to the effects of ethylene glycol on the resulting morphologies of $BaTiO_3$ nanoparticles.

5.4. Methods for the Synthesis of Nanocrystalline $BaTiO_3$

$BaTiO_3$ has four polymorphs. The cubic and tetragonal phases of barium titanate are most commonly encountered in hydrothermal and solvothermal syntheses due to their stability at higher temperatures when compared to the orthorhombic and rhombohedral phases. $BaTiO_3$ crystals undergo a phase transition at ~130 ºC from the cubic phase to the tetragonal phase upon a decrease in temperature. The tetragonal phase is the

thermodynamically stable phase at room temperature.[156,157] However, as explained later on, the seemingly cubic phase morphology may remain even after cooling down of a $BaTiO_3$ crystal post synthesis. Nanoscale barium titanate of both cubic and tetragonal phases have been reported to be obtained from hydrothermal and solvothermal syntheses using both low temperatures and elevated temperatures reaching hundreds of degrees. The difference in the crystal structure of the tetragonal phase from the cubic phase is the inequality between the *a* and *c* axes in the former. It can, however, be suggested that the cubic phase crystals could actually be a pseuduocubic tetragonal phase. This result is common for solvothermal syntheses where -OH groups fill certain oxygen sites in the lattice, promoting the formation of barium vacancies, thus changing the unit cell parameters and forming a pseudocubic symmetry.[158] This pseudocubic phase can be more stable than the tetragonal phase at room temperature and can prevent the cubic-tetragonal phase transition upon cooling after synthesis.[158] Not only can the amount of -OH from reagents influence the final phase of the $BaTiO_3$ materials, but the grain size of the particles may also determine the phase that forms as a result of the synthetic route. As cubic $BaTiO_3$ cools below the Curie point, the crystal must distort to undergo a phase transition. With grain sizes larger than tens of micrometers, the distortion can be accommodated by twinning.[159] However, in small grains the twinning is not possible; internal strain prevents the cubic-tetragonal phase transition within individual particles or grains. As this work involves a variety of $BaTiO_3$ nanomaterials synthesized by solvothermal methods with different starting reagents and that result in particles of different sizes, these studies will not focus on a particular cubic or tetragonal phase. It is, however, important to distinguish the different phases of $BaTiO_3$ for future possible work in evaluating $BaTiO_3$ morphologies under irradiation.

A variety of particle sizes and morphologies for $BaTiO_3$ nanoparticles have been published using hydrothermal and solvothermal synthesis. This includes the formation of spherical, rod-like, and dendritic structures. Cubic morphologies with well-defined edges are very popular in these $BaTiO_3$ syntheses as a cubic shape facilitates the creation of high-density materials through self-assembly of these structures, such as for applications in $BaTiO_3$ based ceramics. Work presented in this thesis demonstrates a novel synthesis of $BaTiO_3$ cubes and other nanostructures of barium titanate.

5.5. Radiation Induced Damage of $BaTiO_3$ Nanomaterials

In general, perovskite materials have demonstrated a degree of radiation tolerance under a variety of forms of radiation. The study of the effects of radiation damage in $BaTiO_3$ materials reported in the literature is scarce and is even more so for these effects on nanoscale barium titanate materials. Since numerous materials have shown a relatively high radiation tolerance with the preparation of smaller grain sizes relative to their bulk counterpart, it would be valuable to study the radiation tolerance of nanoscale $BaTiO_3$.

As radiation damage stems from atomic displacements, understanding the movement of atoms out of their lattices to produce vacancies and interstitials is integral to understanding the effects of radiation-induced damage and the subsequent formation of defects in materials. The movement of oxygen atoms as a result of exposure to radiation is often studied; materials evaluated under irradiation with energetic particles are often oxides and oxygen can have a relatively low displacement energy.[3] It is anticipated that defects within barium titanate will include oxygen vacancies and, as a result, the formation of dangling bonds and related defect structures.

5.6. Experimental

5.6.1. Solvothermal Synthesis of Nanoscale Cuboidal $BaTiO_3$ in Ethylene Glycol

While the mechanisms of hydrothermal and solvothermal syntheses inherently aid in the formation of crystals that are smaller and that are more likely uniform in size and shape when compared to other methods that produce colloidal solutions, the selection of solvent can also aid in developing the desired morphology. Ethylene glycol is a solvent that has been used in the synthesis of a variety of nanomaterials.[160–163] The role of a solvent often is to serve as a surfactant by lowering the surface tension at the interface of the particles and to decrease the tendency of particle aggregation. Ethylene glycol's role as a reducing agent in nanoparticle synthesis has also been explored, particularly in

[3] The displacement energy is the energy required to permanently displace an atom from its lattice site.

promoting the nucleation and growth of Ag nanoparticles.[164] Some studies have even produced Pd-Ag alloys using ethylene glycol as a solvent and as a reducing agent.[165,166]

For the synthesis of $BaTiO_3$ nanoparticles, 8 mg of rutile TiO_2 (MK Nano, 99% pure, Lot#: 08/0124) was dissolved in 9.0 mL of ethylene glycol (Sigma Aldrich, >99%, Lot#: SHBM3293) and 25.7 mg of $Ba(OH)_2$ (Sigma, Aldrich, >95%) was dissolved in 1 mL of diH_2O. The two solutions were then mixed together, and placed in an autoclave at 150 °C and 180 °C for periods of 24 h to 96 h. Furthermore, these syntheses were repeated using $1/10^{th}$ the amounts of the Ba and Ti precursors, which were prepared as $1/10^{th}$ of the weight of precursors mentioned above.

5.6.2. Solvothermal Synthesis of Nanoscale Cuboidal $BaTiO_3$ in Benzyl Alcohol

In nanoparticle synthesis, benzyl alcohol is not a commonly used solvent in comparison to ethylene glycol or other alcohols. Studies demonstrating the production of $BaTiO_3$ based nanomaterials using benzyl alcohol as a solvent are even more rare. These studies typically depict the resultant $BaTiO_3$ materials with undefined shapes[167] or spherical morphologies. It has been suggested that the mechanism of formation of the spheres proceeds mainly through a novel pathway involving C-C bond formation between benzyl alcohol and a ligand from the titanium precursor.[168] Furthermore, benzyl alcohol does have reductive properties which could aid in seed formation during nanoparticle synthesis.[169] Alcohols in general are popular solvents in nanomaterial synthesis. The diverse range of alcohols can result in a variety of properties for these products and their formation, such as altering the mechanisms by which the particles are synthesized. For example, certain alcohols exhibit a better stability of the carbocation upon dissociation of the oxygen from the carbon.[170] As such, the hydroxyl group can be a good source of oxygen to produce metal oxides. This provides further motivation to evaluate benzyl alcohol as a solvent for the production of nanoscale $BaTiO_3$ particles.

For synthesis of $BaTiO_3$ nanoparticles, 8 mg of rutile TiO_2 was dissolved in 9.0 mL of benzyl alcohol (Alfa Aesar, 99%, Lot#: W29C061) and 25.7 mg of $Ba(OH)_2$ was dissolved in 1 mL of diH_2O. The two solutions were then mixed together, and placed in an autoclave at 150 °C and 180 °C for periods of 24 h to 96 h. Furthermore, this synthesis was repeated using $1/10^{th}$ of the amounts of the Ba and Ti precursors. In addition, 20 mg

of sodium dodecyl sulfate (SDS) and 20 mg of Brij® L4 were added as surfactants to some additional syntheses to control particle growth and particle morphology. As an anionic surfactant, SDS is commonly used in nanoparticle synthesis to control particle growth and as a template for particle morphology. Typical results from these syntheses are depicted in Figures 5.1. and 5.2. in Section 5.7.1.

5.6.3. Neutron Irradiation of Cuboidal $BaTiO_3$ Nanoparticles

The neutron generator used for the irradiation studies was a Thermo Fisher P 385 model with, for our experiments, a yield of $2.1x10^8$ neutrons per second. The particles were irradiated for 6 h and 24 h. The operating voltage was 130 kV, with a beam current average of ~69.5 μA. Samples were positioned 6 cm from the neutron source.

The $BaTiO_3$ particles used in the irradiation studies were developed using the method described in Section 5.6.2. with 0.8 mg of TiO_2 and 2.57 mg of $Ba(OH)_2$ dispersed in a solution of 9:1 (v/v) benzyl alcohol and diH_2O. The surfactant added to this reaction mixture was 20 mg of SDS. Sonication of the samples while held within a plastic vial (~2 mg in 3 mL of ddH_2O) after their neutron irradiation was achieved using a 40 kHz sonicator bath for a duration of 2 min.

5.6.4. Investigation of Radiation-Induced Damage via Crystallinity and Morphologies Changes

Previous studies have demonstrated the changes in the crystallinity of perovskites under certain levels of ion radiation, observing notable disruptions to the lattice structure. While other studies have shown changes to particle morphology after ion irradiation but no observable change in the crystallinity of the sample.[95] Clearly, the degree and physical form of damage to a material depends on various factors including the material properties and the type and energy of the incident radiation. Considering the lack of fast neutron studies on the morphology and crystallinity of nanocrystalline $BaTiO_3$, this work is important in probing their potential as radiation tolerant materials. In this work, we aim to evaluate significant changes to the crystallinity of nanoscale $BaTiO_3$, as well as obvious alterations to the morphology of these particles, such as damage to their surfaces as observed by TEM-based techniques.

5.6.5. Investigation of Radiation-induced Damage via Silver Deposition

The displacement of oxygen as a result of irradiation has been observed in materials. In oxides and oxygen containing materials, radiation-induced defects are often the result of oxygen displacement and depletion in certain areas of the irradiated material.[171] For example, it was found that oxygen deficient regions from the non-thermodynamically favourable displacement of oxygen can result from the energy imparted by an incident beam of accelerated Ag ions.[172]

While oxygen displacement is expected, we aim to look for the possibility of bond fragmentation. Bond breakage is possible from irradiation in various materials and under various fluxes of different types of radiation. It is possible that the degree of oxygen displaced within the lattice of the barium titanate culminates in fragmentation of the particles. Radiation has been known to induce a notable amount of dangling oxygen bonds in oxygen rich materials. In amorphous SiO_2, a resonance Raman band induced by X-ray irradiation was assigned to non-bridging oxygen holes, $\equiv Si\text{-}O\cdot$.[173] In 1960, γ-rays from cobalt-60 were shown to be capable of cleaving S-S bonds in an enzyme.[174]

Density functional theory (DFT) calculations indicate that ionic bonding exists between the Ba atom and the TiO_2 group of $BaTiO_3$, and that there is an f bond formed between the Ti and O atoms within the unit cell.[175] The formation energy of neutron induced point defects has been calculated previously. Authors of one study found that the energy of vacancy formation for O atoms within $BaTiO_3$ range from -0.15 to about 5 eV.[176] These energies suggest an atom displaced as a result of fast neutron bombardment can reach the threshold necessary for the formation of an O vacancy.

In metal oxides, the impact of radiation damage is strongly dependant on the form of radiation. X-rays and γ-rays do not significantly induce new structural defects.[173] Instead, radiation damage is influenced by the circumstances surrounding the impact of atoms by energetic particles above the threshold energy of Frenkel defect formation. Impact with highly energetic particles such as ions and fast neutrons can create enough energy for Frenkel defect formation. A study looked at the thermal stability of Frenkel defects in the anion sublattice of corundum (α- Al_2O_3) and found a co-existence of O and O^- atoms using optical absorption and EPR (electron paramagnetic resonance)

spectroscopy methods.[177] The EPR signal of oxygen interstitials were found in the form of O_2^- in irradiated corundum.

The evidence for bond breakage as well as O^- and O_2^- interstitials caused by ion radiation suggests that fast neutron irradiation of $BaTiO_3$ may lead to changes in structural integrity and can be led in part by bond breakage through formation of Frenkel defects pairs involving oxygen atoms. While there is access to electron microscopy at our institution, the ability to conclusively view changes in atomic lattices require equipment outside the capabilities provided through 4D LABS at Simon Fraser University. Developing chemical methods to view changes in lattice bonds may provide a more easily accessible and cost-effective route to viewing atomic displacements.

Using a solution of silver nitrate to view the degree of the selective reduction and deposition of Ag onto irradiated $BaTiO_3$ nanoparticles may be a plausible method as interstitial Ba and Ti species suggests possible sites for Ag reduction. Charged O species may also facilitate Ag deposition. For the reduction studies, 1 mg of the particles will be placed in 1 mL of a solution of 1×10^{-7} M $AgNO_3$ for 10 h under ambient light. Studies have confirmed the deposition of Ag onto dangling bonds, such as on dangling Si bonds.[178] These are non-bonding *sp* orbitals, and these dangling bonds can form when the periodicity of the Si in the lattice is disrupted. Given, as well, the displacement energies for Ba, Ti and O in $BaTiO_3$ (see Section 4.1.1.), the evidence reasonably suggests there should be a selective deposition of Ag onto sites corresponding to displaced O, Ba or Ti within the structure of the barium titanate following its irradiation with fast neutrons.

5.7. Results and Discussion

5.7.1. Solvent Effects on the Solvothermal Synthesis of $BaTiO_3$

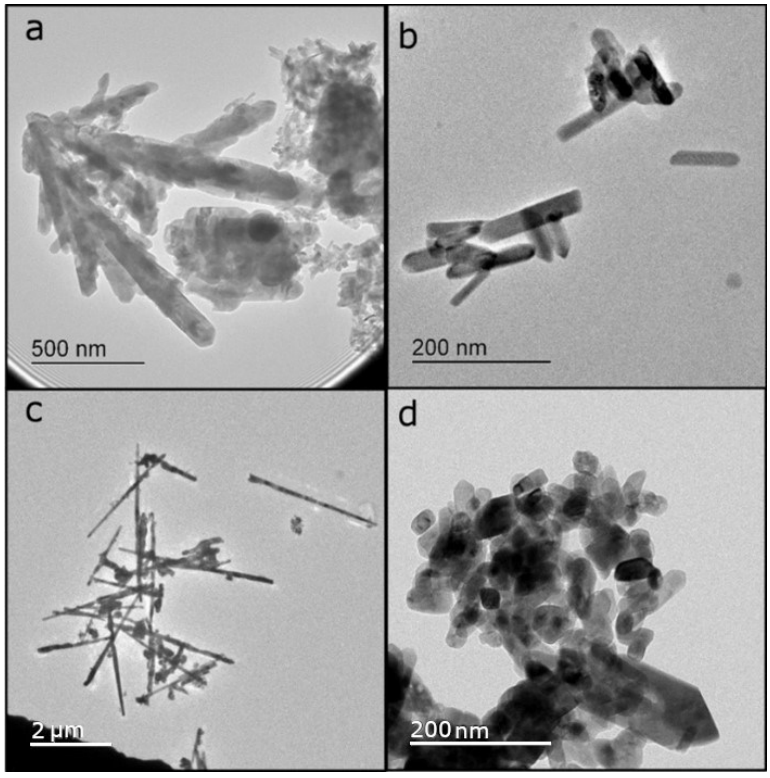

Figure 5.1. TEM images of $BaTiO_3$ particles prepared by a solvothermal synthesis in 9:1 (v/v) benzyl alcohol:diH_2O at 180 °C for 24 h (a) and 72 h (b), and after 24 h (c and d) using 1/10th of the concentration of precursors of conditions (a) and (b). SDS was used as a surfactant.

$BaTiO_3$ particle morphology produced in benzyl alcohol with SDS added as a surfactant suggests a strong tendency for the formation of rod-like structures, as shown in Figure 5.1. Particles produced in 9:1 benzyl alcohol:H_2O at either 24 h or 72 h resulted in particles with rods that were 100 to 500 nm in length and 20 to 100 nm in diameter. When repeating the same synthesis, but using 1/10th the concentration of Ba and Ti precursors [$Ba(OH)_2$ and TiO_2, respectively], and for a 24 h reaction time, rod-like morphologies were also observed within the sample. A representative result of this more dilute reaction concentration is seen in Figure 5.1 (d). However, a longer reaction time of 72 h vs 24 h did result in a significant decrease in the average particle size (*e.g.*, Figure 5.2). This result can be attributed to the influences of the reaction mechanism and reaction kinetics, which

suggest that the smaller particle size observed after 72 h is due to the partial dissolution of the larger structures that are initially formed in the solution.

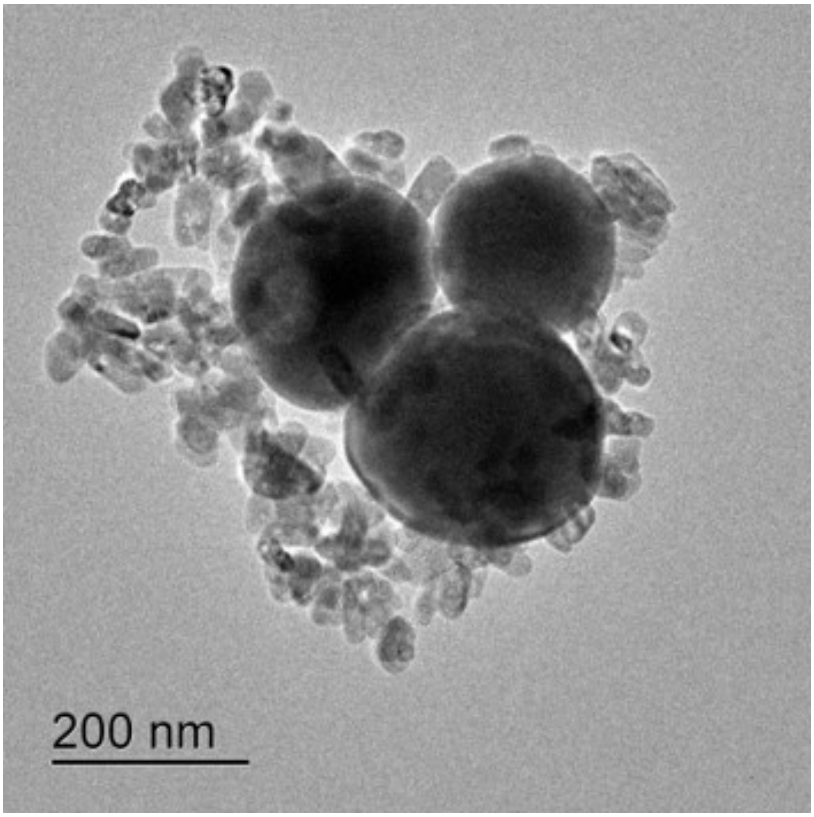

Figure 5.2. TEM image of $BaTiO_3$ particles prepared in 9:1 (v/v) benzyl alcohol:diH_2O after 72 h using 1/10th of the original concentration of precursors. SDS was used as the surfactant.

When the reaction period was then lengthened to 72 h, spherical particles resulted, as seen in Figure 5.2. The particles obtained at 96 h reaction time were similar to particles obtained at 72 h. Because these spheres were not seen in the syntheses using the original ten-fold precursor concentration, the resulting images are similar to the representative images in Figure 5.1. (b). Even at a reaction time of 72 h the precursor concentration appears to have a significant effect on the resulting particle morphologies. Note that the darker appearance of the spheres as observed by bright field TEM techniques is indicative of a relatively thicker morphology, such as when the particles adopt a spherical shape as opposed to having a thinner, plate-like morphology.

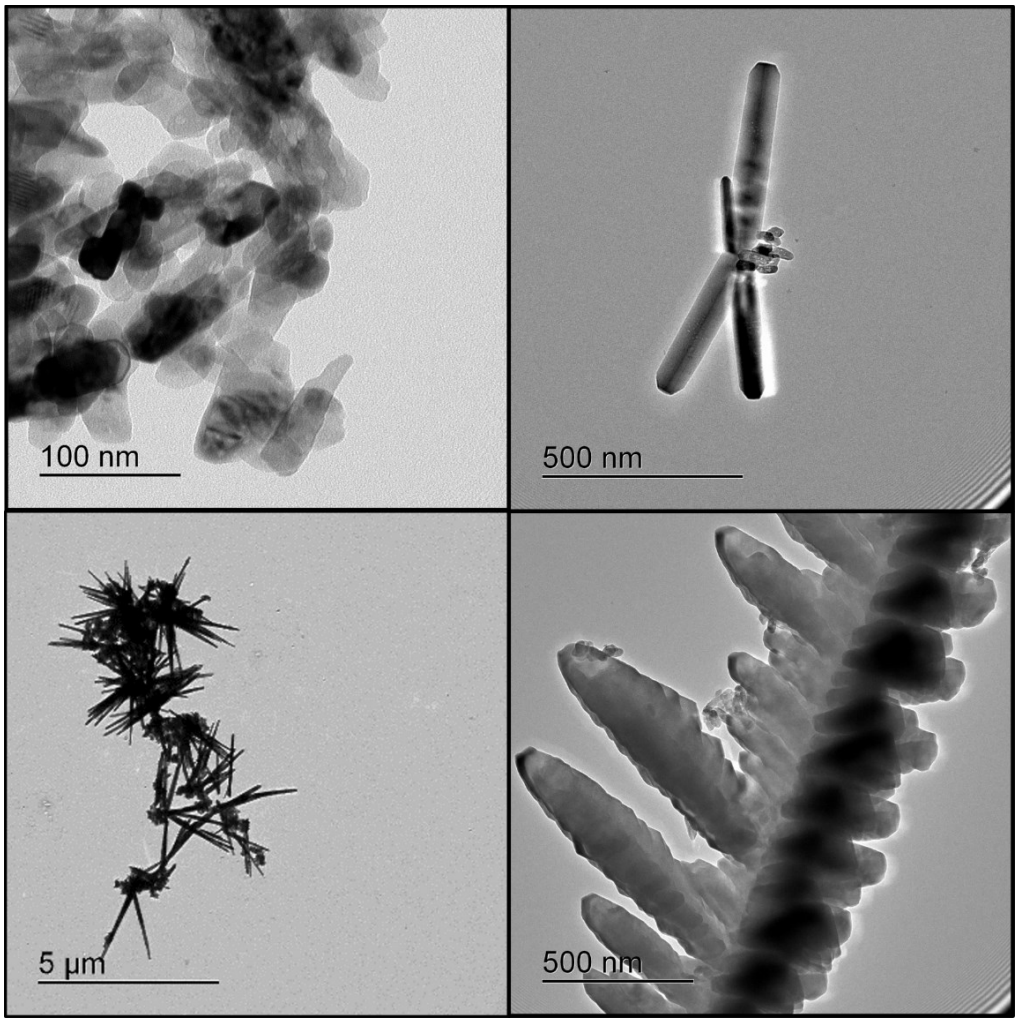

Figure 5.3. TEM images of $BaTiO_3$ particles prepared in 9:1 (v/v) ethylene glycol:diH_2O after 24 h using SDS as the surfactant. Top images depict particles produced using 1/10th the reagent concentrations in comparison to those prepared in the bottom images.

Figure 5.3. depicts $BaTiO_3$ particles prepared in a 9:1 (v/v) solution of ethylene glycol:H_2O that was heated for a period of 24 h. The top images and the bottom left-hand image are representative images of particles produced at 180 °C, while the bottom right-hand image shows a particle with dendritic morphology obtained at 150 °C. Furthermore, the structures in the top images were resultant particles prepared using 1/10th the concentrations of the Ba and Ti precursors compared to the structures in the two bottom images. This result is similar to the results obtained using benzyl alcohol as the solvent; smaller reagent concentrations resulted in an overall smaller particles size in the population. The structures produced at the higher temperature and using lower concentrations also appeared to be more uniform in size. While most structures produced

were rod-like in nature, $BaTiO_3$ syntheses involving ethylene glycol resulted in a much more diverse range of morphologies, compared to using benzyl alcohol.

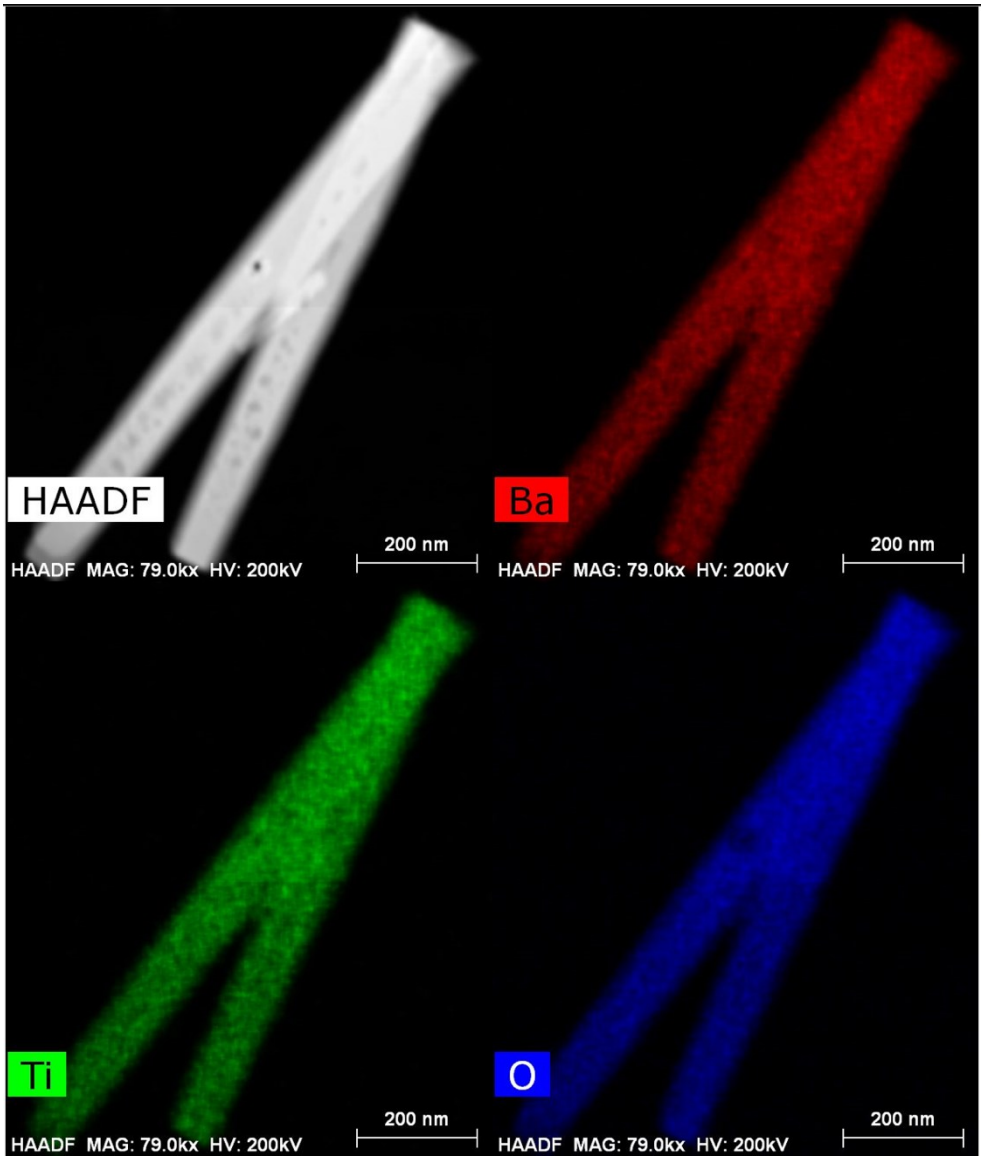

Figure 5.4. HAADF image (top left) and a series of EDS spectra of a $BaTiO_3$ particle that was synthesized in 9:1 (v/v) ethylene glycol:diH_2O at 180 °C using SDS as the surfactant.

Figure 5.4. shows the elemental composition of the $BaTiO_3$ particles produced in ethylene glycol at 180 °C with SDS as the surfactant. The HAADF image and EDS spectra confirm that rod-like $BaTiO_3$ particles were produced with well-defined edges.

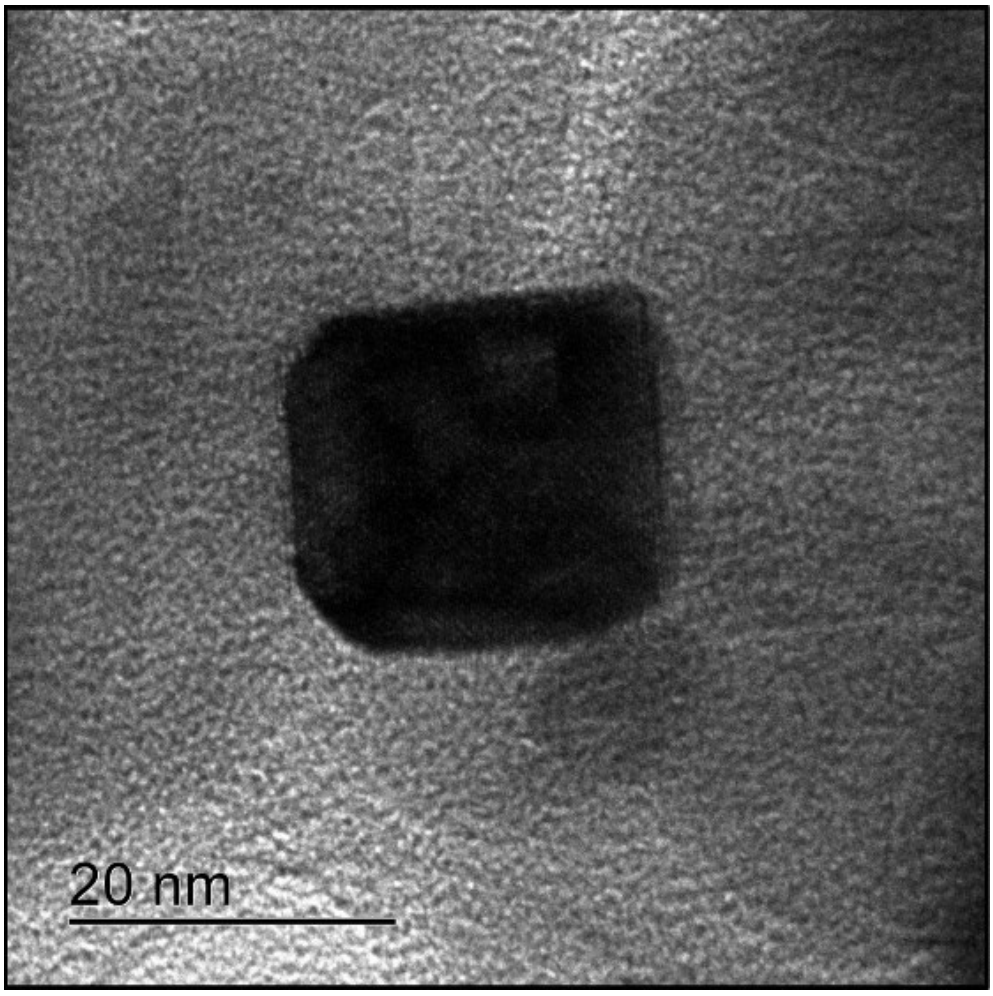

Figure 5.5. TEM image of a $BaTiO_3$ cube prepared at 180 °C for 72 h in 9:1 (v/v) benzyl alcohol:H_2O, using SDS and Brij L4 as surfactants in the reaction mixture.

A well-defined cubic morphology was obtained at a 72 h reaction time using both SDS and Brij L4 as surfactants. The cubic morphology seen in Figure 5.5 was produced at 180 °C. Note that benzyl alcohol has a boiling point of 205 °C. This work demonstrates a safer, lower temperature alternative to the production of nanoscale $BaTiO_3$ by solvothermal synthesis when compared to the majority of these syntheses that rely on solvents with lower boiling points. However, for the purposes of the radiation studies we sought to produce particles with a thinner morphology than these cubic morphologies to better observe any atomic or structural breakage stemming from radiation-induced damage. Thinner samples can better show fragmentation and atomic dislocation within their structures. Because TEM imaging relies on transmission of electrons through the sample, thick particles like the one in Figure 5.5 appear relatively dark and it would be

difficult to observe abnormalities in such structures. Furthermore, thinner structures could be more prone to fracture, which would enable an easier comparison of the relative degree of damage to different samples when comparing different irradiation conditions (e.g., different durations of radiation exposure). One of the more ideal structures were the particles produced at 180 °C after 24 h of solvothermal synthesis using SDS as the surfactant, such as those particles depicted in Figure 5.1.(d).

5.7.2. Investigation of Radiation-induced Damage via Silver Deposition

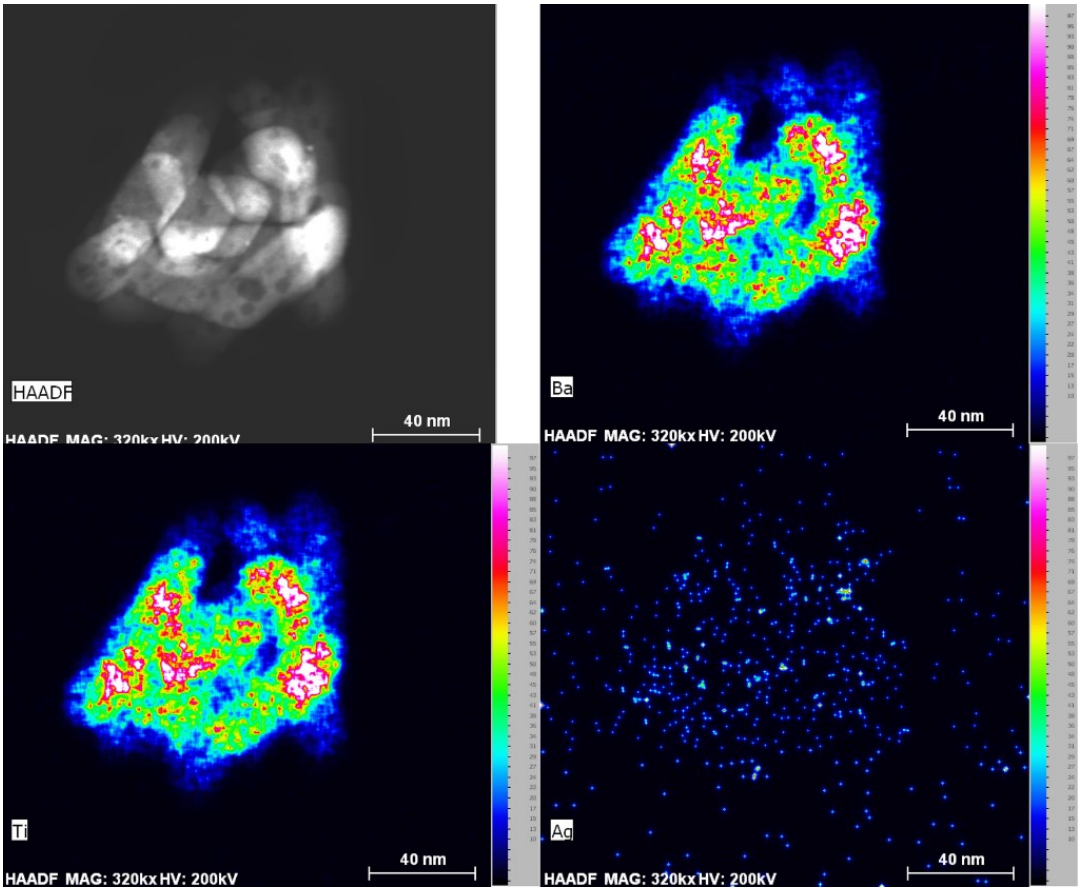

Figure 5.6. HAADF image and EDS heat maps corresponding to elemental spectral response for non-irradiated $BaTiO_3$ after its sonication for 2 min and incubation in a solution of silver ions (Ag^+).

To utilize silver deposition of radiation-induced damage, $BaTiO_3$ particles were kept in solution of Ag^+ for 10 h under ambient light. Figure 5.6. shows a HAADF image of $BaTiO_3$ particles in the top left section of the four quadrants in this figure. Included in this figure are heat maps of the elemental maps of Ba, Ti and Ag atoms distributed within these

particles. These particles were not irradiated with neutrons but were still incubated in a solution of Ag^+ ions as a control experiment. The morphology of the particles chosen for the irradiation studies were those that were around 50 nm in diameter or less, and with a relatively thin profile and a cuboidal morphology. The EDS spectra for the Ba, Ti and Ag depict that the relative presence of silver is minimal compared to the amount of Ba and Ti in these particles. The presence of silver in the vicinity to the $BaTiO_3$ particles is, however, higher than in the background, which suggests some deposition of silver onto the particles. This could result from a minimal exposure of the sample to ambient light that results in a photoinitiated deposition of silver.

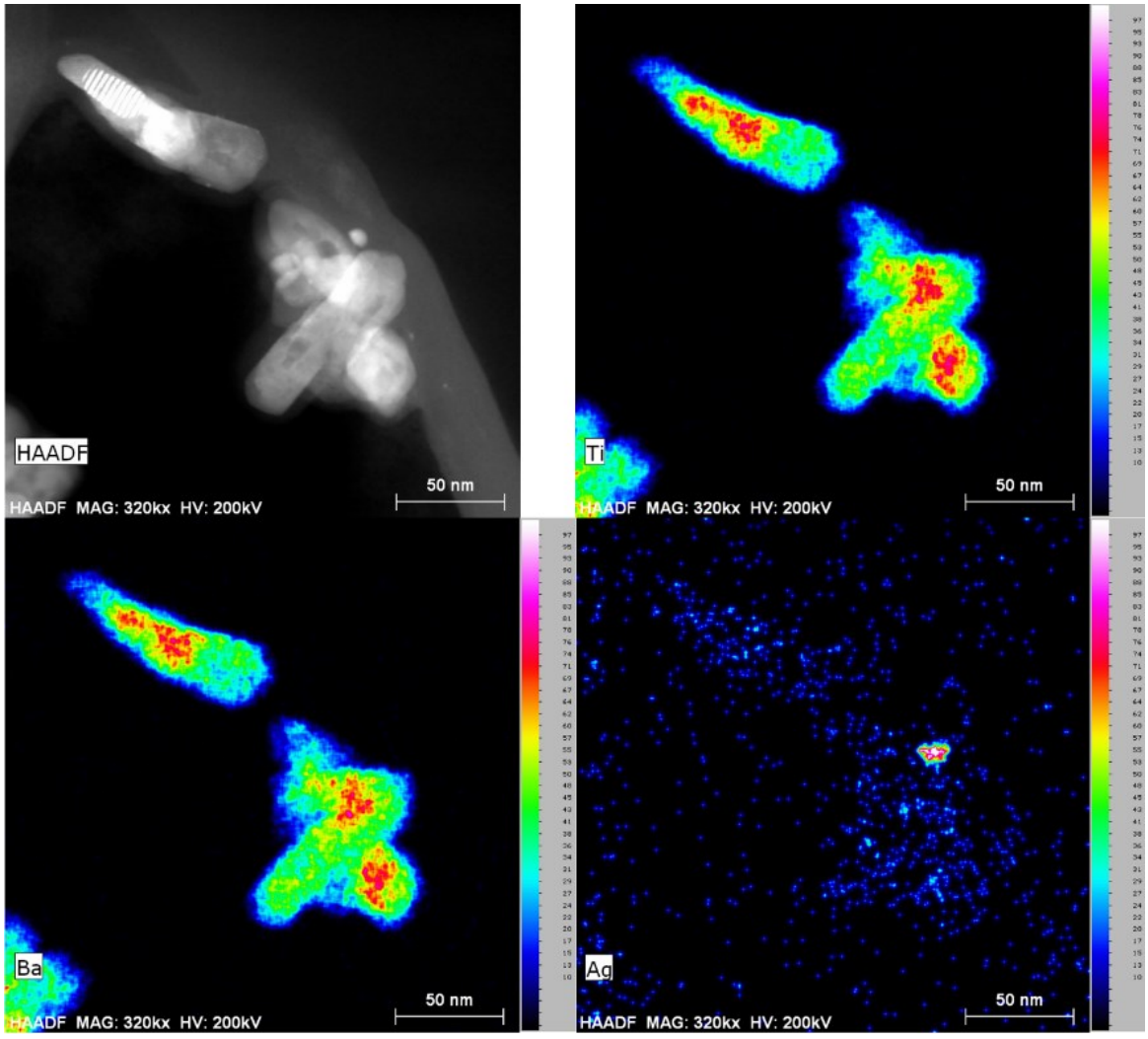

Figure 5.7. HAADF image and heat map obtained by EDS techniques of the $BaTiO_3$ particles that were irradiated for 6 h with neutrons, subsequently treated by ultrasonication for 2 min, and incubated in a solution of Ag^+ before purification for TEM-based analyses.

Figure 5.7. shows a HAADF image of $BaTiO_3$ particles in the top left section of the four quadrants of this figure, as well as the heat maps obtained by EDS techniques for the Ba, Ti, and Ag atoms distributed within these particles in the remaining images. These particles had been irradiated for 6 h with neutrons and were incubated in a solution of Ag ions. The EDS spectra for the three elements demonstrate that the presence of silver is minimal compared to the amount of Ba and Ti in the particles. The amount of silver present is similar to the levels observed in the non-irradiated particles. The presence of silver in vicinity of the $BaTiO_3$ particles is still higher than in the background, showing some deposition of silver onto the particles.

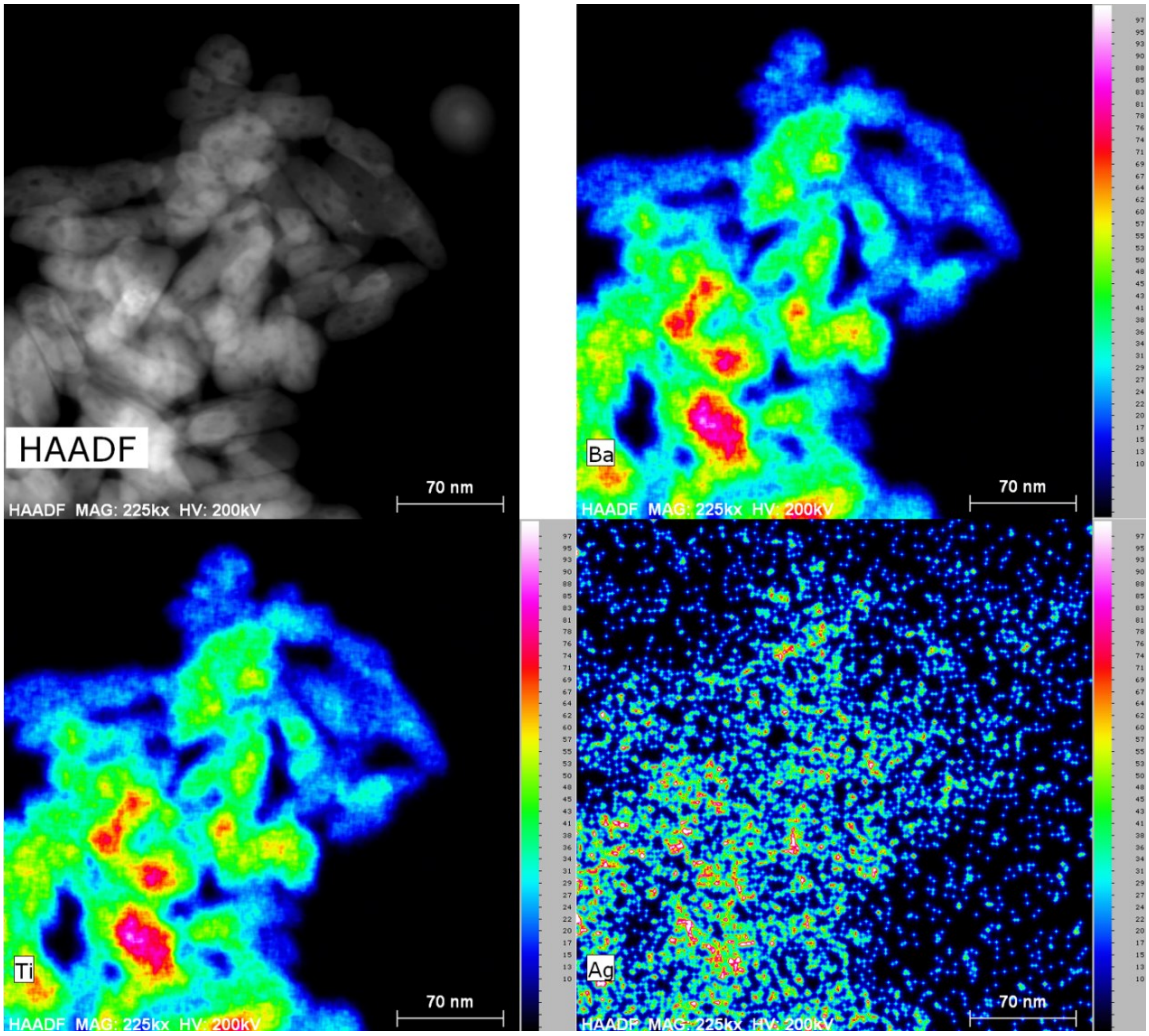

Figure 5.8. HAADF image and heat maps obtained by EDS technique of $BaTIO_3$ nanoparticles that had been irradiated with neutrons for 24 h and subsequently incubated in a solution of Ag^+ before being purified and imaged by TEM techniques.

Figure 5.8. shows a HAADF image of $BaTiO_3$ particles in the top left section of the four-quadrant figure, as well as the corresponding heat maps for the distribution of Ba, Ti and Ag atoms within the particles as obtained by EDS techniques. These particles were irradiated for 24 h and were incubated in a solution of Ag ions, and subsequently purified in preparation for these TEM-based analyses. The EDS-based maps for the three elements demonstrated that the presence of silver was noticeably higher compared to the samples irradiated for 6 h. The presence of silver in vicinity of the $BaTiO_3$ particles is higher than in the background, indicating a deposition of silver onto the particles. Furthermore, there is significantly higher silver deposition onto these particles in comparison to the particles irradiated for 6 h.

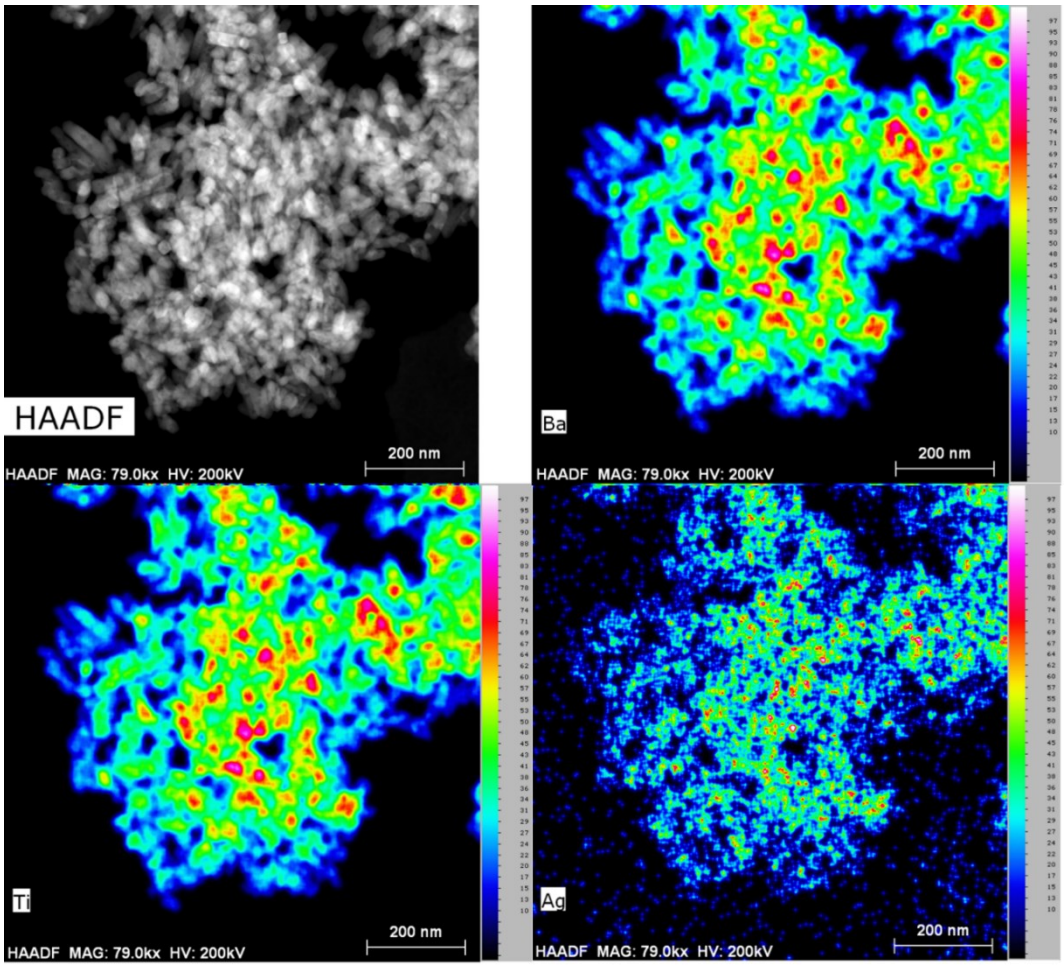

Figure 5.9. A representative HAADF image and heat maps obtained by EDS for $BaTiO_3$ particles that had been irradiated for 24 h, sonicated for 2 min, and subsequently incubated in a solution of Ag^+. These materials were purified before imaging by TEM and EDS mapping.

Figure 5.9. shows a HAADF image of $BaTiO_3$ particles in the top left section of the four-quadrant figure, as well as the heat maps depicting the distributions of Ba, Ti and Ag atoms within these irradiated particles. These particles were irradiated for 24 h, sonicated for 2 min and were incubated in a solution of Ag ions. The EDS spectra for the three elements the presence of silver is noticeably higher compared to the samples irradiated for 6 h. The silver in vicinity to the $BaTiO_3$ particles is higher than in the background, showing deposition of silver onto the irradiated particles. Not only is there significantly higher silver deposition onto the particles in comparison to the particles irradiated for 6 h, but it appears that sonication may have increased the oxygen displacement and potentially bond breakage, resulting in an increase in the silver deposition onto the surfaces of the particles when compared to the non-sonicated particles that were irradiated for 24 h.

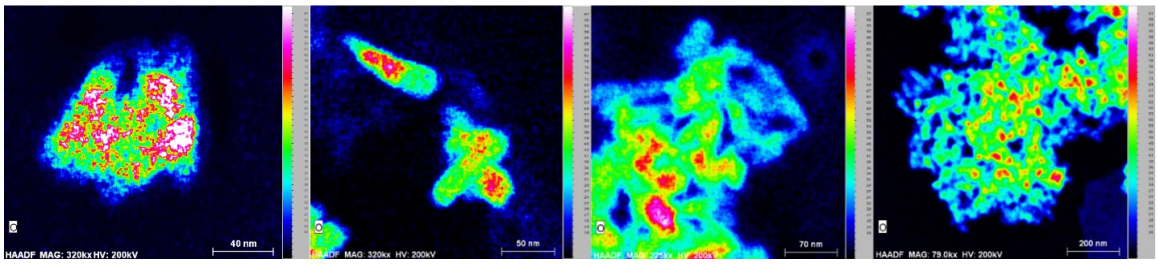

Figure 5.10. EDS based heat maps of the O within in non-irradiated $BaTiO_3$ particles prepared by ultrasonication (left). As well as particles irradiated for 6 h and sonicated (middle left), particles irradiated for 24 h without sonication (middle right), and particles irradiated for 24 h and sonicated 2 min (right).

Figure 5.10. contains heat maps obtained by EDS techniques of the oxygen content in the irradiated and non-irradiated $BaTiO_3$ samples. The spectra suggest that there is no notable change in the oxygen content before and after irradiation (see Table 5.1). This suggests that the increase of silver deposition on the irradiated $BaTiO_3$ is not due to a significant increase or decrease in the relative oxygen content as a result of exposure to neutron radiation. Furthermore, if silver deposition is due to oxidation of oxygen vacancies, then the increased silver deposition is due to either a very low concentration of vacancies and/or from displaced oxygen within the lattice wherein the processes of irradiation result in the formation of charged species and radicals. This result is supported by the prior art depicting the breakage of bonds from both exposure to radiation and from sonication, including the sensitivity of O-bonds specifically.[177,179]The series of images presented herein also suggest a relationship between the duration of the radiation exposure and the amount of silver deposited onto the particles.

Comparing the heat maps obtained by EDS techniques across the different irradiation conditions, there is a notable increase in the silver content for the particles irradiated for 24 h in comparison to those without any radiation exposure. Furthermore, there may be an increase in the silver content after 24 h of exposure to fast neutrons when these particles were sonicated versus those that were not treated by sonication. This result may be due to a further breakage in the bonds within the barium titanate lattice due to sonication. It has been known that sonication at a frequency of ~40 kHz can result in the breaking of C-C bonds, while at 22 kHz it is sufficient to cleave C–O or P–O bonds within the sugar-phosphate backbone of DNA[179] This might be the case for oxygen bonds within $BaTiO_3$ as well, but this could also result from displacement of the Ba and/or BaO species from the lattice given the bond strength of the Ti-O bonds and the sub-units of TiO_2 formed within the lattice as mentioned above.

Table 5.1. Relative abundances of Ba, Ti, O and Ag in irradiated and non-irradiated $BaTiO_3$

Sample	Ratio of Ti to O*	Ratio of Ba to O*	Ratio of Ag to Ti*
Non-irradiated $BaTiO_3$	0.23	0.18	0
6 hr irradiated $BaTiO_3$	0.25	0.20	0.007 ± 0.002
24 hr irradiated $BaTiO_3$ (not sonicated)	0.24	0.22	0.040 ± 0.007
24 hr irradiated $BaTiO_3$ (sonicated)	0.24	0.19	0.040 ± 0.009

* Obtained through EDS analysis by comparing atomic %

Given the data obtained to date, it is not possible to draw a quantitative conclusion with regards to the underlying mechanism as to why there was a significant increase in silver content observed for the irradiated particles. There was, for example, no notable change in the relative amount of oxygen, barium depicted in the EDS based heat maps, making it unlikely that the significant increase in silver deposition was due to a change in the O and/or Ba content relative to the Ti content.

5.7.3. Evaluation of Crystallinity of Irradiated $BaTiO_3$ Nanoparticle

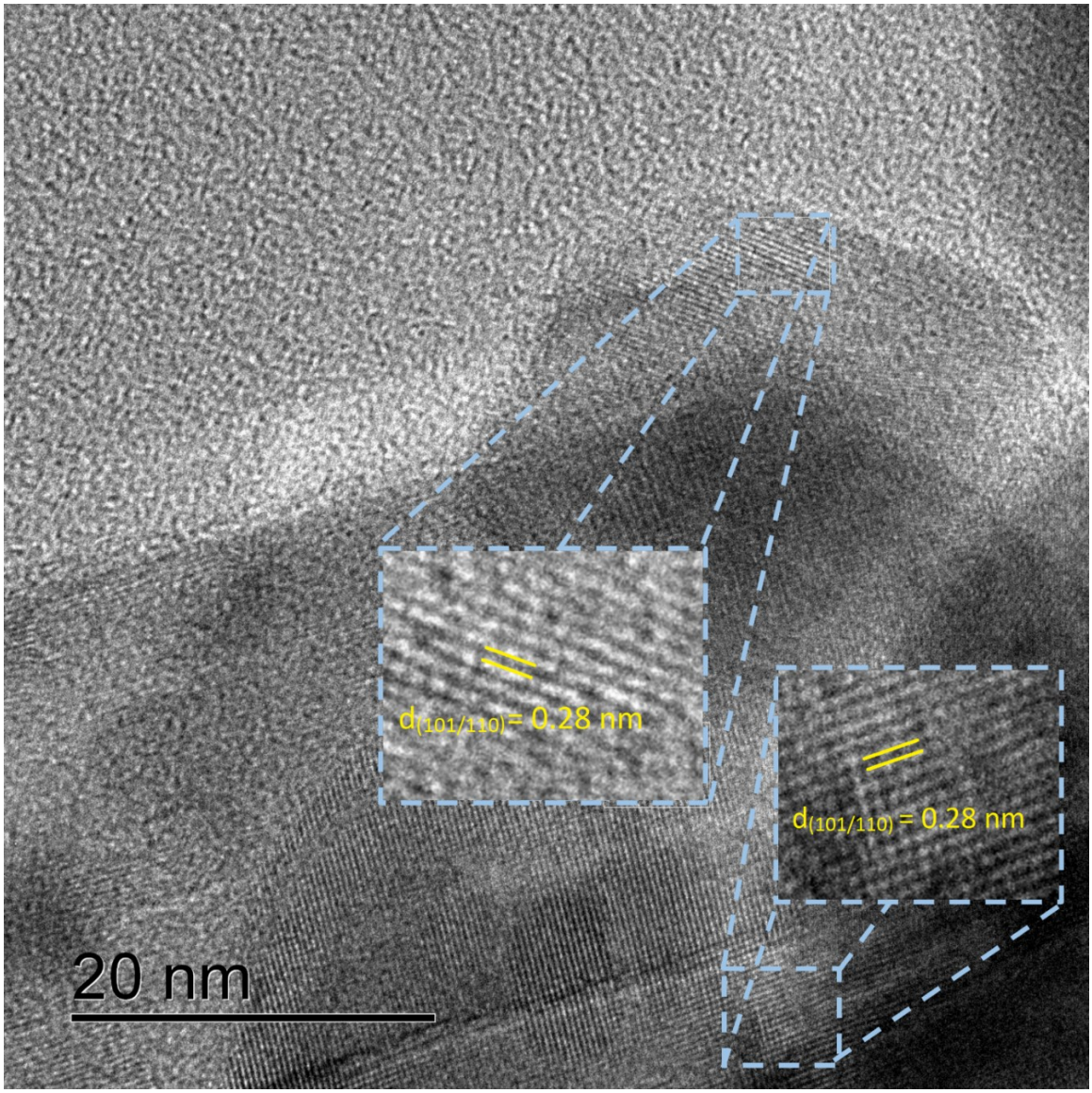

Figure 5.11. HRTEM image of agglomerated $BaTiO_3$ nanoparticles that were not irradiated. The two insets show an enlarged image of the outlined areas.

Figure 5.11. depicts a representative high-resolution TEM (HRTEM) image of agglomerated $BaTIO_3$ nanoparticles before being irradiated with fast neutrons. The two insets are enlarged images of the regions outlined in the light blue dashed boxes. The measured distance between the adjacent planes shown in the insets suggests a *d* spacing of 2.8 Å, corresponding to either the (110) or (111) crystal planes of $BaTiO_3$, or both.

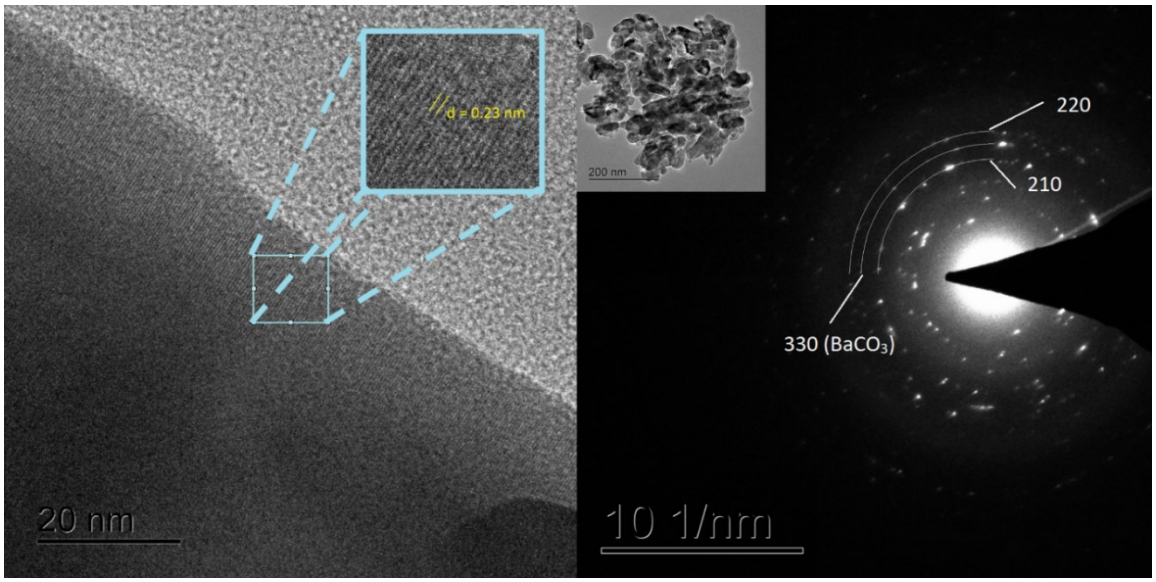

Figure 5.12. TEM and SAED image of $BaTiO_3$ particle after being irradiated for 24 h and sonicated for 2 min. The inset within the SAED pattern shows the selected area for the electron diffraction.

Figure 5.12. shows the lattice spacing for a portion of a $BaTiO_3$ particle after 24 h of neutron irradiation. In the leftmost image, the corresponding inset shows fringes demonstrating an interplanar spacing within the lattice of this material of 2.3 Å. This distance corresponds to the (111) plane of $BaTiO_3$. The right image depicts an SAED pattern showing diffraction patterns that correspond to the (220) and (210) planes of $BaTiO_3$. Diffraction rings also denote the (330) plane of a $BaCO_3$ impurity formed during $BaTiO_3$ synthesis.

The study used $BaTiO_3$ with relatively thin morphologies in the hopes to observe potentially distinguishable effects of the neutron irradiation at the edges of the $BaTiO_3$ particles, but the TEM-based analyses could not identify notable damage to the edges of the particles, such as fragmentation or cracking. The lack of visible, quantifiable damage to these particles suggests that the total fluence of ~4.0 x 10^{10} neutrons cm^{-2} was not sufficient to cause any discernable damage to the particles, even after sonication of the particles. It was, however, sufficient to create lattice defects that led to the reduction of silver on the surfaces of the $BaTiO_3$ nanoparticles.

5.8. Conclusions and Outlook

The tolerance of nanoscale $BaTiO_3$ to neutron radiation has been elucidated in terms of changes to the crystallinity and morphology of these particles. It appears that crystal planes belonging to certain planes of $BaTiO_3$ remain even after neutron radiation at a total fluence of 4.0×10^{10} neutrons cm^{-2}. Furthermore, no notable damage to the edges of the particles were observed by TEM techniques, which suggested there was no notable radiation-induced damage at the surfaces of the particles and likely even less damage resulted within the bulk of the particles.

However, while significant changes in lattice or morphologies were not detected from the results, there appears to be atomic displacements with the presence of broken and dangling bonds from any of the atomic constituents of $BaTiO_3$. This conclusion is drawn from the EDS spectra that show heat maps for the distributions of the different elements in these samples, wherein increased radiation times led to an increased amount of silver deposited onto the $BaTiO_3$ particles. However, there did not appear to be a quantifiable increase or decrease in oxygen content after irradiation. This suggests that the increased silver content from reduction of its salt may be due to increased oxygen displacements as a result of exposure to neutron radiation, as opposed to significant changes in the oxygen content specifically. Previous studies have demonstrated the breaking of oxygen bonds during some forms of irradiation. It should be noted that while a neutron fluence of 4×10^{10} neutrons cm^{-2} appears to result in a significant oxygen (or barium/titanium) displacement within the crystal lattices, a neutron fluence of 1×10^{10} neutrons cm^{-2} resulted in significantly lower atomic displacement; there was not a significant amount of silver deposition when compared to that of the non-irradiated $BaTiO_3$.

Single atom displacements are not easily seen with the electron microscopy systems available at SFU. But through the use of a simple chemical method for the site selective silver deposition onto the $BaTiO_3$ particles, the visualization of radiation-induced oxygen displacements appears to be a viable method for detecting the formation of such defects. With exposure to higher amounts of radiation, there was more deposition of silver, which was indicative of a higher extent of displaced oxygen within the $BaTiO_3$ lattice. These results support the practicality of using chemical methods as a simpler and more cost-effective way of determining the forms of radiation damage on the surfaces of nanomaterials

These results demonstrating a form of radiation tolerance up to a particular flux of fast neutrons give motivation for further work in investigating radiation-induced damage in nanoscale $BaTiO_3$, as well as further evaluation of chemical methods for detecting radiation damage. For example, comparing silver deposition onto irradiated nanoscale $BaTiO_3$ versus particles that have diameters that are several micrometers in size. The results of such a chemical amplification process could confirm an increased resilience of nanomaterials to atomic displacements through increasing grain boundaries via smaller particles size. These outcomes can also be applied to studying effects of radiation on particle crystallinity and morphology.

Chapter 6.

Executive Summary and Outlook

The work herein is the culmination of our efforts in producing and evaluating a series of nanomaterials for radiation studies. Developing nanomaterials is an important process for many industries. The inherent nature of nanomaterials means that their structure is greatly influential on their function. It is not surprising that nanomaterials can be beneficial in industries that involve the production and handling of radioactive materials. Nuclear energy, nuclear medicine, solar power, space exploration, are all involved in environments with high amounts of radiation exposure. The results in this study tell a compelling argument for the purpose of this thesis: to contribute to a relatively new and emerging field of nano-based technologies that can be used in extreme environments including the exposure to high energy particles.

Producing ^{32}P using a portable neutron generator can provide motivation for the on-site production of radionuclides for clinical and medical uses—especially if we can increase the efficiencies for processing these radionuclides. We have successfully isolated ^{32}P from nanosized sulfur following their irradiation with neutrons at an energy of ~14 MeV through the $^{32}S(n,p)^{32}P$ reaction. The ^{32}P was extracted from the sulfur through a simple process of heating of the nanosized sulfur in toluene, with an extraction efficiency of 49%. Furthermore, we demonstrated an easier extraction of ^{32}P from irradiated nanosized sulfur when compared to a commercial powder of sulfur with a larger particle size. As well, sulfur rods were synthesized using a method that was easier than what has been reported in the prior literature and within $1/4^{th}$ the amount of time of this prior art. These rods could be used in the future for ^{32}P extraction with these materials assembled into a porous mesh for the continuous extraction of ^{32}P from the irradiated sulfur nanorods by passing a solvent through this network. The work accomplished so for has established the foundations towards developing easier and more cost-effective radionuclide production and extraction.

Chapter 4 in this thesis provides a glimpse into the range of studies that demonstrate how nanomaterials and nanostructured features enhance radiation tolerance. The self-healing nature of these materials are powered by the multitude of nano features that drive annihilation of radiation-induced defects. The radiation tolerance of a

perovskite, $BaTiO_3$, was investigated for changes to morphology and crystallinity. The work in this thesis demonstrates the sustained presence of crystal planes in nanocrystalline $BaTiO_3$ to ~14 MeV neutrons with a fluence of 1 x 10^{10} neutrons cm^{-2}. Furthermore, we demonstrate the use of silver reduction and deposition onto surfaces of $BaTiO_3$ particles to evaluate the effects and extent of radiation induced damage to these particles. Given what is known about the breakage of bonds during radiation, it can be hypothesized that the increased silver deposition on the particles irradiated with neutrons for a longer duration is due to an increased oxygen displacement within the lattice. Likely the dangling bonds and charges, formed from lattice structure impact with high energy neutrons, facilitates the silver reduction onto the barium titanate particles. If this hypothesis is correct, then this chemical enhancement could provide a simpler and far more cost-effective alternative to the exclusive use of costly electron microscopy methods alone for detecting lattice damage and atomic displacements within these nanocrystalline materials.

The work in this thesis has set the foundations for developing future methods in radionuclide production, the development of materials that are more durable to the effects of neutron radiation, and a technique to assist in visualizing the extent and distribution of radiation-induced damage in nanomaterials. It is clear that a lot more work needs to be done to apply what has been developed in this thesis to real world applications. The promising results herein provide the foundation and further motivation to pursue these opportunities.

References

(1) Vetterick, G. A.; Gruber, J.; Suri, P. K.; Baldwin, J. K.; Kirk, M. A.; Baldo, P.; Wang, Y. Q.; Misra, A.; Tucker, G. J.; Taheri, M. L. Achieving Radiation Tolerance through Non-Equilibrium Grain Boundary Structures. *Scientific Reports* **2017**, *7* (1). https://doi.org/10.1038/s41598-017-12407-2.

(2) Kim, Y.; Baek, J.; Kim, S.; Kim, S.; Ryu, S.; Jeon, S.; Han, S. M. Radiation Resistant Vanadium-Graphene Nanolayered Composite. *Scientific Reports* **2016**, *6*, 24785. https://doi.org/10.1038/srep24785.

(3) Bryan, J. C. *Introduction to Nuclear Science*, 3rd ed.; 2018.

(4) OECD/NEA. *The Supply of Medical Isotopes: An Economic Diagnosis and Possible Solutions*; ORGANIZATION FOR ECONOMIC, 2019.

(5) Pouget, J. P.; Constanzo, J. Revisiting the Radiobiology of Targeted Alpha Therapy. *Frontiers in Medicine* **2021**, *8*. https://doi.org/10.3389/fmed.2021.692436.

(6) L'Annunziata, M. F. *Handbook of Radioactivity Analysis*, 2nd ed.; Academic Press, 2004.

(7) United States Environmental Protection Agency. *Radioactive Decay*.

(8) National Research Council, D. on E. and L. S. N. and R. S. B. and C. on M. I. P. W. H. E. U. *Medical Isotope Production Without Highly Enriched Uranium*; National Academies Press, 2009.

(9) Schlissel, D.; Biewald, B. *Nuclear Power Plant Construction Costs* ; Cambridge, 2008.

(10) World Nuclear Association. *Plans For New Reactors Worldwide*.

(11) Krikorian, S. *Preliminary Nuclear Power Facts and Figures for 2019*. IAEA.

(12) Khanal, L. R.; Sundararajan, J. A.; Qiang, Y. Advanced Nanomaterials for Nuclear Energy and Nanotechnology. *Energy Technology* **2020**, *8* (3), 1–23. https://doi.org/10.1002/ente.201901070.

(13) Nawada, H. P.; Ganguly, C.; International Atomic Energy Agency. *Management of Reprocessed Uranium : Current Status and Future Prospects.*; International Atomic Energy Agency, 2007.

(14) Elsaidi, S. K.; Mohamed, M. H.; Helal, A. S.; Galanek, M.; Pham, T.; Suepaul, S.; Space, B.; Hopkinson, D.; Thallapally, P. K.; Li, J. Radiation-Resistant Metal-Organic Framework Enables Efficient Separation of Krypton Fission Gas from Spent Nuclear Fuel. *Nature Communications* **2020**, *11* (1), 3103. https://doi.org/10.1038/s41467-020-16647-1.

(15) Rivai, A. K.; Dimyati, A.; Adi, W. A. Mechanosynthesis of A Ferritic ODS (Oxide Dispersion Strengthened) Steel Containing 14% Chromium and Its Characterization. *IOP Conference Series: Materials Science and Engineering* **2017**, *202* (1). https://doi.org/10.1088/1757-899X/202/1/012068.

(16) Hassan, T. A. A. Development of Nanosensors in Nuclear Technology. In *AIP Conference Proceedings*; American Institute of Physics Inc., 2017; Vol. 1799. https://doi.org/10.1063/1.4972925.

(17) Pushpavanam, K.; Inamdar, S.; Dutta, S.; Bista, T.; Sokolowski, T.; Boshoven, E.; Sapareto, S.; Rege, K. Determination of Topographical Radiation Dose Profiles Using Gel Nanosensors. *Sci. Adv* **2019**, *5*, 8704–8719.

(18) Espinet-Gonzalez, P.; Barrigón, E.; Otnes, G.; Vescovi, G.; Mann, C.; France, R. M.; Welch, A. J.; Hunt, M. S.; Walker, D.; Kelzenberg, M. D.; Åberg, I.; Borgström, M. T.; Samuelson, L.; Atwater, H. A. Radiation Tolerant Nanowire Array Solar Cells. *ACS Nano* **2019**, *13* (11), 12860–12869. https://doi.org/10.1021/acsnano.9b05213.

(19) IAEA. *Review of Fuel Failures in Water Cooled Reactors*; 2010.

(20) Nordlund, K.; Zinkle, S. J.; Sand, A. E.; Granberg, F.; Averback, R. S.; Stoller, R.; Suzudo, T.; Malerba, L.; Banhart, F.; Weber, W. J.; Willaime, F.; Dudarev, S. L.; Simeone, D. Improving Atomic Displacement and Replacement Calculations with Physically Realistic Damage Models. *Nature Communications* **2018**, *9* (1). https://doi.org/10.1038/s41467-018-03415-5.

(21) Buchan, J. T.; Robinson, M.; Christie, H. J.; Roach, D. L.; Ross, D. K.; Marks, N. A. Molecular Dynamics Simulation of Radiation Damage Cascades in Diamond. *Journal of Applied Physics* **2015**, *117* (24). https://doi.org/10.1063/1.4922457.

(22) Jiang, M.; Peng, S. M.; Zhang, H. B.; Xu, C. H.; Xiao, H. Y.; Zhao, F. A.; Liu, Z. J.; Zu, X. T. Ab Initio Molecular Dynamics Simulation of the Effects of Stacking Faults on the Radiation Response of 3C-SiC. *Scientific Reports* **2016**, *6*. https://doi.org/10.1038/srep20669.

(23) Yang, Y.; Zheng, G.; Cui, Y. Nanostructured Sulfur Cathodes. *Chemical Society Reviews* **2013**, *42* (7), 3018–3032. https://doi.org/10.1039/c2cs35256g.

(24) Ji, X.; Lee, K. T.; Nazar, L. F. A Highly Ordered Nanostructured Carbon-Sulphur Cathode for Lithium-Sulphur Batteries. *Nature Materials* **2009**, *8* (6), 500–506. https://doi.org/10.1038/nmat2460.

(25) Wang, L.; Chen, B.; Ma, J.; Cui, G.; Chen, L. Reviving Lithium Cobalt Oxide-Based Lithium Secondary Batteries-toward a Higher Energy Density. *Chemical Society Reviews* **2018**, *47* (17), 6505–6602. https://doi.org/10.1039/c8cs00322j.

(26) Franklin, J. L.; Jaffe, . ; F; Gaydon, ; G. *Dissociation Energies and Spectra of Diatomic Molecules*; John Wiley and Sons, Inc, 1949; Vol. 41.

(27) Guo, Y.; Zhao, J.; Yang, S.; Yu, K.; Wang, Z.; Zhang, H. Preparation and Characterization of Monoclinic Sulfur Nanoparticles by Water-in-Oil Microemulsions Technique. *Powder Technology* **2006**, *162* (2), 83–86. https://doi.org/10.1016/j.powtec.2005.12.012.

(28) Soleimani, M.; Aflatouni, F.; Khani, A. A New and Simple Method for Sulfur Nanoparticles Synthesis. *Colloid Journal* **2013**, *75* (1), 112–116. https://doi.org/10.1134/S1061933X12060142.

(29) Deshpande, A. S.; Khomane, R. B.; Vaidya, B. K.; Joshi, R. M.; Harle, A. S.; Kulkarni, B. D. Sulfur Nanoparticles Synthesis and Characterization from H 2S Gas, Using Novel Biodegradable Iron Chelates in W/O Microemulsion. *Nanoscale Research Letters* **2008**, *3* (6), 221–229. https://doi.org/10.1007/s11671-008-9140-6.

(30) Shankar, S.; Jaiswal, L.; Rhim, J. W. New Insight into Sulfur Nanoparticles: Synthesis and Applications. *Critical Reviews in Environmental Science and Technology* **2021**, *51* (20), 2329–2356. https://doi.org/10.1080/10643389.2020.1780880.

(31) Jana, N. R.; Gearheart, L.; Murphy, C. J. Wet Chemical Synthesis of High Aspect Ratio Cylindrical Gold Nanorods. *Journal of Physical Chemistry B* **2001**, *105* (19), 4065–4067. https://doi.org/10.1021/jp0107964.

(32) Jin, W.; Liang, G.; Zhong, Y.; Yuan, Y.; Jian, Z.; Wu, Z.; Zhang, W. The Influence of CTAB-Capped Seeds and Their Aging Time on the Morphologies of Silver Nanoparticles. *Nanoscale Research Letters* **2019**, *14*. https://doi.org/10.1186/s11671-019-2898-x.

(33) Hossain, F. Natural and Anthropogenic Radionuclides in Water and Wastewater: Sources, Treatments and Recoveries. *Journal of Environmental Radioactivity* **2020**, *225*. https://doi.org/10.1016/j.jenvrad.2020.106423.

(34) Porras, I.; Sabaté-Gilarte, M.; Praena, J.; Quesada, J. M.; Esquinas, P. L. 33S for Neutron Capture Therapy: Nuclear Data for Monte Carlo Calculations. *Nuclear Data Sheets* **2014**, *120*, 246–249. https://doi.org/10.1016/j.nds.2014.07.058.

(35) Viktor Zerkin, N. I. A. E. A. *Experimental Nuclear Reaction Data (EXFOR)* .

(36) National Center for Biotechnology Information. *Phosphorus Radioisotopes*. Pub Chem.

(37) Sgouros, G.; Bodei, L.; McDevitt, M. R.; Nedrow, J. R. Radiopharmaceutical Therapy in Cancer: Clinical Advances and Challenges. *Nature Reviews Drug Discovery*. Nature Research September 1, 2020, pp 589–608. https://doi.org/10.1038/s41573-020-0073-9.

(38) Pattillo, R. A.; Collier, B. D.; Abdel-Dayem, H.; Ozker, K.; Wilson, C.; Ruckert, A. C. F.; Hamilton, K. Phosphorus-32-Chromic Phosphate for Ovarian Cancer: I. Fractionated Low-Dose Intraperitoneal Treatments in Conjunction with Platinum Analog Chemotherapy. *Journal of Nuclear Medicine* **1995**, *36* (1), 29–36.

(39) Parmentier, C. Use and Risks of Phosphorus-32 in the Treatment of Polycythaemia Vera. *European Journal of Nuclear Medicine and Molecular Imaging* **2003**, *30* (10), 1413–1417. https://doi.org/10.1007/s00259-003-1270-6.

(40) Barriger, R. B.; Chang, A.; Lo, S. S.; Timmerman, R. D.; Desrosiers, C.; Boaz, J. C.; Fakiris, A. J. Phosphorus-32 Therapy for Cystic Craniopharyngiomas. *Radiotherapy and Oncology* **2011**, *98* (2), 207–212. https://doi.org/10.1016/j.radonc.2010.12.001.

(41) Cheng, Y.; Kiess, A. P.; Herman, J. M.; Pomper, M. G.; Meltzer, J.; Abraham, J. M. Phosphorus-32 , a Clinically Available Drug , Inhibits Cancer Growth by Inducing DNA Double-Strand Breakage. **2015**, 1–11. https://doi.org/10.1371/journal.pone.0128152.

(42) Voet, D.; Voet, J. G.; Pratt, C. W. Metabolism. In *Principles of Biochemistry International Student Version*; Voet, D., Voet, J. G., Pratt, C. W., Eds.; John Wiley & Sons, 2012; pp 436–767.

(43) Leijtens, T.; Bush, K. A.; Prasanna, R.; McGehee, M. D. Opportunities and Challenges for Tandem Solar Cells Using Metal Halide Perovskite Semiconductors. *Nature Energy* **2018**, *3* (10), 828–838. https://doi.org/10.1038/s41560-018-0190-4.

(44) Yin, W. J.; Shi, T.; Yan, Y. Unique Properties of Halide Perovskites as Possible Origins of the Superior Solar Cell Performance. *Advanced Materials* **2014**, *26* (27), 4653–4658. https://doi.org/10.1002/adma.201306281.

(45) Ringwood, A. E.; Kesson, S. E.; Ware, N. G.; Hibberson, W.; Major, A. Immobilisation of High Level Nuclear Reactor Wastes in SYNROC. *Nature* **1979**, *278*, 219–223.

(46) Acosta, M.; Novak, N.; Rojas, V.; Patel, S.; Vaish, R.; Koruza, J.; Rossetti, G. A.; Rödel, J. BaTiO3-Based Piezoelectrics: Fundamentals, Current Status, and Perspectives. *Applied Physics Reviews* **2017**, *4* (4). https://doi.org/10.1063/1.4990046.

(47) Zhao, C.; Wu, H.; Li, F.; Cai, Y.; Zhang, Y.; Song, D.; Wu, J.; Lyu, X.; Yin, J.; Xiao, D.; Zhu, J.; Pennycook, S. J. Practical High Piezoelectricity in Barium Titanate Ceramics Utilizing Multiphase Convergence with Broad Structural Flexibility. *J Am Chem Soc* **2018**, *140* (45), 15252–15260. https://doi.org/10.1021/jacs.8b07844.

(48) Merz, W. J. Merz 1949 Dielectric Behavior of BaTiO3. *Physical Review* **1949**, *75*, 687.

(49) Nakashima, K.; Onagi, K.; Kobayashi, Y.; Ishigaki, T.; Ishikawa, Y.; Yoneda, Y.; Yin, S.; Kakihana, M.; Sekino, T. Stabilization of Size-Controlled BaTiO3 Nanocubes via Precise Solvothermal Crystal Growth and Their Anomalous Surface Compositional Reconstruction. *ACS Omega* **2021**, *6* (14), 9410–9425. https://doi.org/10.1021/acsomega.0c05878.

(50) Gadiyar, C.; Loiudice, A.; D'Ambra, F.; Oveisi, E.; Stoian, D.; Iyengar, P.; Castilla-Amorós, L.; Mantella, V.; Buonsanti, R. Nanocrystals as Precursors in Solid-State Reactions for Size- A Nd Shape-Controlled Polyelemental Nanomaterials. *J Am Chem Soc* **2020**, *142* (37), 15931–15940. https://doi.org/10.1021/jacs.0c06556.

(51) Li, J.; Wu, Q.; Wu, J. Synthesis of Nanoparticles via Solvothermal and Hydrothermal Methods. In *Handbook of Nanoparticles*; Springer International Publishing, 2015; pp 1–28. https://doi.org/10.1007/978-3-319-13188-7_17-1.

(52) Nunes, D.; Pimental, A.; Santos, L.; Barquinha, P.; Pereira, L.; Fortunato, E.; Martins, R. Synthesis, Design, and Morphology of Metal Oxide Nanostructures. In *Metal Oxide Nanostructures: Synthesis, Properties and Applications*; Elsevier, 2019.

(53) Shameer Ahmed, B.; Namratha, K.; Nandaprakash, M. B.; Somashekar, R.; Byrappa, K. Effect of Gamma Irradiation on Hydrothermally Synthesized Barium Titanate Nanoparticles. *Radiation Effects and Defects in Solids* **2017**, *172* (3–4), 257–270. https://doi.org/10.1080/10420150.2017.1303835.

(54) Keating, J. J.; Murphy, Glenn. Gamma-Irradiation Effects in Single-Crystalline Barium Titanate. *Physcal Review* **1969**, *184* (2), 476–480.

(55) Sharma, S.; Tomar, M.; Puri, N. K.; Gupta, V. Ultraviolet Radiation Detection by Barium Titanate Thin Films Grown by Sol-Gel Hydrothermal Method. *Procedia Engineering* **2014**, *87*, 1172–1175. https://doi.org/10.1016/j.proeng.2014.11.375.

(56) Hilczer, B. Effect of Neutron Irradiation on the Ferroelectric Properties of Barium Titanate Ceramics. *Physica Status Solidi (B)* **1963**, *2* (4), 447–455.

(57) Stash, A. I.; Ivanov, S. A.; Stefanovich, S. Y.; Mosunov, A. v.; Boyko, V. M.; Ermakov, V. S.; Korulin, A. v.; Kalyukanov, A. I.; Isakova, N. N. X-Ray Diffraction Study of BaTiO3 Single Crystals before and after Fast-Neutron Irradiation. *Crystallography Reports* **2015**, *60* (5), 620–628. https://doi.org/10.1134/S1063774515050168.

(58) Ali, R. F.; Ovens, J. S.; Starosta, K.; Gates, B. D. Novel Defect-Fluorite Pyrochlore Sodium Niobate Nanoparticles: Solution-Phase Synthesis and Radiation Tolerance Analysis. *Nanoscale* **2019**, *11* (12), 5489–5498. https://doi.org/10.1039/c8nr10385b.

(59) Santry, D. C.; Butler, N. D. J. P. THE S32 (n,p) P32 REACTION AS A FAST-NEUTRON FLUX MONITOR. *Canadian Journal of Chemistry* **1963**, *41*, 123–133.

(60) Nguyen, T. T.; Ngo, H. H.; Guo, W. Pilot Scale Study on a New Membrane Bioreactor Hybrid System in Municipal Wastewater Treatment. *Bioresource Technology* **2013**, *141*, 8–12. https://doi.org/10.1016/j.biortech.2013.03.125.

(61) Jang, M.; Chen, W.; Cannon, F. S. Preloading Hydrous Ferric Oxide into Granular Activated Carbon for Arsenic Removal. *Environmental Science and Technology* **2008**, *42* (9), 3369–3374. https://doi.org/10.1021/es7025399.

(62) Blaney, L. M.; Cinar, S.; SenGupta, A. K. Hybrid Anion Exchanger for Trace Phosphate Removal from Water and Wastewater. *Water Research* **2007**, *41* (7), 1603–1613. https://doi.org/10.1016/j.watres.2007.01.008.

(63) Gao, Y.-M.; Senguptaj, A. K.; Simpson, D. A NEW HYBRID INORGANIC SORBENT FOR HEAVY METALS REMOVAL. *Water Research* **1995**, *29* (9), 2195–2205.

(64) Suzuki, T. M.; Bomani, J. O.; Matsunaga, H.; Yokoyama, T. Preparation of Porous Resin Loaded with Crystalline Hydrous Zirconium Oxide and Its Application to the Removal of Arsenic. *Reactive & Functional Polymers* **2000**, *43*, 165–172.

(65) Dutta, P. K.; Ray, A. K.; Sharma, V. K.; Millero, F. J. Adsorption of Arsenate and Arsenite on Titanium Dioxide Suspensions. *Journal of Colloid and Interface Science* **2004**, *278* (2), 270–275. https://doi.org/10.1016/j.jcis.2004.06.015.

(66) Foster, X.; Vaneeckhaute, C. Modifying the Resin Type of Hybrid Anion Exchange Nanotechnology (HAIX-Nano) to Improve Its Regeneration and Phosphate Recovery Efficiency. *npj Clean Water* **2021**, *4* (1). https://doi.org/10.1038/s41545-021-00142-1.

(67) Fultz, B.; Howe, J. M. *Transmission Electron Microscopy and Diffractometry of Materials*, 3rd ed.; Springer Berlin, Heidelberg, 2008.

(68) Beckman Coulter. *Beckman LS6500 Scintillation Counter Manual*; 1999.

(69) Aganbi, E.; Iwegbue, C. M. A.; Martincigh, B. S. Concentrations and Risks of Polychlorinated Biphenyls (PCBs) in Transformer Oils and the Environment of a Power Plant in the Niger Delta, Nigeria. *Toxicology Reports* **2019**, *6*, 933–939. https://doi.org/10.1016/j.toxrep.2019.08.008.

(70) National Diagnostics. *Principles and Applications of Liquid Scintillation Counting*; 2004.

(71) Haldrup, K.; Vankó, G.; Gawelda, W.; Galler, A.; Doumy, G.; March, A. M.; Kanter, E. P.; Bordage, A.; Dohn, A.; van Driel, T. B.; Kjær, K. S.; Lemke, H. T.; Canton, S. E.; Uhlig, J.; Sundström, V.; Young, L.; Southworth, S. H.; Nielsen, M. M.; Bressler, C. Guest-Host Interactions Investigated by Time-Resolved X-Ray Spectroscopies and Scattering at MHz Rates: Solvation Dynamics and Photoinduced Spin Transition in Aqueous Fe(Bipy)32+. *Journal of Physical Chemistry A* **2012**, *116* (40), 9878–9887. https://doi.org/10.1021/jp306917x.

(72) Davis, R. E. Displacement Reactions at the Sulfur Atom Displacement Reactions at the Sulfur Atom. I. An Interpretation of the Decomposition of Acidified Thiosulfate. *J Am Chem Soc* **1958**, *80* (14), 3565–3569.

(73) Lamer, V. K.; Dinegar, R. H. Theory, Production and Mechanism of Formation of Monodispersed Hydrosols. *J Am Chem Soc* **1950**, *72* (11).

(74) Lindsey, R. K.; Goldman, N.; Fried, L. E.; Bastea, S. Chemistry-Mediated Ostwald Ripening in Carbon-Rich C/O Systems at Extreme Conditions. *Nature Communications* **2022**, *13* (1). https://doi.org/10.1038/s41467-022-29024-x.

(75) Whitehead, C. B.; Özkar, S.; Finke, R. G. LaMer's 1950 Model of Particle Formation: A Review and Critical Analysis of Its Classical Nucleation and Fluctuation Theory Basis, of Competing Models and Mechanisms for Phase-Changes and Particle Formation, and Then of Its Application to Silver Halide, Semiconductor, Metal, and Metal-Oxide Nanoparticles. *Materials Advances* **2021**, *2* (1), 186–235. https://doi.org/10.1039/d0ma00439a.

(76) st. John, S.; Nan, Z.; Hu, N.; Schaefer, D. W.; Angelopoulos, A. P. A Nanoscale-Modified LaMer Model for Particle Synthesis from Inorganic Tin-Platinum Complexes. *Journal of Materials Chemistry A* **2013**, *1* (31), 8903–8916. https://doi.org/10.1039/c3ta11552f.

(77) Jia, H.; Bai, X.; Li, N.; Yu, L.; Zheng, L. Siloxane Surfactant Induced Self-Assembly of Gold Nanoparticles and Their Application to SERS. *CrystEngComm* **2011**, *13* (20), 6179–6184. https://doi.org/10.1039/c1ce05715d.

(78) Javadian, S.; Kakemam, J. Intermicellar Interaction in Surfactant Solutions; a Review Study. *Journal of Molecular Liquids* **2017**, *242*, 115–128. https://doi.org/10.1016/j.molliq.2017.06.117.

(79) Khan, M. Y.; Samanta, A.; Ojha, K.; Mandal, A. Interaction between Aqueous Solutions of Polymer and Surfactant and Its Effect on Physicochemical Properties. *Asia-Pacific Journal of Chemical Engineering* **2008**, *3* (5), 579–585. https://doi.org/10.1002/apj.212.

(80) Li, M.; Schnablegger, H.; Mann, S. Coupled Synthesis and Self-Assembly of Nanoparticles to Give Structures with Controlled Organization. *Nature* **1999**, *402*, 393–395.

(81) Mann, S.; Davis, S. A.; Hall, S. R.; Li, M.; Rhodes, K. H.; Shenton, W.; Vaucher, S.; Zhang, B. Crystal Tectonics: Chemical Construction and Self-Organization beyond the Unit Cellf. *Journal of the Chemical Society, Dalton Transactions* **2000**, No. 21, 3753–3763. https://doi.org/10.1039/b004066p.

(82) Xie, X. Y.; Li, L. Y.; Zheng, P. S.; Zheng, W. J.; Bai, Y.; Cheng, T. F.; Liu, J. Facile Synthesis, Spectral Properties and Formation Mechanism of Sulfur Nanorods in PEG-200. *Materials Research Bulletin* **2012**, *47* (11), 3665–3669. https://doi.org/10.1016/j.materresbull.2012.06.043.

(83) Yeon, J. S.; Yun, S.; Park, J. M.; Park, H. S. Surface-Modified Sulfur Nanorods Immobilized on Radially Assembled Open-Porous Graphene Microspheres for Lithium-Sulfur Batteries. *ACS Nano* **2019**, *13* (5), 5163–5171. https://doi.org/10.1021/acsnano.8b08822.

(84) Seh, Z. W.; Li, W.; Cha, J. J.; Zheng, G.; Yang, Y.; McDowell, M. T.; Hsu, P. C.; Cui, Y. Sulphur-TiO 2 Yolk-Shell Nanoarchitecture with Internal Void Space for Long-Cycle Lithium-Sulphur Batteries. *Nature Communications* **2013**, *4*. https://doi.org/10.1038/ncomms2327.

(85) Gates, B.; Mayers, B.; Cattle, B.; Xia, Y. Synthesis and Characterization of Uniform Nanowires of Trigonal Selenium**. *Advanced Functional Materials* **2002**, *12* (3), 219–227.

(86) Daniel, M.-C.; Astruc, D. Gold Nanoparticles: Assembly, Supramolecular Chemistry, Quantum-Size-Related Properties, and Applications toward Biology, Catalysis, and Nanotechnology. **2004**. https://doi.org/10.1021/cr030698.

(87) Daruich De Souza, C.; Ribeiro Nogueira, B.; Rostelato, M. E. C. M. Review of the Methodologies Used in the Synthesis Gold Nanoparticles by Chemical Reduction. *Journal of Alloys and Compounds* **2019**, *798*, 714–740. https://doi.org/10.1016/j.jallcom.2019.05.153.

(88) Hu, X.; Zhang, Y.; Ding, T.; Liu, J.; Zhao, H. Multifunctional Gold Nanoparticles: A Novel Nanomaterial for Various Medical Applications and Biological Activities. *Frontiers in Bioengineering and Biotechnology* **2020**, *8*. https://doi.org/10.3389/fbioe.2020.00990.

(89) International Atomic Energy Agency. *IAEA Increases Projections for Nuclear Power Use in 2050*.

(90) The Australian Nuclear Science and Technology Organisation. *Improving the radiation tolerance of microelectronics for space*.

(91) Aglietti, G. S. Current Challenges and Opportunities for Space Technologies. *Frontiers in Space Technologies* **2020**, *1*. https://doi.org/10.3389/frspt.2020.00001.

(92) Dey, S.; Drazin, J. W.; Wang, Y.; Valdez, J. A.; Holesinger, T. G.; Uberuaga, B. P.; Castro, R. H. R. Radiation Tolerance of Nanocrystalline Ceramics: Insights from Yttria Stabilized Zirconia. *Scientific Reports* **2015**, *5*. https://doi.org/10.1038/srep07746.

(93) Aradi, E.; Lewis-Fell, J.; Harrison, R. W.; Greaves, G.; Mir, A. H.; Donnelly, S. E.; Hinks, J. A. Enhanced Radiation Tolerance of Tungsten Nanoparticles to He Ion Irradiation. *Nanomaterials* **2018**, *8* (12). https://doi.org/10.3390/NANO8121052.

(94) Miyazawa, Y.; Ikegami, M.; Chen, H. W.; Ohshima, T.; Imaizumi, M.; Hirose, K.; Miyasaka, T. Tolerance of Perovskite Solar Cell to High-Energy Particle Irradiations in Space Environment. *iScience* **2018**, *2*, 148–155. https://doi.org/10.1016/j.isci.2018.03.020.

(95) Kanaya, S.; Kim, G. M.; Ikegami, M.; Miyasaka, T.; Suzuki, K.; Miyazawa, Y.; Toyota, H.; Osonoe, K.; Yamamoto, T.; Hirose, K. Proton Irradiation Tolerance of High-Efficiency Perovskite Absorbers for Space Applications. *Journal of Physical Chemistry Letters* **2019**, *10* (22), 6990–6995. https://doi.org/10.1021/acs.jpclett.9b02665.

(96) Gao, N.; Yao, Z. W.; Lu, G. H.; Deng, H. Q.; Gao, F. Mechanisms for <100> Interstitial Dislocation Loops to Diffuse in BCC Iron. *Nature Communications* **2021**, *12* (1). https://doi.org/10.1038/s41467-020-20574-6.

(97) Singh, B. N.; Foreman, A. J. E.; Trinkaus, H. Radiation Hardening Revisited: Role of Intracascade Clustering. *Journal of Nuclear Materials* **1997**, *249* (2–3), 103–115. https://doi.org/10.1016/S0022-3115(97)00231-6.

(98) Ghoniem, N. M.; Sharafat, S.; Williams, J. M.; Mansur, L. K. Theory of Helium Transport and Clustering in Materials under Irradiation. *Journal of Nuclear Materials* **1983**, *117*, 96–105.

(99) Uberuaga, B. P.; Hoagland, R. G.; Voter, A. F.; Valone, S. M. Direct Transformation of Vacancy Voids to Stacking Fault Tetrahedra. *Physical Review Letters* **2007**, *99* (13). https://doi.org/10.1103/PhysRevLett.99.135501.

(100) Martínez, E.; Uberuaga, B. P. Mobility and Coalescence of Stacking Fault Tetrahedra in Cu. *Scientific Reports* **2015**, *5*. https://doi.org/10.1038/srep09084.

(101) Bryant, F. J.; Cox, A. F. J. Experimental and Calculated Atomic Displacement Threshold Energies for Binary Semiconductors. *Proc. Roy. Soc. A* **1969**, *310*, 319–339.

(102) Gonzalez, E.; Abreu, Y.; Cruz, C. M.; Piñera, I.; Leyva, A. Molecular-Dynamics Simulation of Threshold Displacement Energies in BaTiO3. *Nuclear Instruments and Methods in Physics Research, Section B: Beam Interactions with Materials and Atoms* **2015**, *358*, 142–145. https://doi.org/10.1016/j.nimb.2015.06.015.

(103) Gilbert, M. R.; Marian, J.; Sublet, J. C. Energy Spectra of Primary Knock-on Atoms under Neutron Irradiation. *Journal of Nuclear Materials* **2015**, *467*, 121–134. https://doi.org/10.1016/j.jnucmat.2015.09.023.

(104) Zolnikov, K. P.; Korchuganov, A. v.; Kryzhevich, D. S.; Chernov, V. M.; Psakhie, S. G. Formation of Point Defect Clusters in Metals with Grain Boundaries under Irradiation. *Physical Mesomechanics* **2019**, *22* (5), 355–364. https://doi.org/10.1134/S1029959919050023.

(105) Protasov, V. I.; Chudinov, V. G. Evolution of Cascade Region during the Thermal Spike. *Radiation Effects* **1982**, *66* (1), 1–7.

(106) Miessler, G. L.; Fischer, P. J.; Tarr, D. A. *Inorganic Chemistry*, 5th ed.; Pearson, 2014.

(107) Edwards, D. J.; Simonen, E. P.; Garner, F. A.; Greenwood, L. R.; Oliver, B. M.; Bruemmer, S. M. Influence of Irradiation Temperature and Dose Gradients on the Microstructural Evolution in Neutron-Irradiated 316SS. *Journal of Nuclear Materials* **2003**, *317* (1), 32–45. https://doi.org/10.1016/S0022-3115(03)00003-5.

(108) Zinkle, S. J.; Matsukawa, Y. Observation and Analysis of Defect Cluster Production and Interactions with Dislocations. *Journal of Nuclear Materials* **2004**, *329–333* (1-3 PART A), 88–96. https://doi.org/10.1016/j.jnucmat.2004.04.298.

(109) Jiang, S.; Wang, Z. Effect of Annealing on Microstructures and Hardening of Helium-Hydrogen-Implanted Sequentially Vanadium Alloys. *Nanoscale Research Letters* **2018**, *13*. https://doi.org/10.1186/s11671-018-2485-6.

(110) Zinkle, S. J.; Matsukawa, Y. Observation and Analysis of Defect Cluster Production and Interactions with Dislocations. *Journal of Nuclear Materials* **2004**, *329–333* (1-3 PART A), 88–96. https://doi.org/10.1016/j.jnucmat.2004.04.298.

(111) Singh, B. N.; Foreman, A. J. E.; Trinkaus, H. Radiation Hardening Revisited: Role of Intracascade Clustering. *Journal of Nuclear Materials* **1997**, *249* (2–3), 103–115. https://doi.org/10.1016/S0022-3115(97)00231-6.

(112) Kim, I. S.; Hunn, J. D.; Hashimoto, N.; Larson, D. L.; Maziasz, P. J.; Miyahara, K.; Lee, E. H. Defect and Void Evolution in Oxide Dispersion Strengthened Ferritic Steels under 3.2 MeV Fe+ Ion Irradiation with Simultaneous Helium Injection. *Journal of Nuclear Materials* **2000**, *280* (3), 264–274. https://doi.org/10.1016/S0022-3115(00)00066-0.

(113) Lu, C.; Lu, Z.; Wang, X.; Xie, R.; Li, Z.; Higgins, M.; Liu, C.; Gao, F.; Wang, L. Enhanced Radiation-Tolerant Oxide Dispersion Strengthened Steel and Its Microstructure Evolution under Helium-Implantation and Heavy-Ion Irradiation. *Scientific Reports* **2017**, *7* (January), 40343. https://doi.org/10.1038/srep40343.

(114) Zhang, F.; Boatner, L.; Zhang, Y.; Chen, D.; Wang, Y.; Wang, L. Swelling and Helium Bubble Morphology in a Cryogenically Treated FeCrNi Alloy with Martensitic Transformation and Reversion after Helium Implantation. *Materials* **2019**, *12* (17), 2821. https://doi.org/10.3390/ma12172821.

(115) Samaras, M.; Derlet, P. M.; van Swygenhoven, H.; Victoria, M. Radiation Damage near Grain Boundaries. *Philosophical Magazine* **2003**, *83* (31–34), 3599–3607. https://doi.org/10.1080/14786430310001600222.

(116) Swaminathan, N.; Kamenski, P. J.; Morgan, D.; Szlufarska, I. Effects of Grain Size and Grain Boundaries on Defect Production in Nanocrystalline 3C-SiC. *Acta Materialia* **2010**, *58* (8), 2843–2853. https://doi.org/10.1016/j.actamat.2010.01.009.

(117) Chen, Z.; Niu, L. L.; Wang, Z.; Tian, L.; Kecskes, L.; Zhu, K.; Wei, Q. A Comparative Study on the in Situ Helium Irradiation Behavior of Tungsten: Coarse Grain vs. Nanocrystalline Grain. *Acta Materialia* **2018**, *147*, 100–112. https://doi.org/10.1016/j.actamat.2018.01.015.

(118) Han, W. Z.; Demkowicz, M. J.; Fu, E. G.; Wang, Y. Q.; Misra, A. Effect of Grain Boundary Character on Sink Efficiency. *Acta Materialia* **2012**, *60* (18), 6341–6351. https://doi.org/10.1016/j.actamat.2012.08.009.

(119) Han, W. Z.; Demkowicz, M. J.; Fu, E. G.; Wang, Y. Q.; Misra, A. Effect of Grain Boundary Character on Sink Efficiency. *Acta Materialia* **2012**, *60* (18), 6341–6351. https://doi.org/10.1016/j.actamat.2012.08.009.

(120) Zhang, J.; He, H.; Liu, W.; Kang, L.; Yun, D.; Chen, P. Effects of Grain Boundaries on the Radiation-Induced Defects Evolution in BCC Fe–Cr Alloy: A Molecular Dynamics Study. *Nuclear Materials and Energy* **2020**, *22* (January), 0–6. https://doi.org/10.1016/j.nme.2020.100726.

(121) Arjhangmehr, A.; Feghhi, S. A. H. Irradiation Deformation near Different Atomic Grain Boundaries in α-Zr: An Investigation of Thermodynamics and Kinetics of Point Defects. *Scientific Reports* **2016**, *6* (March), 23333. https://doi.org/10.1038/srep23333.

(122) Arjhangmehr, A.; Feghhi, S. A. H.; Esfandiyarpour, A.; Hatami, F. An Energetic and Kinetic Investigation of the Role of Different Atomic Grain Boundaries in Healing Radiation Damage in Nickel. *Journal of Materials Science* **2016**, *51* (2), 1017–1031. https://doi.org/10.1007/s10853-015-9432-z.

(123) Bai, X. M.; Vernon, L. J.; Hoagland, R. G.; Voter, A. F.; Nastasi, M.; Uberuaga, B. P. Role of Atomic Structure on Grain Boundary-Defect Interactions in Cu. *Physical Review B - Condensed Matter and Materials Physics* **2012**, *85* (21), 1–10. https://doi.org/10.1103/PhysRevB.85.214103.

(124) Han, S. M.; Phillips, M. A.; Nix, W. D. Study of Strain Softening Behavior of Al-Al3Sc Multilayers Using Microcompression Testing. *Acta Materialia* **2009**, *57* (15), 4473–4490. https://doi.org/10.1016/j.actamat.2009.06.007.

(125) Wang, J.; Hoagland, R. G.; Hirth, J. P.; Misra, A. Atomistic Modeling of the Interaction of Glide Dislocations with "Weak" Interfaces. *Acta Materialia* **2008**, *56* (19), 5685–5693. https://doi.org/10.1016/j.actamat.2008.07.041.

(126) Phillips, M. A.; Clemens, B. M.; Nix, W. D. A Model for Dislocation Behavior during Deformation of Al/Al3Sc (Fcc/L12) Metallic Multilayers. *Acta Materialia* **2003**, *51* (11), 3157–3170. https://doi.org/10.1016/S1359-6454(03)00127-7.

(127) Fu, E. G.; Carter, J.; Swadener, G.; Misra, A.; Shao, L.; Wang, H.; Zhang, X. Size Dependent Enhancement of Helium Ion Irradiation Tolerance in Sputtered Cu/V Nanolaminates. *Journal of Nuclear Materials* **2009**, *385* (3), 629–632. https://doi.org/10.1016/j.jnucmat.2008.12.308.

(128) Fu, E. G.; Misra, A.; Wang, H.; Shao, L.; Zhang, X. Interface Enabled Defects Reduction in Helium Ion Irradiated Cu/V Nanolayers. *Journal of Nuclear Materials* **2010**, *407* (3), 178–188. https://doi.org/10.1016/j.jnucmat.2010.10.011.

(129) Victoria, M.; Baluc, N.; Bailat, C.; Dai, Y.; Luppo, M. I.; Schaublin, R.; Singh, B. N. Microstructure and Associated Tensile Properties of Irradiated Fcc and Bcc Metals. *Journal of Nuclear Materials* **2000**, *276* (1), 114–122. https://doi.org/10.1016/S0022-3115(99)00203-2.

(130) Diaz De La Rubla, T.; Zblb, H. M.; Khralshl, T. A.; Wirth, B. D.; Victoria, M.; Caturia, M. J. Multiscale Modelling of Plastic Flow Localization in Irradiated Materials. *Nature* **2000**, *406* (6798), 871–874. https://doi.org/10.1038/35022544.

(131) Ames, M.; Markmann, J.; Karos, R.; Michels, A.; Tschöpe, A.; Birringer, R. Unraveling the Nature of Room Temperature Grain Growth in Nanocrystalline Materials. *Acta Materialia* **2008**, *56* (16), 4255–4266. https://doi.org/10.1016/j.actamat.2008.04.051.

(132) Chookajorn, T.; Murdoch, H. A.; Schuh, C. A. Design of Stable Nanocrystalline Alloys. *Science (American Association for the Advancement of Science)* **2012**, *337* (6097), 951–954.

(133) Kurtz, R. J.; Odette, G. R.; Yamamoto, T.; Gelles, D. S.; Miao, P.; Oliver, B. M. The Transport and Fate of Helium in Martensitic Steels at Fusion Relevant He/Dpa Ratios and Dpa Rates. *Journal of Nuclear Materials* **2007**, *367-370 A* (SPEC. ISS.), 417–422. https://doi.org/10.1016/j.jnucmat.2007.03.121.

(134) Kim, I.; Jiao, L.; Khatkhatay, F.; Martin, M. S.; Lee, J.; Shao, L.; Zhang, X.; Swadener, J. G.; Wang, Y. Q.; Gan, J.; Cole, J. I.; Wang, H. Size-Dependent Radiation Tolerance in Ion Irradiated TiN/AlN Nanolayer Films. *Journal of Nuclear Materials* **2013**, *441* (1–3), 47–53. https://doi.org/10.1016/j.jnucmat.2013.05.035.

(135) Wei, Q. M.; Li, N.; Mara, N.; Nastasi, M.; Misra, A. Suppression of Irradiation Hardening in Nanoscale V/Ag Multilayers. *Acta Materialia* **2011**, *59* (16), 6331–6340. https://doi.org/10.1016/j.actamat.2011.06.043.

(136) Li, N.; Fu, E. G.; Wang, H.; Carter, J. J.; Shao, L.; Maloy, S. A.; Misra, A.; Zhang, X. He Ion Irradiation Damage in Fe/W Nanolayer Films. *Journal of Nuclear Materials* **2009**, *389* (2), 233–238. https://doi.org/10.1016/j.jnucmat.2009.02.007.

(137) Kutty, T. R. G.; Ravi, K.; Ganguly, C. Studies on Hot Hardness of Zr and Its Alloys for Nuclear Reactors. *Journal of Nuclear Materials* **1999**, *265* (1–2), 91–99. https://doi.org/10.1016/S0022-3115(98)00610-2.

(138) Park, J. Y.; Choi, B. K.; Jeong, Y. H.; Jung, Y. H. Corrosion Behavior of Zr Alloys with a High Nb Content. *Journal of Nuclear Materials* **2005**, *340* (2–3), 237–246. https://doi.org/10.1016/j.jnucmat.2004.12.003.

(139) Han, W.; Demkowicz, M. J.; Mara, N. A.; Fu, E.; Sinha, S.; Rollett, A. D.; Wang, Y.; Carpenter, J. S.; Beyerlein, I. J.; Misra, A. Design of Radiation Tolerant Materials via Interface Engineering. *Advanced Materials* **2013**, *25* (48), 6975–6979. https://doi.org/10.1002/adma.201303400.

(140) Li, N.; Nastasi, M.; Misra, A. Defect Structures and Hardening Mechanisms in High Dose Helium Ion Implanted Cu and Cu/Nb Multilayer Thin Films. *International Journal of Plasticity* **2012**, *32–33*, 1–16. https://doi.org/10.1016/j.ijplas.2011.12.007.

(141) Orowan, E. *Symposium on Internal Stresses in Metals and Alloys*; London, 1948.

(142) Misra, A.; Demkowicz, M. J.; Zhang, X.; Hoagland, R. G. The Radiation Damage Tolerance of Ultra-High Strength Nanolayered Composites. *Jom* **2007**, *59*, 62–65.

(143) Fayeulle, S.; Nastasi, M.; Lu, Y. C.; Kung, H.; Tesmer, J. R. Thermal and Ion Irradiation Stability of Direct Current Sputtered TiN/B-C-N Multilayers. *Applied Physics Letters* **1997**, *70* (9), 1098–1100. https://doi.org/10.1063/1.118496.

(144) Yang, K.; Huang, K.; Li, X.; Zheng, S.; Hou, P.; Wang, J.; Guo, H.; Song, H.; Li, B.; Li, H.; Liu, B.; Zhong, X.; Yang, J. Radiation Tolerance of Perovskite Solar Cells under Gamma Ray. *Organic Electronics* **2019**, *71*, 79–84. https://doi.org/10.1016/j.orgel.2019.05.008.

(145) Durant, B. K.; Afshari, H.; Singh, S.; Rout, B.; Eperon, G. E.; Sellers, I. R. Tolerance of Perovskite Solar Cells to Targeted Proton Irradiation and Electronic Ionization Induced Healing. *ACS Energy Letters* **2021**, *6* (7), 2362–2368. https://doi.org/10.1021/acsenergylett.1c00756.

(146) Paternò, G. M.; Robbiano, V.; Santarelli, L.; Zampetti, A.; Cazzaniga, C.; Garcìa Sakai, V.; Cacialli, F. Perovskite Solar Cell Resilience to Fast Neutrons. *Sustainable Energy and Fuels* **2019**, *3* (10), 2561–2566. https://doi.org/10.1039/c9se00102f.

(147) Zou, Y.; Wu, Y.; Guo, X.; Tong, S.; Wang, Z.; Zhang, L. Effect of Particle Size on the Densification and Dielectric Properties of $BaTiO_3$ Ceramics Prepared by Liquid Phase Sintering. *Physica Status Solidi (A) Applications and Materials Science* **2012**, *209* (2), 243–247. https://doi.org/10.1002/pssa.201127439.

(148) Boulos, M.; Guillemet-Fritsch, S.; Mathieu, F.; Durand, B.; Lebey, T.; Bley, V. Hydrothermal Synthesis of Nanosized $BaTiO_3$ Powders and Dielectric Properties of Corresponding Ceramics. *Solid State Ionics* **2005**, *176* (13–14), 1301–1309. https://doi.org/10.1016/j.ssi.2005.02.024.

(149) Haertling, G. H. Ferroelectric Ceramics: History and Technology. *Journal of the American Ceramic Society* **1999**, *82* (4), 797–818.

(150) Jung, W. S.; Park, J.; Park, Y.; Yoon, D. H. Effects of Impurities on the Properties of BaTiO3 Synthesized from Barium Titanyl Oxalate. *Ceramics International* **2010**, *36* (6), 1997–2002. https://doi.org/10.1016/j.ceramint.2010.03.033.

(151) Su, J.; Zhang, J. Recent Development on Modification of Synthesized Barium Titanate (BaTiO3) and Polymer/$BaTiO_3$ Dielectric Composites. *Journal of Materials Science: Materials in Electronics* **2019**, *30* (3), 1957–1975. https://doi.org/10.1007/s10854-018-0494-y.

(152) Testino, A.; Buscaglia, M. T.; Buscaglia, V.; Viviani, M.; Bottino, C.; Nanni, P. Kinetics and Mechanism of Aqueous Chemical Synthesis of $BaTiO_3$ Particles. *Chemistry of Materials* **2004**, *16* (8), 1536–1543. https://doi.org/10.1021/cm031130k.

(153) Gu, Y.; Sun, S.; Liu, Y.; Dong, M.; Yang, Q. Solvent Effect on the Solvothermal Synthesis of Mesoporous NiO Catalysts for Activation of Peroxymonosulfate to Degrade Organic Dyes. *ACS Omega* **2019**, *4* (18), 17672–17683. https://doi.org/10.1021/acsomega.9b01883.

(154) Zare, M.; Namratha, K.; Byrappa, K.; Surendra, D. M.; Yallappa, S.; Hungund, B. Surfactant Assisted Solvothermal Synthesis of ZnO Nanoparticles and Study of Their Antimicrobial and Antioxidant Properties. *Journal of Materials Science and Technology* **2018**, *34* (6), 1035–1043. https://doi.org/10.1016/j.jmst.2017.09.014.

(155) Sun, X.; Wang, J.; Xing, Y.; Zhao, Y.; Liu, X.; Liu, B.; Hou, S. Surfactant-Assisted Hydrothermal Synthesis and Electrochemical Properties of Nanoplate-Assembled 3D Flower-like $Cu_3V_2O_7(OH)_2 \cdot 2H_2O$ Microstructures. *CrystEngComm* **2011**, *13* (1), 367–370. https://doi.org/10.1039/c0ce00083c.

(156) Li, Y.; Liao, Z.; Fang, F.; Wang, X.; Li, L.; Zhu, J. Significant Increase of Curie Temperature in Nano-Scale $BaTiO_3$. *Applied Physics Letters* **2014**, *105* (18). https://doi.org/10.1063/1.4901169.

(157) Hongo, K.; Kurata, S.; Jomphoak, A.; Inada, M.; Hayashi, K.; Maezono, R. Stabilization Mechanism of the Tetragonal Structure in a Hydrothermally Synthesized $BaTiO_3$ Nanocrystal. *Inorganic Chemistry* **2018**, *57* (9), 5413–5419. https://doi.org/10.1021/acs.inorgchem.8b00381.

(158) Hongo, K.; Kurata, S.; Jomphoak, A.; Inada, M.; Hayashi, K.; Maezono, R. Stabilization Mechanism of the Tetragonal Structure in a Hydrothermally Synthesized $BaTiO_3$ Nanocrystal. *Inorganic Chemistry* **2018**, *57* (9), 5413–5419. https://doi.org/10.1021/acs.inorgchem.8b00381.

(159) Dutta, P. K.; Gregg, J. R. Hydrothermal Synthesis of Tetragonal Barium Titanate. *Chemistry of Materials* **1992**, *4*, 843–846.

(160) Dewan, M.; Kumar, A.; Saxena, A.; de, A.; Mozumdar, S. Using Hydrophilic Ionic Liquid, [Bmim]BF 4 - Ethylene Glycol System as a Novel Media for the Rapid Synthesis of Copper Nanoparticles. *PLoS ONE* **2012**, *7* (1). https://doi.org/10.1371/journal.pone.0029131.

(161) Yang, M.; Zhao, W.; Singh, S.; Simmons, B.; Cheng, G. On the Solution Structure of Kraft Lignin in Ethylene Glycol and Its Implication for Nanoparticle Preparation. *Nanoscale Advances* **2019**, *1* (1), 299–304. https://doi.org/10.1039/c8na00042e.

(162) López, C.; Rodríguez-Páez, J. E. Synthesis and Characterization of ZnO Nanoparticles: Effect of Solvent and Antifungal Capacity of NPs Obtained in Ethylene Glycol. *Applied Physics A: Materials Science and Processing* **2017**, *123* (12). https://doi.org/10.1007/s00339-017-1339-x.

(163) Li, J.; Zhu, J.; Liu, X. Ultrafine Silver Nanoparticles Obtained from Ethylene Glycol at Room Temperature: Catalyzed by Tungstate Ions. *Dalton Transactions* **2014**, *43* (1), 132–137. https://doi.org/10.1039/c3dt52242c.

(164) Silvert, P.-Y.; Herrera-Urbina, R.; Duvauchelle, N.; Vijayakrishnan, V.; Elhsissen, K. T. Preparation of Colloidal Silver Dispersions by the Polyol Process Part 1-Synthesis and Characterization. *Journal of Materials Chemistry* **1996**, *6* (4), 573–577.

(165) Carotenuto, G.; Pepe, G. P.; Nicolais, L. Preparation and Characterization of Nano-Sized Ag/PVP Composites for Optical Applications. *The European Physical Journal B* **2000**, *16*, 11–17.

(166) Wang, W.; Zhao, B.; Li, P.; Tan, X. Fabrication and Characterization of Pd/Ag Alloy Hollow Spheres by the Solvothermal Method. *Journal of Nanoparticle Research* **2008**, *10* (3), 543–548. https://doi.org/10.1007/s11051-007-9279-6.

(167) Veldhuis, S. A.; Vijselaar, W. J. C.; Stawski, T. M.; ten Elshof, J. E. Formation of Nanocrystalline Barium Titanate in Benzyl Alcohol at Room Temperature. *Inorganic Chemistry* **2014**, *53* (24), 13188–13196. https://doi.org/10.1021/ic502410v.

(168) Niederberger, M.; Garnweitner, G.; Pinna, N.; Antonietti, M. Nonaqueous and Halide-Free Route to Crystalline BaTiO3, SrTiO3, and (Ba,Sr)TiO3 Nanoparticles via a Mechanism Involving C-C Bond Formation. *J Am Chem Soc* **2004**, *126* (29), 9120–9126. https://doi.org/10.1021/ja0494959.

(169) Sprinzak, Y. Reduction and Benzylation by Means of Benzyl Alcohol. I. Carbon Benzylation. The Preparation of 9-Benzylfluorenes. *J Am Chem Soc* **1956**, *78* (2), 466–469.

(170) Hu, M.; Xu, J.; Gao, J.; Yang, S.; Wong, J. S. P.; Li, R. K. Y. Benzyl Alcohol-Based Synthesis of Oxide Nanoparticles: The Perspective of SN1 Reaction Mechanism. *Journal of the Chemical Society. Dalton Transactions* **2013**, *42* (26), 9777–9784. https://doi.org/10.1039/c3dt50680k.

(171) Kumari, R.; Kulriya, P. K.; Mishra, S.; Kotari, V.; Achary, S. N.; Tyagi, A. K.; Avasthi, D. K. Phase-Dependent Radiation-Resistant Behavior of BaTiO3: An in Situ X-Ray Diffraction Study. *Journal of the American Ceramic Society* **2017**, *100* (9), 4263–4269. https://doi.org/10.1111/jace.14941.

(172) Zhang, Y.; Rupich, M. W.; Solovyov, V.; Li, Q.; Goyal, A. Dynamic Behavior of Reversible Oxygen Migration in Irradiated-Annealed High Temperature Superconducting Wires. *Scientific Reports* **2020**, *10* (1). https://doi.org/10.1038/s41598-020-70663-1.

(173) di Francesca, D.; Boukenter, A.; Agnello, S.; Alessi, A.; Girard, S.; Cannas, M.; Ouerdane, Y. Resonance Raman of Oxygen Dangling Bonds in Amorphous Silicon Dioxide. *Journal of Raman Spectroscopy* **2017**, *48* (2), 230–234. https://doi.org/10.1002/jrs.5006.

(174) Ray, D. K.; Hutchinson, F.; Morowitz, H. J. A Connexion between S—S Bond Breakage and Inactivation by Radiation of a Dry Enzyme. *Nature* **1960**, *186*, 312–313.

(175) Gao, H.; Cao, J.; Liu, L.; Yang, Y. Theoretical Investigation on the Structure and Electronic Properties of Barium Titanate. *Journal of Molecular Structure* **2011**, *1003* (1–3), 75–81. https://doi.org/10.1016/j.molstruc.2011.07.024.

(176) Moriwake, H. First-Principles Calculation of Formation Energy of Neutral Point Defects in Perovskite-Type BaTiO3. *International Journal of Quantum Chemistry* **2004**, *99* (5 SPEC. ISS.), 824–827. https://doi.org/10.1002/qua.10863.

(177) Lushchik, A.; Kuzovkov, V. N.; Kotomin, E. A.; Prieditis, G.; Seeman, V.; Shablonin, E.; Vasil'chenko, E.; Popov, A. I. Evidence for the Formation of Two Types of Oxygen Interstitials in Neutron-Irradiated α-Al2O3 Single Crystals. *Scientific Reports* **2021**, *11* (1). https://doi.org/10.1038/s41598-021-00336-0.

(178) Sakurai, M.; Thirstrup, C.; Aono, M. Nanoscale Growth of Silver on Prepatterned Hydrogen-Terminated Si(001) Surfaces. *Physical Review B* **2000**, *62*, 16167–16174.

(179) Grokhovsky, S. L.; Il'icheva, I. A.; Nechipurenko, D. Y.; Golovkin, M. v.; Panchenko, L. A.; Polozov, R. v.; Nechipurenko, Y. D. Sequence-Specific Ultrasonic Cleavage of DNA. *Biophysical Journal* **2011**, *100* (1), 117–125. https://doi.org/10.1016/j.bpj.2010.10.052.

Appendix.

Supplemental Information

Figure A1. **General setup of irradiation experiments in front of the neutron generator for both $BaTiO_3$ and S samples.**

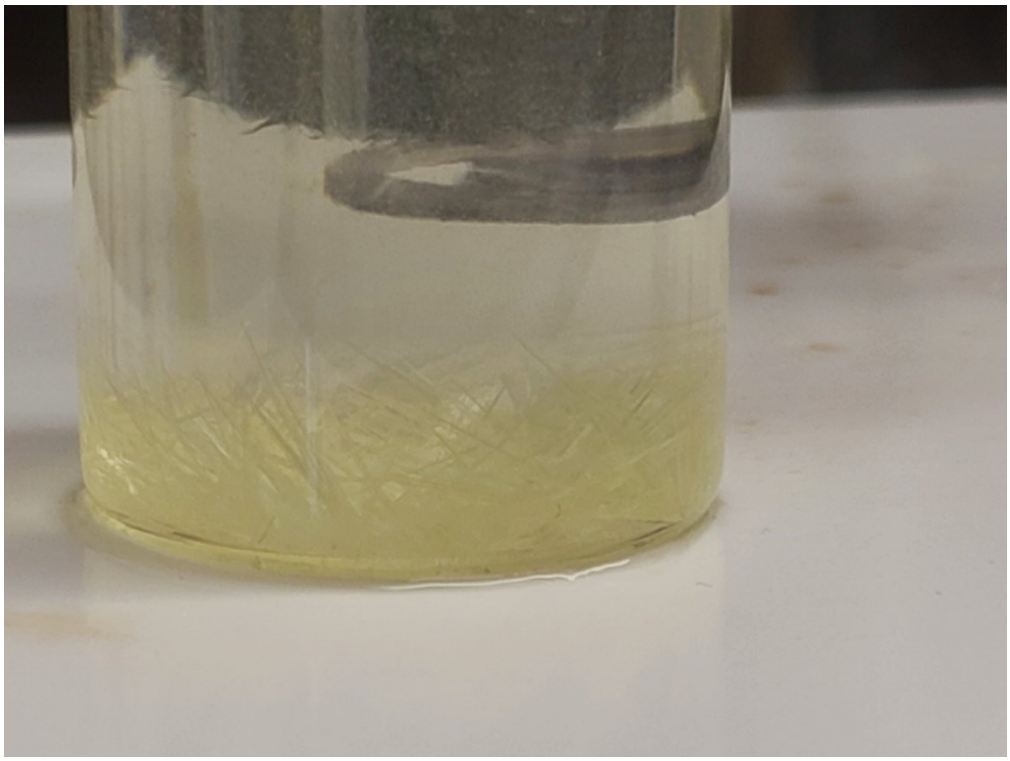

Figure A2. Sulfur crystals formed upon cooling of the solution of sulfur in hot toluene, immediately prior to ^{32}P extraction.

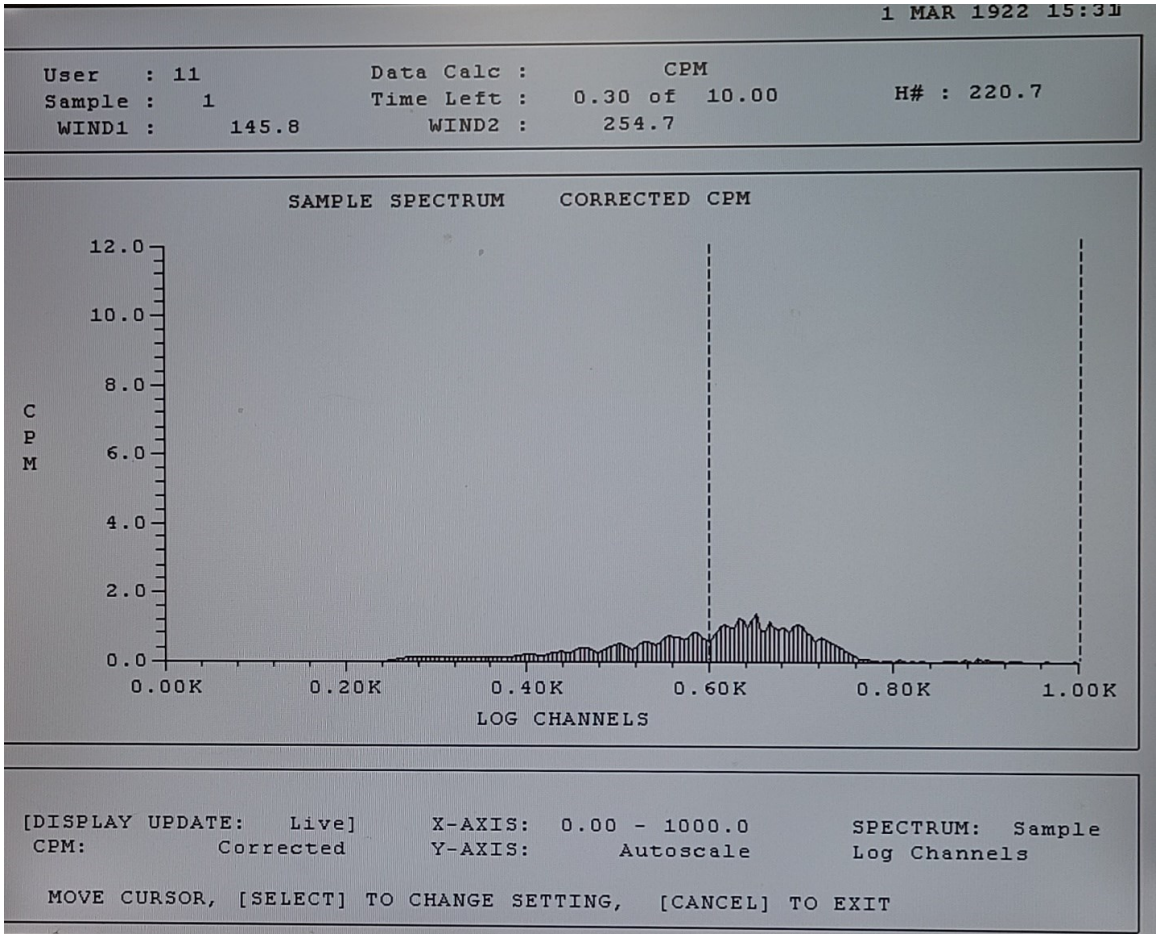

Figure A3. Picture of a sample spectra of ^{32}P emission energies on the Beckman LS6500 Liquid Scintillation Counter. The instrument does not allow printing or storing of such spectra. Energies past the dashed line (Window 2 shown above) are attributed to ^{32}P decay.

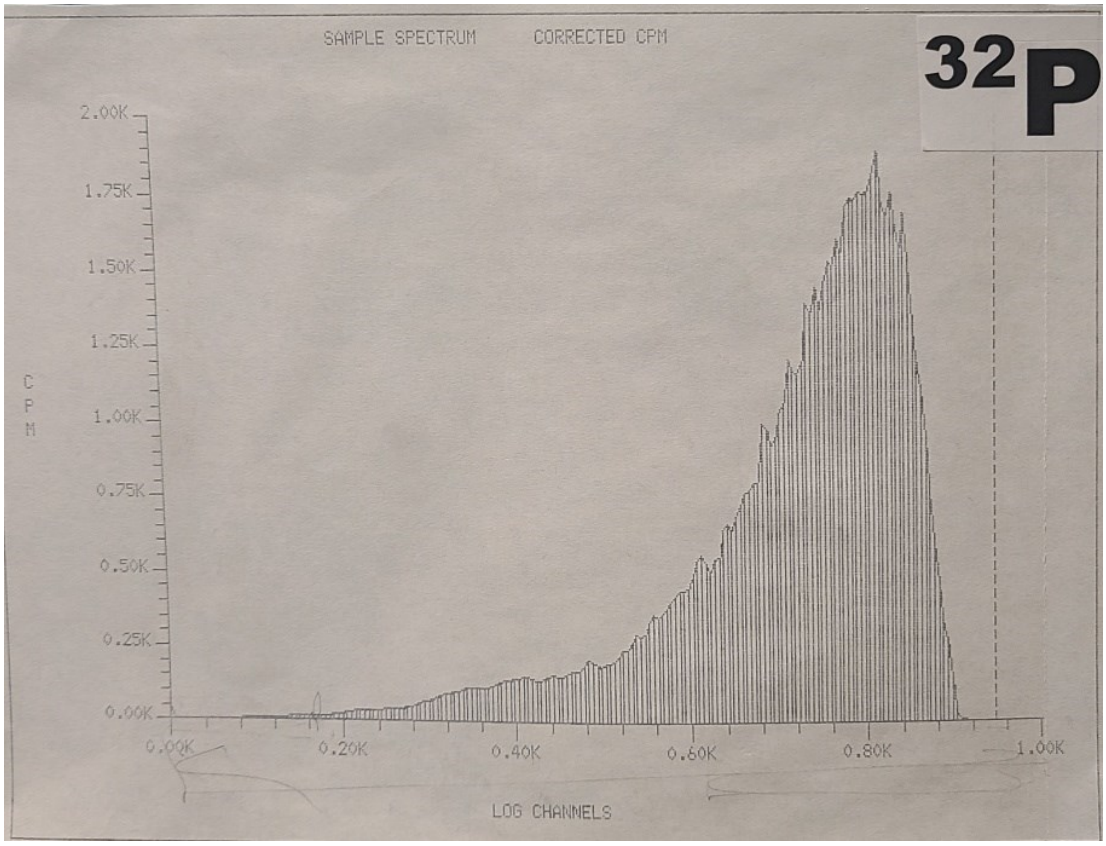

Figure A4. Reference energy spectrum of a ^{32}P standard using the Beckman LS6500 Liquid Scintillation Counter.

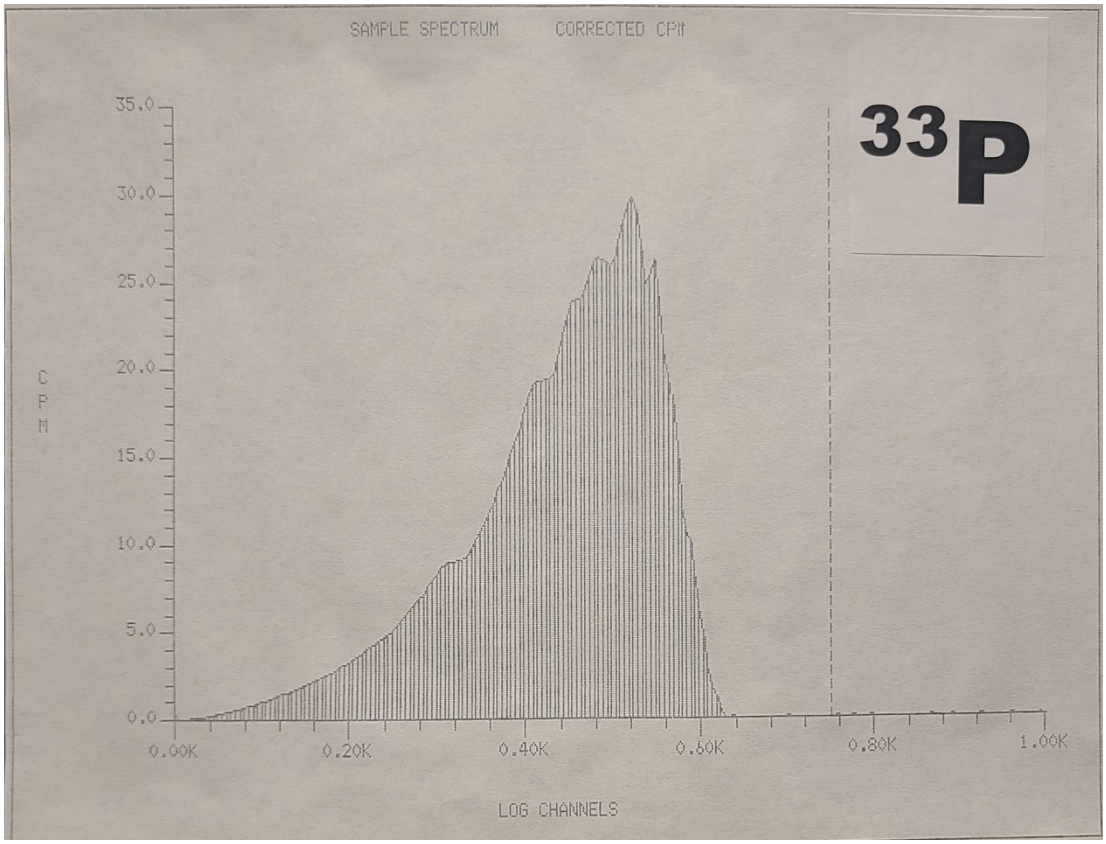

Figure A5. **Reference energy spectrum of a ^{33}P standard using the Beckman LS6500 Liquid Scintillation Counter. Based on a comparison of these standard samples, most of the energies associated with ^{33}P decay are below the log 0.60K channels for the instrument, whereas for ^{32}P most of the energies are above the log 0.60K. As such, measurements where only counted for energies above log 0.60K for the experiments in this study.**